X-ray tomography of a fluidized bed

Effect of pressure and fines on bubbles in a fluidized bed

MSC THESIS

DELFT UNIVERSITY OF TECHNOLOGY
FACULTY OF APPLIED SCIENCES
DEPARTMENT OF MULTI-SCALE PHYSICS

Author:
G.C. BROUWER
Applied Physics (R&D)
Studentnumber: 1174029
Start: February 2011
End: December 2011

Supervisors:
Prof.dr. R.F. MUDDE
Dr.ir. J.R. van OMMEN

Reviewer:
Dr.ir. J.J.J. GILLISSEN

December 16, 2011

Abstract

Using a fast X-ray tomography setup measurements have been done on a 25 cm diameter fluidized bed of Geldart B powder and a 24 cm bed of Geldart A powder. The average bubble sizes have been determined over a measurement period of 60 seconds. The resolution of this setup is about 4.5 mm per pixel at a rate of 250 reconstructions per second. It is possible to detect bubbles as small as 2.5 cm.

The Geldart B powder consisted of polystyrene particles with an average diameter of 607 μm and a bulk density of 625 kg/m^3. This bed was studied at pressures ranging from 1 to 5 bar$_{abs}$. This was done at superficial gas velocities from 12 to 32 cm/s for the atmospheric pressure measurements. For the highest pressure (5 bar$_{abs}$) this was 10 to 15 cm/s. These measurements showed that the normal gas flow can be increased from 500 l/min at atmospheric pressure to 1700 l/min at 5 bar$_{abs}$ before bubbles start appearing. The bubble size is significantly reduced at higher pressures for similar gas flows.

The Geldart A powder came in the form of several mixtures. These mixtures consist of a base of aluminum oxide particles with an average diameter of 76 μm and a bulk density of 680 kg/m^3. A different amount of fines was added to these base particles for the different mixtures. The fines consist of aluminum oxide particles with an average diameter of 38 μm and a bulk density of 620 kg/m^3. The fines contents varied from 0 to 50%$_{weight}$. An increase in fines content showed a clear reduction in average bubble size. If the fines content is increased from 0 to 50%$_w$ the average spherical equivalent bubble diameter is reduced by 20%.

NEDERLANDSE VERSIE

Met behulp van een hogesnelheids Röntgen tomografie opstelling zijn metingen gedaan aan een gefluidizeerd bed met een diameter van 25 cm met Geldart B deeltjes en een bed met een diameter van 24 cm met Geldart A deeltjes. De gemiddelde bel grootte over een periode van 60 seconde is bepaald. The resolutie van deze opstelling is ongeveer 4,5 mm per pixel met een snelheid van 250 reconstructies per seconde. Het is mogelijk bellen zo klein als 2,5 cm waar te nemen.

De Geldart B deeltjes bestaan uit polystyreen korrels met een gemiddelde diameter van 607 μm en een bulk dichtheid van 625 kg/m^3. Dit bed is bestudeerd onder drukken variërend van 1 tot 5 bar$_{abs}$. De superficiële gassnelheden varieerden van 12 tot 32 cm/s voor de atmosferische metingen. Voor de hoogste druk (5 bar$_{abs}$) was dit 10 tot 15 cm/s. De metingen lieten zien dan het mogelijk is om het gas debiet te verhogen van 500 normaal l/min bij atmosferische druk tot 1700 normaal l/min bij 5 bar$_{abs}$ voordat er bellen ontstaan. De bel grootte is aanzienlijk verminderd bij hogere druk en gelijke gas debieten.

De Geldart A deeltjes bestaan uit verschillende mengsels. Deze mengsels bestaan uit een basis van aluminium oxide deeltjes met een gemiddelde grootte van 76 μm en een bulk dichtheid van 680 kg/m^3. Een verschillende hoeveelheid 'fines' is aan deze basis deeltjes toegevoegd voor de verschillende mengsels. De 'fine' deeltjes bestaan uit aluminium oxide deeltjes met een gemiddelde diameter van 38 μm en een bulk dichtheid van 620 kg/m^3. Het 'fines' gehalte varieerde van 0 tot 50%$_{gewicht}$. Een toename van het 'fines' gehalte leidt tot een duidelijke vermindering in gemiddelde bel grootte. Als het fines gehalte van 0 tot 50%$_g$ wordt verhoogd, leidt dit tot een 20% kleinere gemiddelde sferische equivalente bubbel diameter.

Contents

Nomenclature

Roman symbols

symbol	description	unit
A_{cal}	calibration coefficient	
A_t	cross-section area of bed	m^2
B	incoming radiation	Sv
B_{cal}	calibration coefficient	
c	speed of light	m/s
C_{cal}	calibration coefficient	
d_{50}	median particle diameter	m
d_{em}	maximum spherical equivalent diameter	m
d_e	spherical equivalent diameter	m
d_p	particle diameter based on screen analysis	m
d_t	bed diameter	m
E	energy	eV
E_{photon}	photon energy	eV
g	acceleration of gravity	$9.8\ m/s^2$
g_c	conversion factor	$\frac{9.8kg \cdot m}{kg-wt \cdot s^2}$
h	Planck's constant	$6.62 \cdot 10^{-34} m^2 kg/s$
h_{bed}	height in the bed	m
l_{21}	interaction coefficient for bubbles	
L_f	height of bubbling fluidized bed	m
L_m	height of fixed bed	m
L_{mf}	height of bed at minimum fluidization	m
M	number of detectors (rays)	
m_{21}	interaction coefficient for bubbles	
p	pressure	Pa
$P_{45\mu m}$	weight fraction of bed that consists of fines	
p_b	pressure drop across bed	Pa
p_{fr}	frictional pressure drop	Pa
p_i	ray i sum	
R_1	radius of leading bubble	m
R_2	radius of trailing bubble	m
T	normalized transmission	
u	gas velocity	m/s
U_1	leading bubble rise velocity	m/s
U_2	trailing bubble rise velocity	m/s
$U_{b\infty}$	isolated bubble rise velocity	m/s
u_{br}	bubble rise velocity on top of gas velocity	m/s
$u_f = \frac{u_{mf}}{\epsilon_{mf}}$	upward velocity of gas at minimum fluidization	m/s
u_{mb}	minimum bubbling velocity	m/s
u_{mf}	minimum fluidization velocity	m/s
V_b	volume of bubble	m^3
W	weighting coefficient matrix	
W_{bed}	weight of solids in bed	kg
w_{ik}	weighting coefficient	
x_d	vertical distance between bubble centers	m
y_d	horizontal distance between bubble centers	m
Z	atomic number	

Greek symbols

symbol	description	unit
α	fitting parameter	
ϵ_m	voidage for bed as a whole	
ϵ_{mf}	voidage at minimum fluidization	
λ	wavelength	m
μ	viscosity of gas	kg/ms
μ_k	attenuation coefficient of pixel k	
$\mu_{material}$	linear attenuation coefficient	m^{-1}
ν	fitting parameter	
ϕ	gas flow rate	m^3/s
$\phi_{mb,n}$	normal gas flow rate at minimum bubbling conditions	m^3/s
ϕ_s	the sphericity of the particles	
Φ	photon fluence	$\mathrm{m}^{-2}\mathrm{s}^{-1}$
Φ_0	initial photon fluence	$\mathrm{m}^{-2}\mathrm{s}^{-1}$
ρ_g	gas density	kg/m^3
ρ_s	solids density	kg/m^3
ω	detector energy response function	

CHAPTER 1

Introduction

This master's thesis contains the results of the research done as part of the MSc program of Applied Physics at the Delft University of Technology. It is the result of work done in the department of Multi-Scale Physics, at the Kramers Lab under the supervision of prof.dr. R.F. Mudde (MSP/MultiPhase Flows) and dr.ir. J.R. van Ommen (ChemE/Product and Process Engineering).

The subject of this research is the behavior of a fluidized bed under increasing pressure and under increasing fines content. The size of the bubbles in the bed will be studied at various conditions, and we will look for trends and explain what is seen.

1.1 Motivation and background

Vessels filled with a solid particulate substance through which a gas is led can form a fluidized bed. If conditions are right the mixture can start behaving like a fluid. If the gas velocity is increased the bed can start bubbling in a way that resembles the boiling of a liquid. In that state there is a very good mixing of the gas and particles, so there will be no local hot spots and the gas and particles will have a very large contact surface area to react. This makes a fluidized bed very interesting to use in reactions where a catalyst is used. Fluidized beds can also be used in other ways, such as fluidized bed combustion or applying a coating onto solid items.

To optimize these processes it is important to better understand what is happening inside a fluidized bed. In the past several decades a lot of research has been done to predict how a bed behaves if it is scaled up from lab to industry scale and to get a better fundamental understanding of the fluidized bed itself. One of the biggest problems is that fluidized beds are generally not transparent to visible light. So it is not possible to study them using LDA (Laser Doppler anemometry) or other optical techniques. It is possible to measure pressure differences in a bed, but this only gives limited information. Another option would be to mount (optical) probes inside the bed. This will give more detailed information locally, but it will also disturb the flow inside the bed.

An example of a non-intrusive method used for studying fluidized beds is Electrical Capacitance Tomography (ECT). Using this technique it is possible to reconstruct a cross-section of the bed, which will show where the bubbles and particles are. This can be done at high speeds of more then 100 frames per second, see Warsito and Fan (2001). However, it is not possible to obtain the required spatial resolution. This is due to the 'soft-field' nature of ECT. Especially in setups with a larger diameter (more than 10 centimeters), ECT does not produce the results that are needed.

MRI is also an interesting technique to use for these kind of studies. Not only can it measure the solids distribution, but it can also find the velocity. The need for a very strong magnetic field makes it difficult to work with and very expensive.

Another possibility to trace the movement of a particle is to make this tracer particles radiative and follow it using CARPT (e.g. Chaouki et al. (1997)) or PEPT (e.g. Fangary et al. (2000), Dechsiri et al. (2005) and Fan et al. (2008)). The use of radioactive particles obviously makes several things more difficult. One of them is obtaining a license to perform these measurements.

X-ray tomography is a so-called 'hard-field' technique, which will be able to give the results that are needed for this research. The drawback is that X-rays are dangerous and the equipment required is expensive. Also, because of the Poisson distribution of the X-ray detection, the speed at which measurements can be done is limited. However, it is possible to achieve speeds of up to 250 frames/s, which is sufficient for this type of research.

Because X-ray tomography is widely used in the medical field, a lot of research has already been done to optimize this method of measuring. In hospitals CT-scans are done every day. These scans are done on patients that lie still, so it can be considered to be a static image. The bubbles in a fluidized bed typically travel at 0.1 to 1.5 m/s, which can hardly be considered static. Although a modern medical CT scanner can record several frames per second, this is not enough. Therefore a different setup was developed for the fluidized bed.

The X-ray setup developed at the Kramers Lab has previously proven that it works well and is capable of reconstructing bubbles in a fluidized bed (Alles (2006),Verhaart (2007)).

1.2 Research goals

As fluidized beds are often used in processes where a large contact surface area is wanted, bubbles are an undesirable phenomenon. Inside these bubbles there is a lot of gas that is not in contact with any particles. Higher gas throughputs, which cause bubbles, on the other hand, are desired. Finding ways to suppress the forming of bubbles, for these reasons, is an important research subject.

Previous research (e.g. Weimer and Quarderer (1985)) has indicated that raising the ambient pressure will reduce that bubble size. Also the addition of so-called fines, with an average particle diameter (d_{50}) of less than 45 μm, will decrease the size of the bubbles as seen by for example Beetstra et al. (2009).

To study these effects two measurement series have been performed. During the first series the vessel was filled with polystyrene spheres with a d_{50} of 607 μm. The pressure inside the vessel was raised from atmospheric, 1 bar$_{abs}$, to 5 bar$_{abs}$. These measurements were done using a gas flow provided by the distribution plate, but also using a gas flow coming from a single jet placed just above the distribution plate. In the second series the vessel was filled with aluminum-oxide particles with a d_{50} of 76 μm. Fines were added to this mix to raise the weight-percentage from 0% up to 50%.

In both series the bed behavior at different gas velocities settings and different heights is studied.

1.3 Safety

Because X-rays are dangerous to living organisms, it is important to contain them and make sure people who work with them know what they are doing. That is why the room in which the setup is housed is shielded using lead plates and inspected regularly by the safety authority (Stralings Beschermings Dienst). Running the setup under pressure also introduces hazards. The vessel could rupture and explode, which could seriously injure people. For that reason the setup can only be pressurized once the safety doors are closed. If these doors are opened, the vessel will be depressurized automatically. All safety information can be found in the separate safety report (Wagner (2011)). Fluidizing beds containing fine particles will generate dust. This dust can be dangerous if inhaled for an extended period of time, even though the particles themselves are not toxic. It is important to minimize the amount of dust that is released. Using personal protection, such as a surgical mask and safety glasses, helps protect people working with the setup.

1.4 Outline

This report is built up as follows:

- Chapter 2 contains the theoretical background of fluidized beds and will briefly discuss X-ray generation, detection and tomography.
- Chapter 3 will discuss the experimental conditions and the processing of the data that is retrieved from this setup.
- Chapter 4 shows the results of the measurements that have been done. In this chapter the accuracy and reliability of the measurements is also studied.
- Chapter 5 contains the conclusions that can be drawn from the research done. It also contains recommendations for future research in this area.

CHAPTER 2

Theory

In this chapter the basic theory behind fluidized beds, X-ray generation, detection and tomography is discussed. This theory will help interpret the results obtained later on, when measurements have been done.

2.1 Fluidized beds

When solid particles are transformed into a fluidlike state though suspension in a gas or liquid this is called fluidization. A fluidized bed is a bed of usually fine particles, contained in some kind of vessel, which is fluidized by passing a fluid upward though the bed. If the flow rate of the fluid is low, it will percolate through the void space between the particles. In this state it is called a fixed bed. Increasing the flow will lead to particles that are vibrating and moving in restricted regions, this is called an expanded bed. If the flow is raised further, a point is reached where all the particles are just suspended by the upward-flowing fluid. The bed is now at minimum fluidization.

In the next section the focus will be on beds that are fluidized using a gas, however many aspects are applicable to a liquid-fluidized bed as well.

As the gas velocity is increased, the bed will go from the fixed bed to the expand bed state, and eventually to the state in which it is at minimum fluidization. The pressure drop over the bed will be approximately proportional to the gas velocity. Once the gas velocity that is required for the minimum fluidization state has been reached, the pressure drop will remain roughly constant, even if the gas velocity is increased. This point is a clear indication that the minimum fluidizing velocity, u_{mf}, has been reached. The bed now exhibits fluidlike properties, such as a level surface that will flatten out again if it is disturbed. A graph that shows the pressure drop for the transition from a fixed bed to a fluidized bed can be seen in the lower part of figure 2.1.

The forces working on a particle in a fluidized bed are the drag force caused by the upward moving fluid and gravitational force caused by the weight of the particle.

(drag force by upward moving gas) = (weight of particles)

Or, worked out a bit more:

(pressure drop across bed) (cross-sectional area of tube) =
(volume of bed) (fraction consisting of solids) (specific weight of solids)

Using that the pressure drop over the bed, Δp_b, is always positive, this can be written as:

$$\Delta p_b A_t = W_{bed} = A_t L_{mf}(1-\epsilon_{mf})[(\rho_s - \rho_g \frac{g}{g_c})] \tag{2.1}$$

Where A_t is the bed cross-section, W_{bed} the bed weight, L_{mf} the height of the bed at minimum fluidization, ϵ_{mf} the voidage at minimum fluidizatoin, g the acceleration of gravity, g_c a conversion factor and ρ_s and ρ_g the density of the solids and the gas, respectively.

Rearranging this equation, we find the minimum fluidization conditions at

$$\frac{\Delta p_b}{L_{mf}} = (1-\epsilon_{mf})(\rho_s - \rho_g)\frac{g}{g_c} \tag{2.2}$$

If this equation is combined with the equation for the frictional pressure drop, like the Ergun equation (Ergun (1952)):

$$\frac{\Delta p_{fr}}{L_m} g_c = 150 \frac{(1-\epsilon_m)^2}{\epsilon_m^2} \frac{\mu u_0}{(\phi_s d_p)^2} + 1.75 \frac{1-\epsilon_m}{\epsilon_m^3} \frac{\rho_g u_0^2}{\phi_s d_p} \tag{2.3}$$

In this equation L_m is the height of the fixed bed, ϵ_m the voidage of the bed as a whole, μ the viscosity of the gas, u_0 the superficial velocity of the gas, ϕ_s the sphericity of a particle and d_p the particle diameter based on screen analysis.

For minimum fluidization conditions, this leads to

$$\frac{1.75}{\epsilon_{mf}^3 \phi_s} \left(\frac{d_p u_{mf} \rho_g}{\mu}\right)^2 + \frac{150(1-\epsilon_{mf})}{\epsilon_{mf}^3 \phi_s^2} \left(\frac{d_p u_{mf} \rho_g}{\mu}\right) = \frac{d_p^3 \rho_g (\rho_s - \rho_g) g}{\mu^2} \tag{2.4}$$

Here ϵ_{mf} and u_{mf} are the voidage and gas velocity in the minimum fluidization state, respectively.

For a summary on how to predict the onset of fluidization for various particles see Couderc in the book by Davidson (1985).
It must be noted that the exact minimum fluidization will sometimes differ depending on whether the velocity is increased until u_{mf} is reached or decreased until that point. Also a wider distribution in the size of the particles will make the exact onset of fluidization less clear; the transistion will be more gradual.

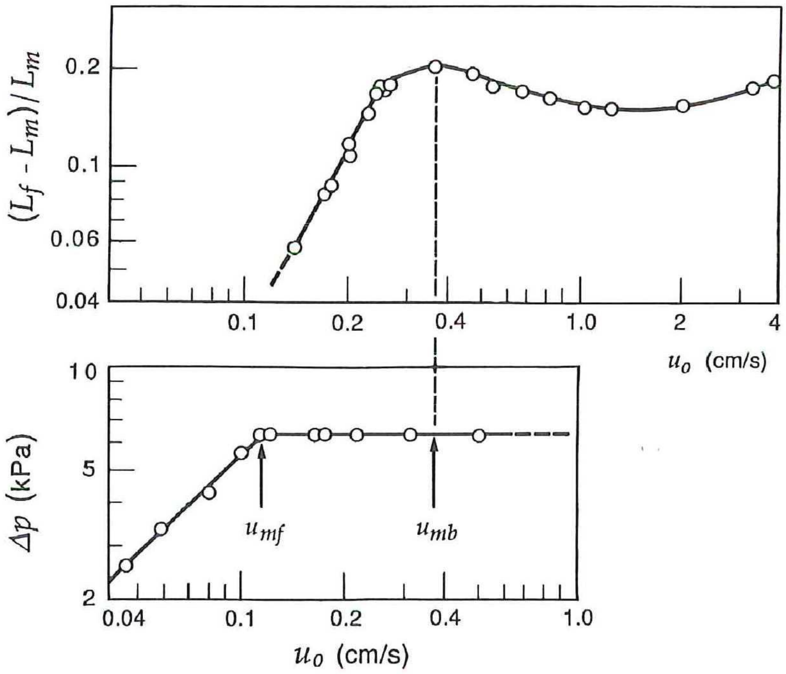

Figure 2.1: Relative bed expansion and pressure drop with increasing gas velocity, FCC catalyst $d_p = 64.7\mu$m (Kunii and Levenspiel (1991)).

As the gas velocity is increased the bed will expand further. If the gas velocity is increased enough, bubbles will start to form. This stops the expansion of the bed; the bed height will reduce slightly. The velocity at which this happens is called the minimum bubbling velocity, u_{mb}. This effect can clearly be seen in the upper part of figure 2.1.
For some types of particles there is a clear distinction between u_{mf} and u_{mb}, for others these two gas velocities are (nearly) the same. Different types of particles fluidize in different ways. A widely used way to classify the different types of particles is the so-called Geldart classification (Geldart (1973)).

2.1.1 Geldart classification

Because the fluidization behavior of different types of particles varies quite a lot, a classification based on the particle size and density has been developed by Geldart. This classification defines four distinct groups: A, B, C and D. An overview of the groups can be seen in figure 2.2.

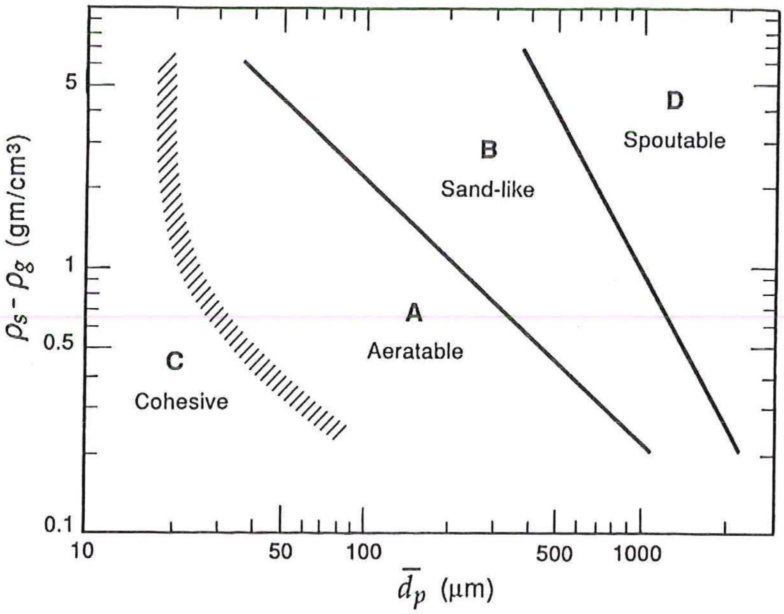

Figure 2.2: Geldart classification of particles for air at ambient conditions (Kunii and Levenspiel (1991)).

- Geldart A: Beds of this type of particles expand considerably before bubbles appear. Bubbles tend to split and coalesce frequently. This will result in a maximum bubble size of less then 10 cm. The bubbles have a tendency to form axial slugs. Even if there are only small bubbles present, there is a lot of circulation of the particles in the bed. Fines seem to act as a lubricant to make it easier to fluidize the bed. Aluminum oxide particles with a density of 680 kg/m^3 and a diameter of 76 μm are an example of a Geldert A powder.
- Geldart B: If these type of solids are fluidized, they will almost immediately start bubbling as soon as the gas velocity exceeds u_{mf}. The bubbles will grow roughly linear with the height above the distributor and the excess gas velocity, $u_o - u_{mf}$. To circulate these particles well, larger bubbles are required. Polystyrene spheres with a density of 625 kg/m^3 and a mean diameter of 607 μm are an example of B particles.
- Geldart C: These particles are difficult to fluidize: in small diameter bed they tend to rise as a plug and in larger beds channels will form through which the gas is passed. Mechanical agitation can make it easier to fluidize these beds.
- Geldart D: In beds of this type of particles bubbles tend to rise relatively slowly and coalesce to become larger. These beds are often operated in spouting mode, since this requires less gas to run. The drying of peas, roasting of coffee beans and gasification of coals are examples of processes that can be run in this way.

In figure 2.2 the boundary between A and C particles is not very clear, this is because some particles behave like an A-powder when fluidized, but will defluidize on a horizontal surface and block the pipes, like a C-powder.

2.1.2 Bed and bubble behavior

Depending on the type of particles and the gas velocity that is fed through the bed, a fluidized bed can exhibit different types of behavior. A proper state should be selected for the desired operation of the bed. A overview can be seen in Figure 2.3.

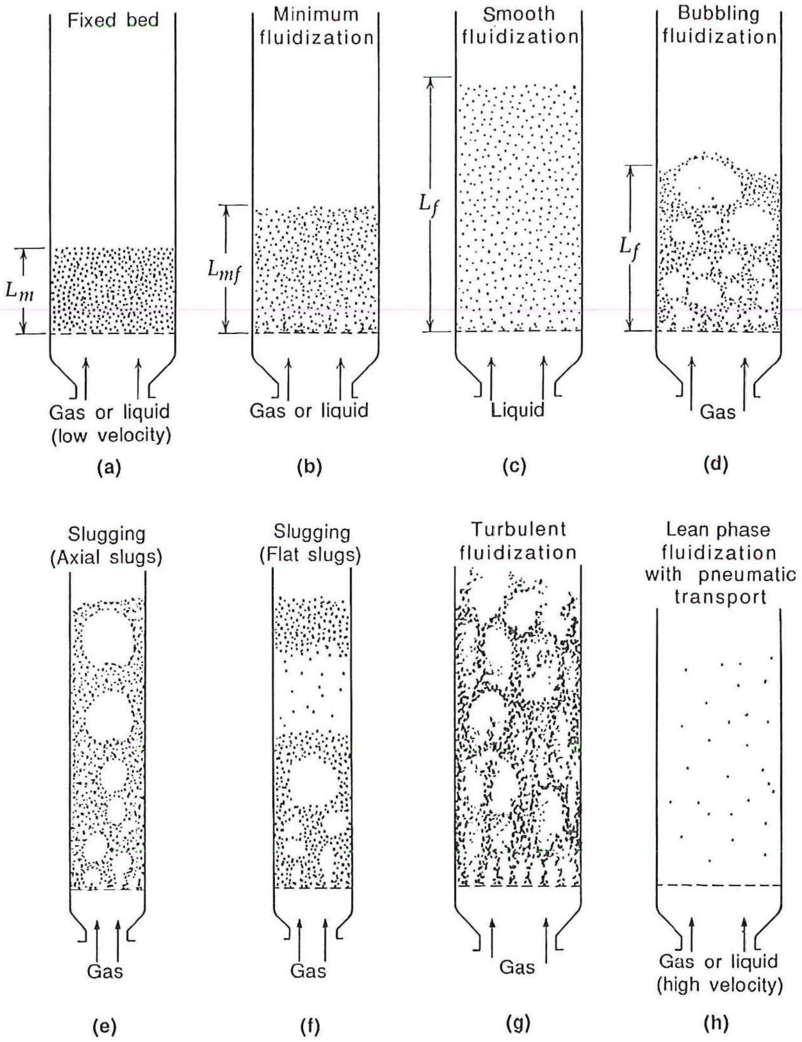

Figure 2.3: Various forms of contacting of a batch of solids by fluid; from Kunii and Levenspiel (1991).

Bubbles rising in the bed

Bubbling beds behave quite similar to bubbling liquids of low viscosity. Roughly all the gas in excess of that needed to just fluidize the bed passes through it in the form of bubbles. These bubbles rise with a speed that depends on their size and whether they interact with the wall of the vessel. The bubble rise velocity has been studied by many people and has been summarized by Clift and Grace in the book by Davidson (1985). The rise velocity has been related to the diameter of a sphere with the same volume as the bubble that is being studied in equation 2.5. This relation holds for bubbles that are no larger than 1/8 of the bed diameter.

$$u_{br} = 0.711(gd_b)^{1/2}, \quad \frac{d_b}{d_t} < 0.125 \tag{2.5}$$

Where u_{br} is the bubble rise velocity on top of the gas velocity, d_b and d_t are the bubble and bed diameters.

For bubbles larger than this a relation has been found based on work by Wallis (1969).

$$u_{br} = [0.711(gd_b)^{1/2}]1.2\exp(-1.49\frac{d_b}{d_t}), \quad 0.125 < \frac{d_b}{d_t} < 0.6 \tag{2.6}$$

For bubbles larger than this the bed should be considered slugging instead of bubbling. A relation has been found by Stewart and Davidson (1967). This relation (equation 2.7) assumes that the slugs will push the particles upward, which will make them rise at least at the excess gas velocity, but on top of that the bubble will rise inside of the slugs.

$$u_{br} = 0.35(gd_b)^{1/2} \tag{2.7}$$

The bubble rise velocity u_{br} is the speed a bubble has on top of the gas velocity that is used to fluidize the bed.

A slightly modified version of these equations were proposed by Hilligardt and Werther (1986) based on their experimental work.

$$u_{br} = \psi \cdot (u - u_{mf}) + 0.711 \cdot \nu \cdot \sqrt{gd_b} \tag{2.8}$$

Where u is the gas velocity. The parameters ψ and ν have been determined experimentally.

$$\psi = 0.8 \quad L_m/d_t < 1.7 \quad \text{Geldart A}$$

$$\psi = \begin{cases} 0.67 & L_m/d_t < 1.7 \\ 0.51 \cdot \sqrt{L_m/d_t} & 1.7 < L_m/d_t < 4 \\ 1 & L_m/d_t > 4 \end{cases} \quad \text{Geldart B}$$

$$\psi = \begin{cases} 0.26 & L_m/d_t < 0.55 \\ 0.35 \cdot \sqrt{L_m/d_t} & 0.55 < L_m/d_t < 8 \\ 1 & L_m/d_t > 8 \end{cases} \quad \text{Geldart D}$$

$$\nu = \begin{cases} 3.2 \cdot d_t^{0.33} & 0.05 < d_t < 1\text{m} & \text{Geldart A} \\ 2.0 \cdot d_t^{0.5} & 0.1 < d_t < 1\text{m} & \text{Geldart B} \\ 0.87 & 0.1 < d_t < 1\text{m} & \text{Geldart D} \end{cases}$$

$$\nu = \begin{cases} 0.63 & d_t < 0.1\text{m} \\ 2.0 \cdot d_t^{0.5} & 0.1 < d_t < 1\text{m} \\ 2.0 & d_t > 1\text{m} \end{cases} \quad \text{Geldart B}$$

Bubble shape and size

A frequently used model for bubbles in a fluidized bed, is the model proposed by Davidson and Harrison (1963). It assumes that there are no particles inside a bubble and that it is spherically shaped. As a bubble rises, the particles move aside, just like in a incompressible inviscid fluid. The bulk density of this fluid is $\rho_s(1-\epsilon_{mf})$. Further it assumes that the gas in the emulsion phase flows like a incompressible viscous fluid and must satisfy Darcy's law. It also assumes that far from the bubble the pressure gradient is undisturbed and that the pressure inside the bubble is constant. This is a so-called two-phase model. Bubbles can rise slower or faster that u_f, which is the gas velocity in the emulsion phase of the bed, u_{mf}/ϵ_{mf}. According to the Davidson and Harrison (1963) model, this will cause a difference in the way gas passes through a bubble.

In slow bubbles the gas enters the bubble at the bottom and leaves at the top. The gas uses the bubble as a kind of shortcut through the bed. However, an annular ring of gas does circulate inside the bubble, which moves it upward. This situation is illustrated in figure 2.4 (b).

If a bubble rises faster than the gas in the emulsion phase, the gas still enters at the bottom and leaves that the top, but it is swept around and returned to the bubble base. This causes a cloud to form around the bubble and prevents the recirculating gas mixing with the rest of the gas in the bed. This situation is illustrated in figure 2.4 (d) and (e). The size of the cloud is given by

$$\frac{R_c^3}{R_b^3} = \frac{u_{br} + 2u_f}{u_{br} - u_f} \tag{2.9}$$

Having a large amount of gas inside a bubble is a very unfavorable situation when the gas is passed through a bed to let it react with the solids. An overview of the flow inside and around a bubble, and the transition from slow to fast behavior can be found in figure 2.4.

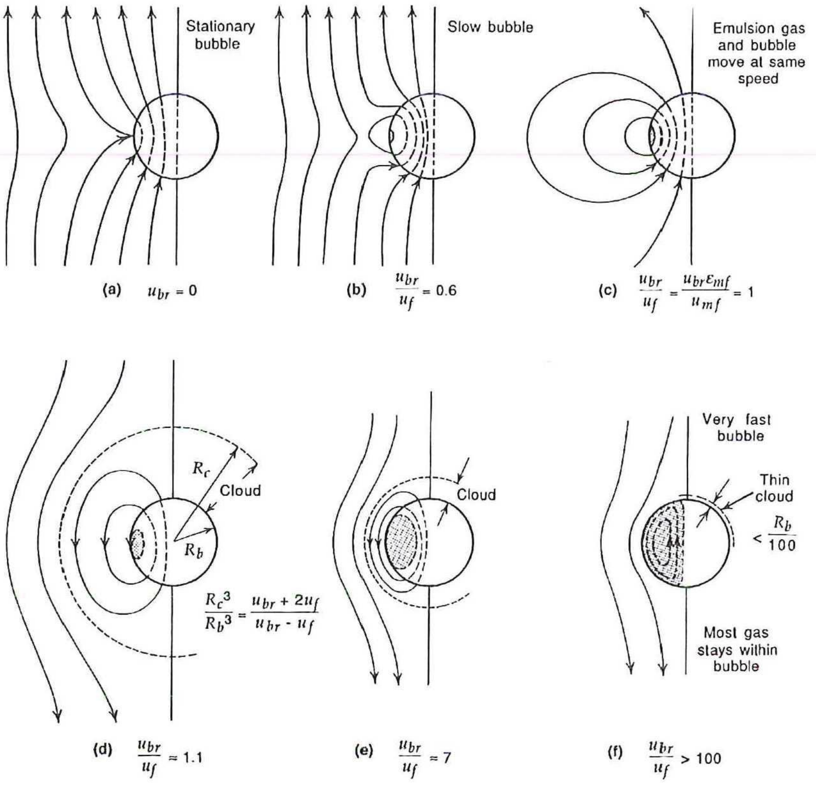

Figure 2.4: Gas streamlines in the region of a rising bubble, upper row are slow bubbles, the lower row shows fast bubbles. The streamlines are symmetric, but only drawn on the left (Kunii and Levenspiel (1991)).

Other models for bubbles in a fluidized bed (such as Stewart and Davidson (1967) and Briongos et al. (2011)) have also been developed, but the Davidson model is very elegant and simple, which makes it a good basis for understanding bubble behavior.

During it's way to the top of the bed a bubble will grow, because of coalescence with other bubbles. A model that is often used to describe this behavior has been developed by Darton et al. (1977). In a bed where no fine particles are present and the bubbles do not form slugs, equation 2.10 will give the spherical equivalent bubble diameter.

$$d_e = 0.54(u - u_{mf})^{0.4}(h_{bed} + 4\sqrt{A_0})^{0.8} g^{-0.2} \tag{2.10}$$

In this equation d_e is the spherical equivalent bubble diameter and h_{bed} is the height in the bed. A_0 is the catchment area. This is the area from which gas is drawn into the bubble stream. For a multi-orifice distributor this is the area of plate per hole. For a porous plate this will value will be in the order of tens of mm^2.

Other models have been proposed, such as Mori and Wen (1975), Rowe (1976), Werther (1976) and several others. Darton is one of the most simple and widely used models, so in this report that model will be used.

However, a maximum bubble diameter will eventually be reached. This size is caused by an equilibrium between the coalescence and the break up of bubbles. According to Mori and Wen (1975) the maximum diameter will be

$$d_{em} = 0.374(\alpha A_t(u - u_{mf}))^{2/5} \tag{2.11}$$

The value for α has to be estimated from measurement data; it was found that this is roughly 4.0. Bubbles can also be split by an effect known as kniffing, this has been observed by Rowe (1971). The roof of a bubble will develop a downward cusp, which then grows to split the bubble. Often one bubble is larger than the other one, which will result in the smaller one being absorbed back into the larger one.

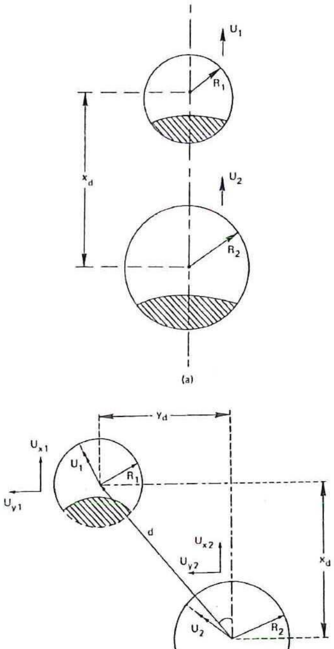

Figure 2.5: Bubbles that are close together will influence each other, whether they are vertically aligned (a) or not (b) (Clift & Grace).

If two bubbles are rising close to each other, the trailing bubble gets accelerated into the leading bubble. This is caused by the circulation of the gas around the bubble, which causes a low pressure area in the wake of a bubble. The trailing bubble might also be stretched out by the pull caused by the low pressure wake.
According to Clift and Grace in the book by Davidson (1985), the rise velocity of the leading bubble will be influenced slightly, but the velocity of the trailing one will be influenced more significantly. The closer the bubbles are in the vertical direction, the stronger they will influence each other. If the bubbles are vertically aligned the effects will also be more significant. A schematic representation of two bubbles close to each other can be seen in figure 2.5. Clift and Grave have developed a model for the bubble rise velocity of the leading bubble, U_1, and the trailing bubble, U_2, when they are vertically aligned.

$$U_1 = U_{b\infty 1} + \frac{U_2 R_2^3}{(x_d + R_1)^3} \tag{2.12}$$

for $x_d \geq R_1 + R_2$:

$$U_2 = U_{b\infty 2} + \frac{U_1 R_1^3}{(x_d - R_1)^3} \tag{2.13}$$

for $x_d < R_1 + R_2$:

$$U_2 = U_1 + U_{b\infty 2} \tag{2.14}$$

Here x_d is the vertical distance between the bubble centers. R_1 and R_2 are the radii of the leading and trailing bubble, respectively. $U_{b\infty}$ is the rise velocity of an isolated bubble.
If the bubbles are not vertically aligned, the bubble velocities must be split up in to their x and y components. Here the influence of the trailing bubble on the leading bubble is neglected.

$$U_{x1} = U_{b\infty 1} \qquad U_{y1} = 0 \tag{2.15}$$

for $(x_d - R_2)^2 + y_d^2 > R_1^2$:

$$U_{x2} = U_{b\infty 2} + l_{21} U_{b\infty 1} \qquad U_{y2} = m_{21} U_{b\infty 1} \tag{2.16}$$

for $(x_d - R_2)^2 + y_d^2 < R_1^2$:

$$U_{x2} = U_{b\infty 2} + U_{b\infty 1} \qquad U_{y2} = 0 \tag{2.17}$$

Here y_d is the horizontal distance between the bubble centers. l_{21} and m_{21} are interaction coefficients defined by Clift and Grace.

2.1.3 Effect of pressure

In many applications of fluidized beds the bed is operated at high pressure or high temperature so that more feed can be processed without the need for a larger bed. The effects of running a fluidized bed at elevated pressures have been studied by Hoffmann and Yates (1986). The raising pressure will increase the density of the gas, which in turn will lower the minimum fluidization velocity, as seen by for instance Olowson and Almstedt (1991). This effect is predicted by equation 2.4. The dense phase voidage in beds of smaller particles (d_p < 100 μm) increases as the pressure is raised. This leads to more gas passing through the bed in the dense phase, so less bubbles will be formed. In beds containing larger particles this effect will be much less noticeable. The bubble size for beds containing small particles, such as Geldart A particles, will decrease drastically. For beds containing larger particles, Geldart B particles, this effect is much smaller, according to Weimer and Quarderer (1985).

2.1.4 Effect of fines

According to Abrahamsen and Geldart (1980) the ratio between u_{mb} and u_{mf} strongly depends on the weight fraction $P_{45\mu m}$, of fines (d_p < 45 μm) added to the particles in the bed. The relation they found is, in SI units,

$$\frac{u_{mb}}{u_{mf}} = \frac{2300\rho_g^{0.13}\mu^{0.52}exp(0.72P_{45\mu m})}{d_p^{0.8}(\rho_s - \rho_g)^{0.93}} \tag{2.18}$$

If the weight fraction of the fines raised from 0% to 30%, this will cause an increase of 24% in the ratio between u_{mb} and u_{mf}. The addition of fines will also cause the mean bubble size to decrease. Although at very low superficial gas velocities (< 2 cm/s) the bubbles have been seen to grow with increased fines content. Why this is happening is not very clear, according to Beetstra et al. (2009). The effect of fines on the bubble size can be seen in Krishna (1988). What exactly causes this is not yet fully explained. It is often speculated that the fines will act as a kind of lubricant. This lowers the apparent viscosity of the dense phase and this leads to smaller bubbles and a more uniform gas-solid distribution.

Fluidized beds come in many different shapes and sizes, ranging from small (a few cm diameter) laboratory setups to large (8 m diameter) fluid catalytic crackers used at oil refineries. To get an idea of what fluidized beds can be used for in the (petrochemical-) industry, see Chapter 2 of Kunii and Levenspiel (1991).

2.2 X-rays

The use of X-rays is quite common nowadays. They give us the opportunity to study phenomena that would stay hidden when using convention light and our eyes or a camera. X-radiation, also known as Bremsstrahlung or Röntgen radiation, is a form of electromagnetic radiation. The wavelength of these X-rays range from roughly 0.01 nm to 100 nm, which corresponds to an energy of about 120 eV to 120 keV. Their place in the electromagnetic spectrum can be seen in figure 2.6. This energy is the energy of the individual photons of which the rays are made up, which can be calculated using $E = \frac{hc}{\lambda}$. Where E is the energy of the photon, h Planck's constant, c the speed of light and λ the wavelength.
When X-rays are used to study an object, the result is a attenuation profile of the object. X-rays reveal the different materials that are inside the object, by showing their ability to absorb or reflect X-rays. If, for example, a human body is studied using X-rays, the different tissues and bones will show up on the radiographic film placed behind the body, because of their difference in ability to absorb X-radiation. How much radiation is absorbed depends strongly on the density of the material. Using the Lambert-Beer law the amount of radiation that will be absorbed can be calculated:

$$T = \frac{\Phi(x)}{\Phi_0} = Be^{-\mu_{material} x} \tag{2.19}$$

Here T is the normalized transmission, $\Phi(x)$ the photon fluence at distance x, Φ_0 is the initial photon fluence, B is the incoming radiation and $\mu_{material}$ the linear attenuation coefficient.
It must be noted that this equation assumes that the radiation is monochromatic and no build-up occurs. Build-up occurs when radiation interacts with materials and causes more photons than originally generated to reach the object. There are several ways in which X-rays can interact with materials. These are:

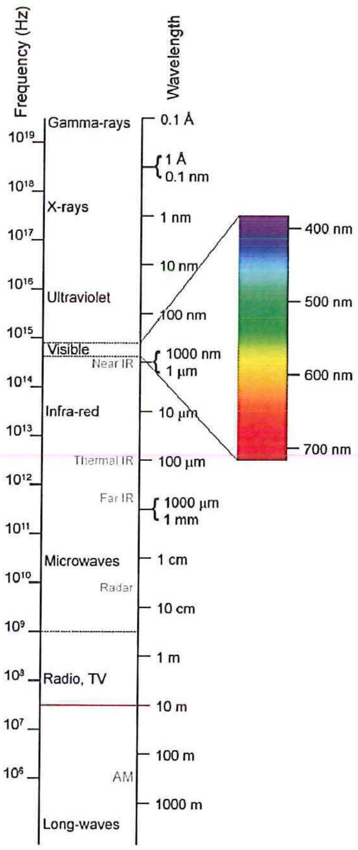

Figure 2.6: Overview of the in electromagnetic spectrum (Wikipedia).

- Photoelectric effect
- Compton effect
- Pair formation
- Rayleigh scattering

Which of these effects dominate depends on the atomic number Z of the material and the energy of the photon. Figure 2.7 shows which effects are most important. The contribution of Rayleigh scattering is relatively low, so it is not included in this graph.

The photoelectric effect occurs when an incoming photon transfers all its energy to a (strongly) bound electron. This electron leaves the atom, and its place is filled by another electron. Because there is a binding energy difference between the new and old electron state, the electron will send out a photon, or X-ray, with this energy.
When Compton scattering occurs, an incoming photon hits a loosely bound electron that is part of the atom of the material. This electron is scattered and so is the photon. Energy conservation requires the total of the energies of the scattered electron and photon to be equal to the energy of the original incoming photon.

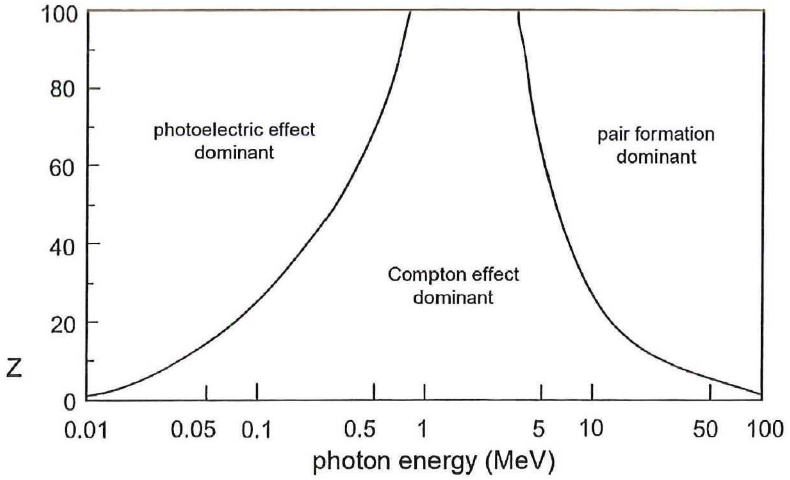

Figure 2.7: Most dominant effect as a function of X-ray energy and atomic number Z (Brouwer and van den Eijnde (2008)).

During pair formation an incoming photon is converted into an electron and a positron. These two particles together have a kinetic energy of $E_{photon} - 1022$ keV, and will leave the atom. Later the positron will annihilate with another electron and two photons with each an energy of 511 keV will be formed.
Rayleigh scattering is a form of elastic scattering of the incoming photons. This occurs most at lower X-ray energies. This form of scattering is used for X-ray diffraction research.
Since the amount of X-ray absorption strongly depends on the density of the material, lead plating is frequently used to contain the radiation.

2.2.1 X-ray generation

X-rays can be generated using an evacuated tube. These tubes evolved from the experimental Crookes tubes, that produced X-rays as a side effect. In an X-ray tube electrons are accelerated from a cathode to an anode, through the evacuated tube, by a high voltage. The voltages across the cathode and anode typically range from 30 to 150 kV. A schematic overview of such a tube can be seen in figure 2.8. Once an electron reaches the anode, it will interact with the anode material. If an electron passes close by the nucleus of an atom of the anode material, it will be deflected because of its charge. This deflection causes the electron to lose energy, which is emitted in the form of Bremsstrahlung, or X-rays, see figure 2.9. Roughly 1% of the energy is converted into useful X-rays, the rest of the electrons undergo many collisions and convert their energy into heat. That is why a modern X-ray tube has a rotating anode. In this way only part of the anode is used at a time, so the other parts can cool. These tubes are usually liquid cooled. This makes it possible to generate X-rays with a higher energy. Depending on the type of material of the anode and the accelerating voltage, different X-ray spectra can be generated. If an incoming electron has an energy of E_{photon}, the energy of the emitted photons will range from 0 to E_{photon}. A continuous spectrum of photons will be generated. Depending on the type material used for the anode, several characteristic lines will be visible in the spectrum. These lines are caused by electrons filling holes in the atom shell, which in turn are caused by the incoming electrons interacting with bound electrons and ejecting them. Figure 2.10 shows such a spectrum for a tube set

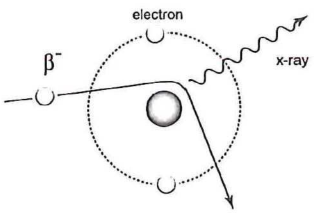

Figure 2.9: Interaction between incoming electron and nucleus that causes Bremsstrahlung (Brouwer and van den Eijnde (2008)).

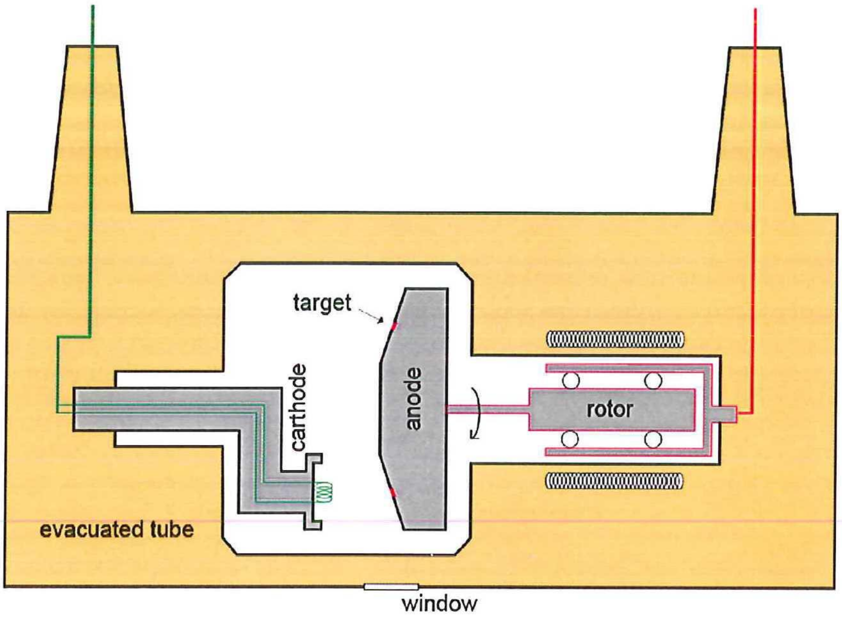

Figure 2.8: Simplified schematic overview of X-ray tube (Wikipedia).

at 120 keV.

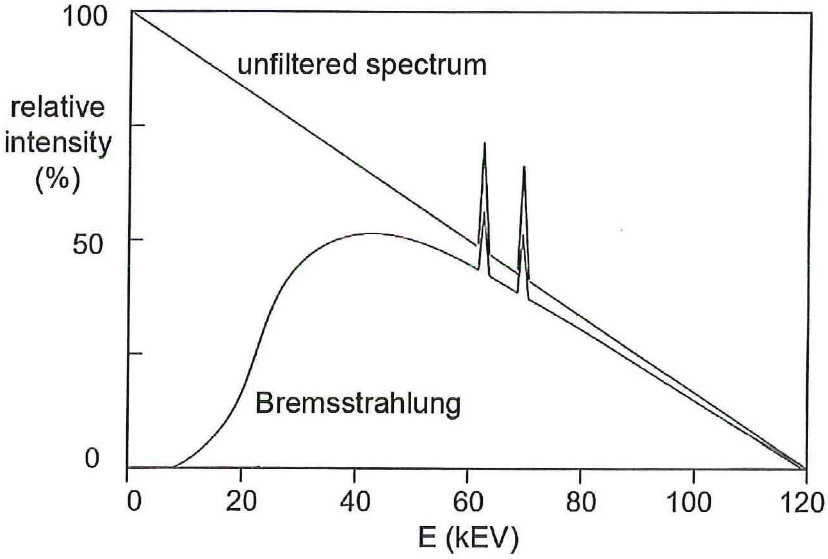

Figure 2.10: Typical X-ray tube spectrum, unfiltered and filtered (Brouwer and van den Eijnde (2008)).

2.2.2 X-ray detectors

There are several types of X-ray detectors. They are usually classified as either an ionization or a scintillation detector.

In an ionization detector there are two electrodes, over which a voltage is applied. A photon can be captured and will cause an electron-ion pair to be formed due to ionization. If the voltage is high enough

to prevent recombination, the electron will go to the anode and the ion to the cathode. This will create a current which is a measure for the amount of photons. A Geiger-Müller tube of the well-known Geiger counter works using this principle. There are also solid-state ionization detectors. Here the ions do not move, but the electrons do and this will also create a current.
Scintillations are flashes of light that are produced by certain materials when they are exposed to high energy photons. There are various materials can be used to detect X-rays in this way. Scintillators are defined by their short fluorescence decay times ($\sim 10^{-8}$ s) and their own transparency to the wavelengths they produce. A device that utilizes this mechanism is a photomultiplier tube (PMT). Inside a glass vacuum tube a photocathode, several dynodes and anode are placed, see figure 2.11. If a photon interacts with the photocathode electrons will be emitted. These will be focused on the first dynode, which in turn will multiply the electrons by the process of secondary emission. In this way the cascade of electrons will generate a peak signal at the anode. In this way each scintillation pulse will produce a clear signal. Photodiodes are solid-state devices that contain a p-n junction, usually with an intrinsic (undoped) layer in between them. These devices are called PIN photodiodes. Light absorbed by the intrinsic layer generates electron-hole pairs that are collected at the anode and cathode, respectively. This generates a measurable signal. A big advantage of photodiodes is their relatively small size and low price. This allows them to be packed into arrays, for example. They can be operated in counting mode, where individual photons and their energies are detected, however the count rates can not be too high. But they can also be run in integral mode, where they give an output proportional to the integral radiant energy fluence rate. The number of photons hitting a detector can be modeled as a Poisson process. The stochastic nature of photon counting results in an uncertainty in the measurement values.

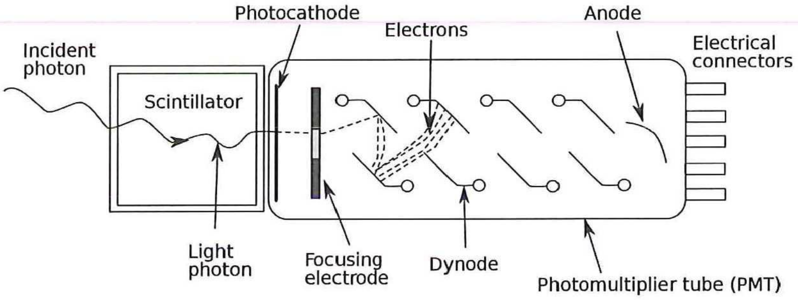

Figure 2.11: Schematic overview of a photomultiplier tube (Wikipedia).

2.2.3 Beam hardening

As mentioned before, the attenuation of the energy of X-rays when passing through a substance is described by the Lambert-Beer law, equation 2.19. This equation only holds for monochromatic beams and homogeneous materials. The Compton scattering and photoelectric cross section will be different for different photon energies. The result is that relatively more low energy photons are absorbed and the beam will become relatively rich in high energy photons. This effect is known as beam hardening.
When the attenuation of the X-rays is used to accurately detect the amount of matter it has passed through, a simple two point calibration will not give accurate results. A way around this is to take multiple calibration points and determine an effective attenuation coefficient. This has been described by Alles and Mudde (2007).

A more detailed treatment of X-rays and their effects on various materials can be found in, for example, Novelline (1997).

2.3 Tomography and reconstruction

Quickly after the discovery of X-rays in the 1890's it was noticed that the 'shadow' of an object can be displayed on a photographic film. This imaging technique is known as projection radiography. It is still used today in many applications, ranging from the examination of broken bones to airport luggage screening. This projection shows a superposition of all the details inside an object. This can lead to a confusing image, that is difficult to interpret. To overcome this problem, several radiographs of an object can be taken from different angles. If the object is studied from many different angles a complete 2D cross-section can be made using computer tomography (CT). This is shown schematically in figure 2.12. The more images are taken from different angles, the more reliable the reconstructed cross-section will be. Medical CT scanners obtain multiple radiographs by rotating the source and detector around the object, usually a patient. This patient must lay still during the time it takes to record the data. This is typically less then one second. These rotating systems produce high resolution cross-sections, but at a relatively low frame-rate, several frames per second at most. This is not suitable for a fluidized bed, where the time scales are much smaller. To overcome this problem there are two possibilities, either move the source very rapidly (see Hampel et al. (2005)) or install multiple static sources. For the setup at the Kramers Lab the latter option was chosen.

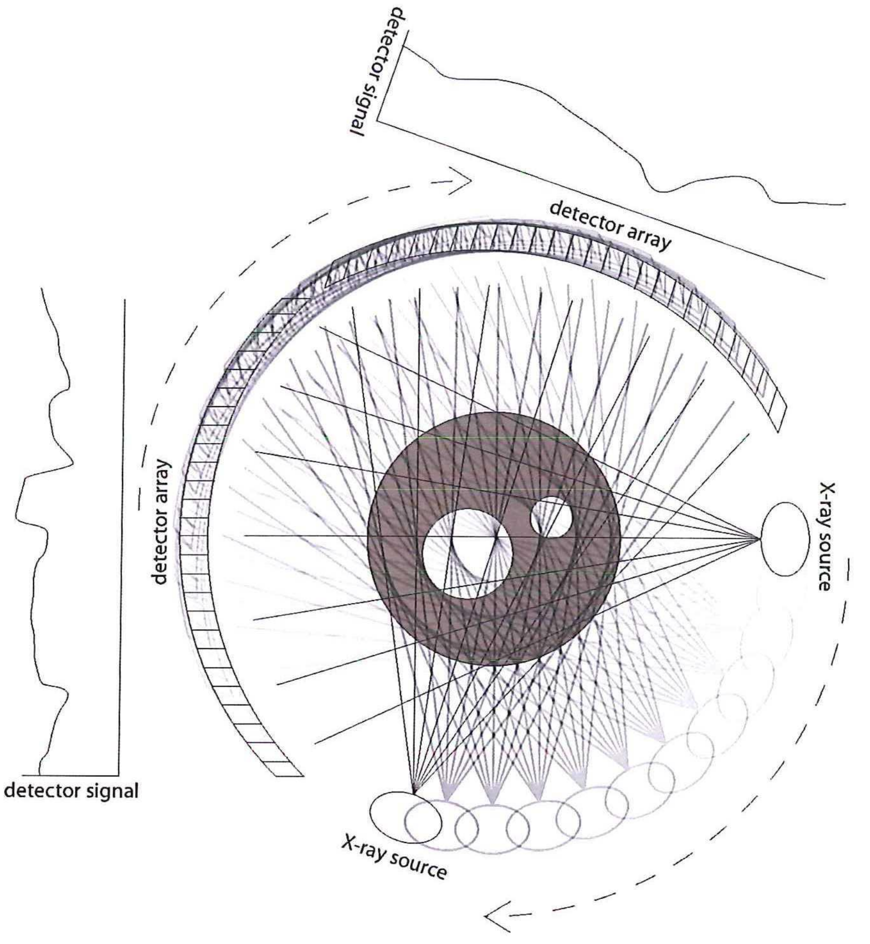

Figure 2.12: Schematic overview of a CT scan. The object is studied from many different angles, each producing a different detector array signal. Using this data a reconstruction is made.

2.3.1 SART with OSL algorithm

For limited data sets an iterative image reconstruction technique will provide more flexibility than a Fourier transform based method, such as a Radon transform. This flexibility comes at the expense of the reconstruction speed; it will be significantly lower. The reconstruction of the data of from the setup is an ill-posed problem in the sense of Hadamard, which means there can be many solutions or none at all.

The method used to process the measurements from our setup is the Simultaneous Algebraic Reconstruction Technique (SART), developed by Andersen and Kak (1984). This is an iterative reconstruction method, which means that it tries to minimize the mismatch between the reconstructed image and the attenuation map obtained from the measurements. The Kaczmarz algorithm (see Kaczmarz (1937)) ensures that if there is a unique solution, the method will always converge to that point. This algorithm is the basis of the Algebraic Reconstruction Technique (ART). SART is different from ART in the fact that instead of updating pixels on a ray-by-ray basis, SART simultaneously applies the average of the corrections generated by all rays to a pixel. This reduces the salt and pepper noise at the cost of the reconstruction time. The SART is given by:

$$\mu_k^{(n+1)} = \mu_k^{(n)} + \frac{\omega}{w_{+,k}} \sum_{i=1}^{M} \left[\tfrac{p_i - \tilde{p}_i}{w_{i,+}} w_{ik} \right] \tag{2.20}$$

Here $\mu_k^{(n)}$ is the guess of the nth generation of the attenuation coefficient of pixel k. ω is the detector energy response function. $w_{+,k}$ represents the total contribution of the kth pixel to all ray sums. M is the amount of detectors used. p_i is the ray sum of the ith ray. $w_{i,+}$ gives the relative contribution of the kth pixel to the ith ray sum. w_{ik} is the weighting coefficient that represents the contribution of ray i to pixel k.

Also

$$\tilde{p}_i = \sum_{k=1}^{N} w_{ik} \mu_k^{(n)} \tag{2.21}$$

Where N is the total number of pixels. And $w_{i,+}$ and $w_{+,k}$ are defined as

$$w_{i,+} = \sum_{k=1}^{N} w_{i,k} \qquad w_{+,k} = \sum_{k=1}^{M} w_{i,k} \tag{2.22}$$

In a paper by Jiang and Wang (2003) it has been shown that the SART produces a maximum likelihood estimate for the attenuation map, if the errors are purely stochastic and have a Gaussian distribution.

The One Step Late method ensures that the SART does not try to minimize the mismatch between the reconstruction and the data at a local minimum. OSL tries to find the overall minimum in the mismatch. The modified OSL method by Alenius and Ruotsalainen (1997) produces images that maintain a high resolution while there is a good amount of noise reduction.

For more information on various reconstruction techniques see the book by Kak and Slaney (1989).

CHAPTER 3

Experimental setup

This chapter will discuss the X-ray setup that was used to perform the measurements. It will also describe that way the measurement data was used to extract useful information.

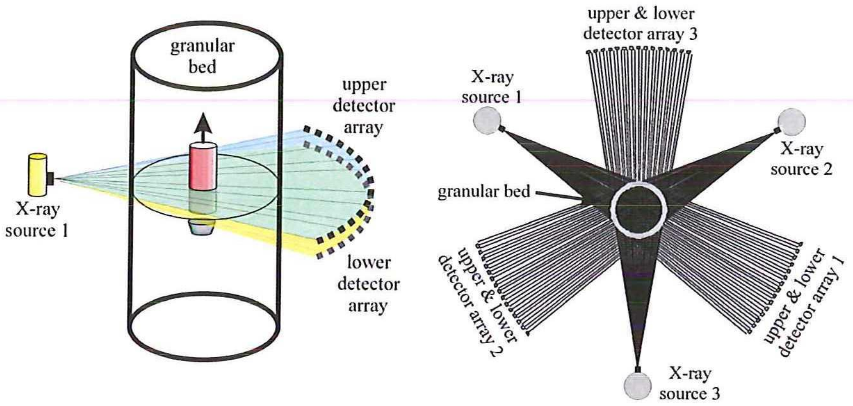

Figure 3.1: Schematic of the X-ray setup. Left: side view showing only one source and its two detector arrays for clarity. Right: top view of complete setup.

3.1 Setup construction

The setup consists of three X-ray sources and three double detector arrays. These sources and detectors are centered around the object. Because the detector banks all three have two detector arrays right above each other, two parallel measurement planes are studied. In this way it is possible to determine the speed of a passing object, because the vertical separation between the two planes is known; 1.86 cm (Mudde (2011)). For a schematic overview see figure 3.1.

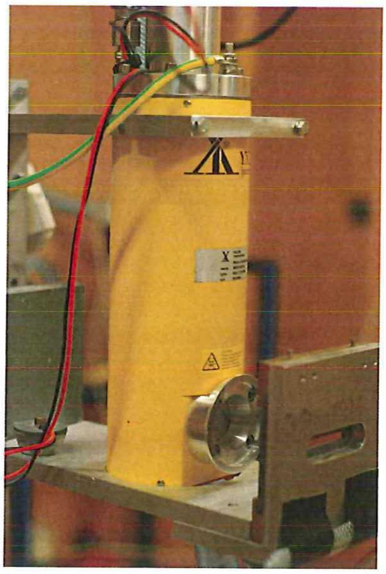

Figure 3.2: Picture of one of the X-ray tubes in the setup with the lead collimator in front of it.

The data from the detectors is recorded at 2.5 kHz and stored using a National Instruments CompactRIO embedded control and acquisition system. This system is controlled using a host-pc running LabView. One minute of measuring results in about 100 MB of binary data. This data is later used to reconstruct the bed cross-sections.

3.1.1 X-ray tubes

The three X-ray sources used in the setup are YXLON Y.TU 160-D06 tubes. A picture of one of the tube is shown in figure 3.2. These tubes have a maximum voltage of 160 kV and a maximum current of 12 mA. The tubes are water cooled and are able to operate for any length of time that is desired. In front of the tubes a lead collimator is placed to create a flat measurement plane. These collimators also reduce the amount of scattered radiation. The tubes are controlled by three YXLON MGC41 control units. This makes it possible to fire all X-ray sources at once, although settings can be set for each tube individually. The tubes are usually set to 150 kV and depending on the type of vessel and particles inside it, a suitable current is selected. A higher current gives a clearer signal, but it might also overexpose the detectors. It is possible to use a higher current and shield the detectors using copper plates. This will absorb part of the radiation and prevent overexposure.

Prolonged exposure to X-rays is dangerous to living organisms. For this reason 5 mm lead plates are mounted on the walls and underneath the floor of the measurement room. The ceiling of the measurement room is fitted with 2 mm lead plating. The experiments are controlled from outside the measurement room. This control room is shielded from radiation and safe to work in during measurements. The doors that close the measurement room have an interlock system that prevents the X-ray tubes from working if their are not closed properly. Also the amount of radiation in the control room is constantly monitored using thermo-luminescence dosimeters which are read out periodically by the Stralings Beschermings Dienst. For a more elaborated description of the safety measures taken see the safety report by Wagner (2011).

3.1.2 Detector arrays

The detector arrays consist of two planes of each 32 Hamamatsu S1337 - 1010BR detectors. These are $CdWO_4$ scintillation crystals, which are optically coupled to the PIN photodiode. Their crystal size is 10 mm x 10 mm x 10 mm. These detectors are installed on a small printed circuit board (right of figure 3.3) which are mounted in a curved plastic arc. The curvature of this arc is such that all detectors are aimed directly at the X-ray tube on the opposite side of the setup. The measurement signal of the detectors is fed through a 12-bit ADC at 2.5 kHz and stored on the CompactRIO. This data is later used to reconstruct the tomograms. The detectors arrays are shielded against scattered X-rays using a lead shielded casing. The left of figure 3.3 shows one of the three detector banks can be seen without the lead shielding. Two copper plates are mounted to prevent overexposure.

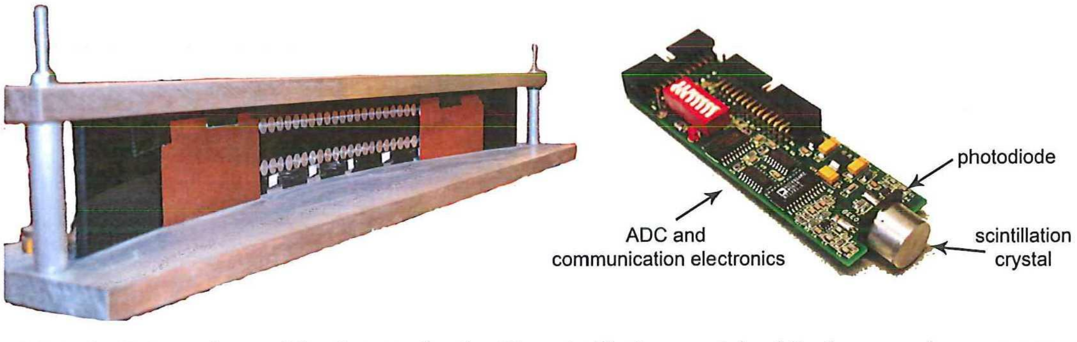

Figure 3.3: Left: Picture of one of the detector banks. The scintillation crystals of the lower and upper arrays can be seen, some with copper plating in front of them. Right: One of the in total 192 detector boards close up.

3.1.3 Vessel containing fluidized bed

The object in the middle of the setup could be anything of interest, but for this study only round columns have been used. The pressurized measurements were done using a stainless steel column with an inner diameter of 25 cm. The column wall has a thickness of 2 mm and is pressure tested up to 10 bar using water. The various parts of the column are connected using 12-bolt flanges and rubber gaskets. The bolts are tightened in a criss-cross pattern using a significant amount of torque. This is needed to prevent leaks at higher pressures. The main part of the column is 70 cm high and another 50 cm part can but put on top. To seal the vessel, a stainless steel lid with hose connections is mounted on top. This column is filled using 607 μm polystyrene particles.

The fines measurements were done using a perspex column with an inner diameter of 24 cm and a wall thickness of 5 mm. Here there are also two parts, a 70 cm high main section and a 50 cm extension. There is another 50 cm extension that can be placed on top, for extra room inside the vessel. The vessel can be sealed using a perspex lid with hose connections. Between the various parts of the perspex column rubber O-rings are used to prevent leaks. The 12 bolts are tightened by hand in a criss-cross pattern. This column is filled using 80 μm aluminum oxide particles.
Both the steel and perspex column are mounted on top of a stainless steel wind box. This wind box has a one inch hose connection which directs the gas flow downward inside the box. This ensures a uniform distribution of gas through the bronze sintered distribution plate in the top of the wind box. This plate has pore sizes ranging from 30 to 70 μm and a thickness of 7 mm.
Roughly 11 cm above the distribution plate a nozzle is placed which can function as a single jet to inject gas, as can be seen in figure 3.4. When this is done, the bed is usually fluidized just below the minimal bubbling velocity using the distribution plate. So bubbles will immediately start to form at the single jet orifice. The inner diameter of this capillary is 4 mm. The center of the fluidized bed is 71.5 cm from the X-ray tubes and 85.8 cm from the detectors.

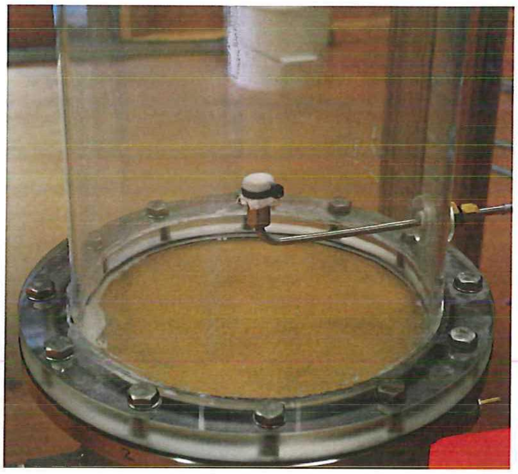

Figure 3.4: Picture of the single jet above the distribution plate inside the perspex column. The outlet of the nozzle is covered with a cloth to prevent particles from entering the nozzle when it is switched off.

It is also possible to study other objects such as smaller vessels or objects falling through a fluidized bed. For smaller objects the spatial resolution can be improved by placing the object close to one of the sources. Now the other two sources and detector arrays do not contribute anything. But the higher resolution data from one source can also be valuable.

3.1.4 Gas flow and pressure control

For the fluidization process the gas flow rate must be monitored and maintained at a constant value. To do this a Brooks 5851 was used for flows up to 100 l/min, a Brooks 5853S for flows up to 300 l/min and a Bronkhorst T15-AAD-99-V for higher flows. For the pressurized measurements a Bronkhorst P-502C was used to maintain the correct pressure. The pressure sender was attached to the top of the vessel. The control value was adjusted to that reading. The flows and pressure can be controlled from outside the measurement room. The vessel will only pressurize if the X-ray safety circuit is closed. This ensures that the doors are closed so that if the vessel should rupture it will not harm anyone.

It is important to note that these flow controllers indicate a volumetric flow, but actually measure mass flow. So if measurements under pressure are done these need to be corrected for the increased gas density.

3.1.5 Dust solution

When fluidizing small particles a significant amount of dust will leave the top of the vessel. This is unwanted because it will cover the measurement room and all devices inside it with dust. And because mostly small particles will become airborne, the amount of small particles in the bed will be reduced during the time that the bed is fluidized. Also inhaling large amounts of dust can be dangerous for people working in the area. All of these things are unwanted and call for an effective solution.

One option would be to install a cyclone in the outlet of the vessel. However, because the dust particles will be quite small (typically $< 40\mu$m) and the gas flow rates quite high (up to 300 l/min), the design and manufacturing of this cyclone will not be so easy. Multiple cyclones might be required to make these gas flow rates possible. Returning particles from the cyclone to the fluidized bed also requires a system such as a hopper. This is especially difficult in a pressurized environment. That is why a much simpler solution was developed.

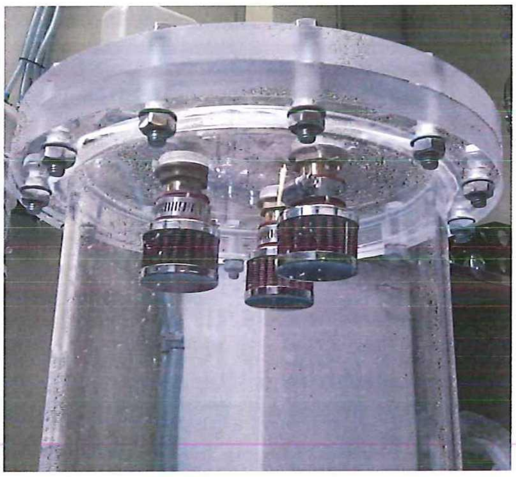
Figure 3.5: Picture of the filter setup inside the perspex column.

It is possible to install filters onto a plate at the top of the vessel, as shown in figure 3.5. These filters can be cheap paper-type automotive filters, frequently used for motorcycles or crankcase ventilation. These filters will prevent particles from leaving the vessel. If the filters are tapped by hand in between measurements, the caught particles will fall back into the bed. It is important to prevent the filters from clogging, by tapping them frequently. If the filters get clogged, the pressure inside the vessel will start to rise and the gas velocity will decrease. Installing a 50 cm column extension will increase the time that the setup can be run before the filters get clogged. Also installing multiple filters will reduce the risk of them clogging up. It is possible to use these filters in a pressurized environment in the future.

In the future it would be possible to expand this setup using two more sources and detector arrays. The data acquisition system is ready for this upgrade. The upgrade will improve the resolution, but this will require more space in the measurement room and processing times will be longer.

3.2 Reconstruction

After the data has been recorded using the X-ray setup, the attenuation signals from the detectors can be reconstructed into images of the cross-section of the bed. But also the raw data from the detectors can tell a lot about what is happening inside the bed.

3.2.1 Calibration

Because of the effects of beam hardening it is not possible to suffice with a simple two point calibration, one being a completely filled bed, the other completely empty. For every single detector a calibration of multiple points, including fully empty and fully filled, has to be made. In this way the detector signal is known for different path lengths through the bed. A picture of this process and a graph of the data used to calibrate one detector can be seen in figure 3.7.

Through the data points a smooth line can be fitted, so the corresponding path length for a given detector signal can easily be found. This information is used to reconstruct the images. The function that is used to fit through the calibration point is $A_{cal} + B_{cal} \cdot \exp(-x/C_{cal})$. This calibration curve has no direct

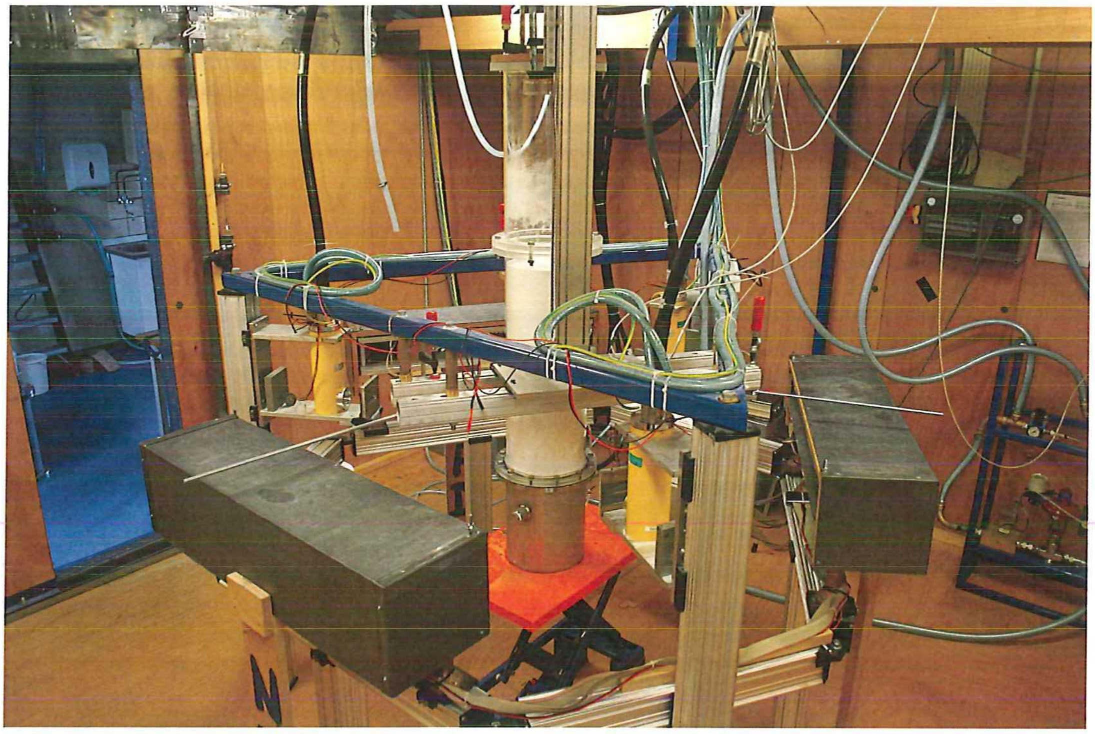

Figure 3.6: Picture of the tomography setup with the perspex column in place.

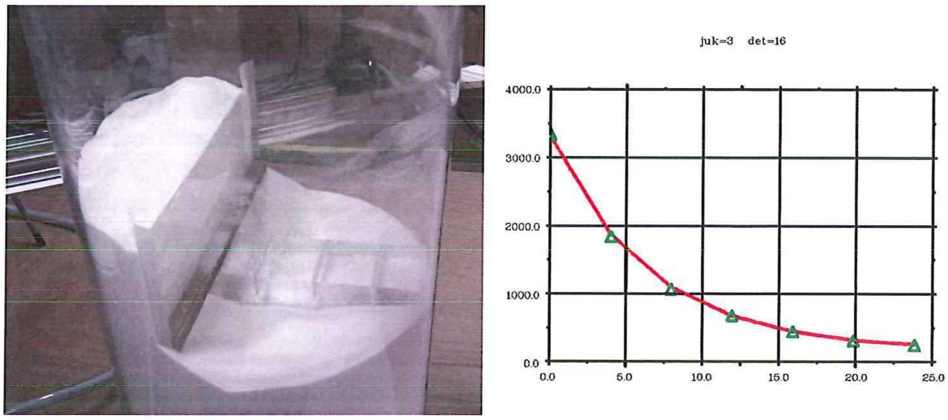

Figure 3.7: Left: process of calibrating setup using partially filled column. Right: data used for the calibration of a single detector for a 76 μm aluminum oxide bed with the X-ray tube at 150 kV and 0.7 mA.

physical meaning, but it can be seen as a measure for the effective attenuation coefficient.
It is important to perform this calibration very carefully, as it will affect all the reconstructions made using this calibration. As long as the tube settings, bed contents and vessel do not change this calibration can be used. However, there appears to be a kind of daily drift in the detector signals. Doing a calibration every day would take a lot of time and is not very practical. Instead a reference measurement is done every day of a completely filled bed. This is compared to the completely filled bed during the calibration and the measurement data is adjusted accordingly in the reconstruction program.
The alignment of the entire setup must not change either. For the X-ray tubes and the detectors this is no problem as they are attached to a rigid steel and aluminum frame. The column containing the fluidized bed however is standing on top of a height-adjustable table. When a high gas flow setting is used the vessel will shake quite significantly. Also moving the table up and down will slightly distort

the alignment. If this misalignment becomes too large the calibration will no longer be valid. To prevent this the column is held in place by three rods, which are attached to the metal frame of the X-ray tubes. This ensures the column remains centered and does not move during measurements.

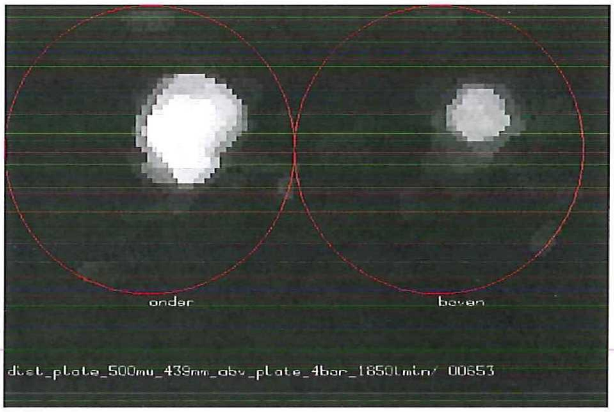

Figure 3.8: Reconstructed images of both lower and upper measurement planes. The inner wall of the vessel is shown by the red circle.

3.2.2 Reconstruction

The SART reconstructs the cross-section of the bed on a grid of square pixels. Previously done research (Mudde et al. (2008)) has determined that for a three source setup a 55 x 55 pixel grid gives the best trade off between resolution and processing time. For the 25 cm column this results in a pixel size of 4.5 mm x 4.5 mm. For the 24 cm column the pixel size is 4.4 mm x 4.4 mm. This results in reconstructions as shown in figure 3.8. The SART is an iterative technique. It will stop when convergence has been reached or when a certain amount of iterations have been done. Again, previous research has indicated that 400 iterations is sufficient. The algorithm takes the average of 10 samples or each detector. This will result in frame rate of 250 images per second. The pixels that are outside the vessel will be given a value of 0. The value inside a bubble will be 1.

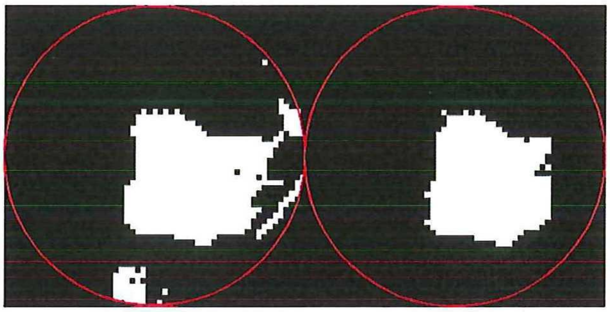

Figure 3.9: Left: original reconstructed image after thresholding, Right: after morphological opening. The inner wall of the vessel is shown by the red circle.

When using these settings for the reconstruction program, each single image takes about 2.6 seconds to be reconstructed. To reconstruct both measurement planes of a 60 seconds measurement will take about 22 hours on a modern single core CPU. The amount of disk space that is required for the (uncompressed) output of this reconstruction will be about 2.2 GB. In the MSP group there is a computer cluster NEMO, which is able to run up to 15 reconstructions simultaneously. It could run more reconstructions at the same time, but this would block other users in the group from using the cluster. In total 760 GB of data was generated (which took more than 300 CPUdays) during reconstruction of the measurements done for this thesis.

3.3 Bubble detection

To determine whether there are bubbles present in the reconstructed images a Matlab script will be run. In this script all reconstructed slices are stacked on top of each other and are converted into a binary image. A value of 1 represents a bubble, and 0 represents particles. The choice whether a pixel should be 1 or 0 is determined by a threshold. After this threshold has been applied, morphological opening is performed on the stack of images. The morphological open operation is an erosion followed by a dilation. This removes a lot of noise and makes it possible to use lower threshold values. The opening command can be given extra input which determines the way it processes the image. This is a balance between removing as much noise as possible and keeping fine details and small bubble visible. The effect of the opening operation on a thresholded reconstructed image is shown in figure 3.9. If the reconstructions are stacked on top of each other a semi-3D image of the bed is obtained, see figure 3.10. The vertical axis is actually time, each unit is a time step of 4 ms.

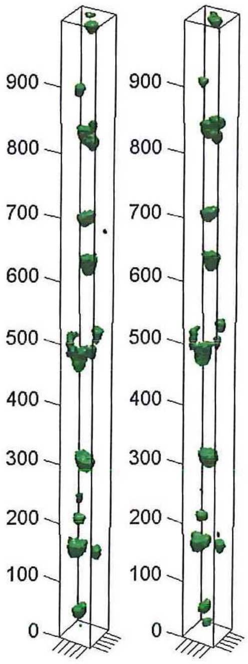

Figure 3.10: Semi-3D image made from stacked reconstruction after processing. Height is actually time. Left: lower plane, right: upper plane.

3.3.1 Threshold choice

The value of the threshold used to determine the transition from particles to bubble has a large influence on the smallest bubbles that will be detected and the volume of the bubbles detected. To determine the correct value to use for this threshold a thin-walled perspex phantom is inserted in the bed. The reconstructed images will show a bubble with a diameter of the inner diameter of the phantom. A 52 mm and a 22 mm inner diameter phantom where used to find the appropriate

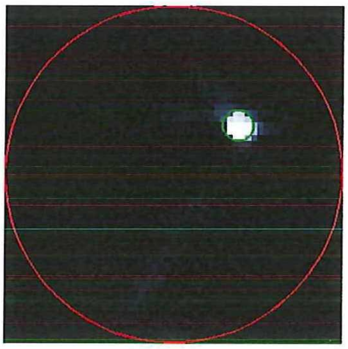

Figure 3.11: A reconstructed 22mm inner diameter phantom. Green shows the inner phantom diameter.

threshold value.
This way of experimentally determining the correct threshold value was chosen over more convention threshold determination methods. A more commonly used way to determine a threshold is using the average pixel value of an image as the threshold. This can be done iteratively to separate the foreground from the background. Also methods base on histograms of pixel value, like the Otsu method (see Shapiro and C. (2001)), could be used to find the correct value. However, this assumes that there is always something in the image that should be extracted from the background. In our case, there is not always a bubble present, so using these methods on each image will result in noise being identified as a bubble. Using a fixed threshold value produces adequate results and is faster.

3.4 Speed measuring

Because the distance between the two measurement planes is known, the bubble rise velocity can be calculated from the measurement data. This can be done using the raw data from the detectors or using the reconstructions. Because the temporal resolution of the raw data is 10 times higher (2500 Hz versus 250 Hz) this will provide the most accurate information. Analyzing the raw data by hand is possible for a few single bubbles, but for more than this, it becomes very cumbersome. If there are multiple bubbles present at one time in the plane, using the raw data can also be difficult. Using the reconstructed images becomes much more interesting since it is easy to let a computer find the bubble speeds. To do this, the computer will need to match bubbles detected in the lower and upper plane.
To verify the accuracy of the data retrieved in this way, a perspex cylinder of known dimensions is pulled through the bed at a known speed. The results from the setup should of course be the true dimensions and true speed. The speed is controlled by a vertical traverse that is monitored using a high speed camera.

3.4.1 Bubble matching

In both the lower and upper plane bubbles are detected. Because these planes are only 1.86 cm apart, it can be assumed that the bubbles don't change much in that short distance. If a bubble of similar size, at a similar location in the bed and with not too much time between them, is detected in both planes, it can be assumed that this is the same bubble. The bubble detection script will give an overview of the bubbles that have been detected in both planes in two data files. For each bubble the most important data is recorded. These files can be used to match the bubbles. As stated before, the bubbles are matched on four criteria:

- The position of the center of gravity of the bubble in the measurement plane
- The maximum diameter of the bubble in the plane
- The time at which the center of gravity of the bubble passed the plane
- The detected volume in 'pixel^2 $\cdot$ sample time'

Of course the same bubble traveling from the lower to the upper measurement plane might have slightly changed in shape, position or size. Also there might be noise in the reconstructed image. However, it still is the same bubble, and therefor should be matched. That is why a search area is defined for each bubble. For the position and maximum diameter this search area has the size of one standard deviation of all the bubble positions and maximum diameters detected in the current measurement series, respectively. For the volume of the bubble it is two standard deviations of all detected bubble volumes.
The result of this matching procedure can be seen in figure 3.12. Here the time is set out on the horizontal axis. This is a 60 second data set at 250 reconstructions per second. At the time at which the center of gravity passes the measurement plane, a x is put in the graph. A red one if the bubble is detected in the upper plane and a blue one if it is detected in the lower plane. On the vertical axis the bubble size in pixel^2 $\cdot$ sample time is set out. If a lower plane bubble can be matched to an upper plane bubble, a

green line is drawn between their markers in the plot. In an ideal case the red and blue markers should be at the same height, because they should have the same size in $\text{pixel}^2 \cdot$ sample time. Differences in size could be caused by the actual changing of the volume of the bubble, but also by speed difference. But over the relatively small distance between the planes these factors will probably not play a very significant role. Although very often the bubble detected in the upper plane is larger. But this is also the case if an artificial bubble is used, which has the same volume all the time. Noise and calibration errors are the largest contributions to the differences in size.

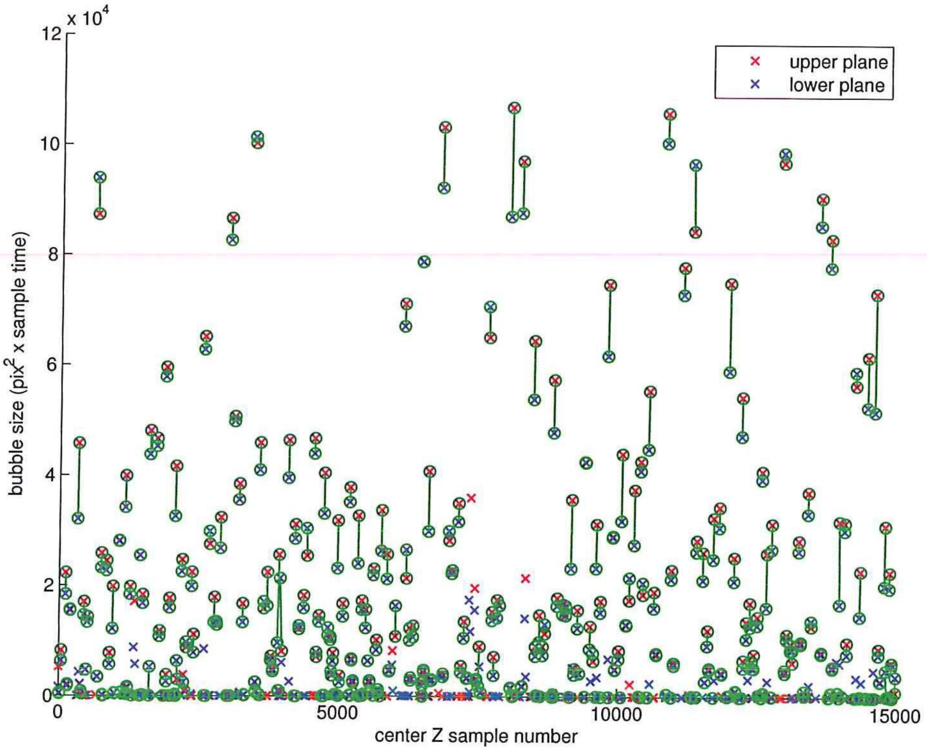

Figure 3.12: Matches made in 60 seconds of data, blue shows data from the lower plane, red from the upper plane. 607 μm polystyrene particles fluidized using the distribution plate at 1 bar_{abs} with a gas velocity of 0.32 m/s, studied at a height of 279 mm above the plate. 63% of the detected bubbles could be matched.

The time that is allowed to be between the center of the bubble passing the planes, sets the lower speed limit that can be detected. If speeds above about 1 m/s are detected, it should be noted that the discretization of the time starts to play a large role. If a speed of 0.93 m/s is detected, this is an interval of 5 frames. If an interval of 4 frames is detected this immediately leads to a detected speed of 1.16 m/s, a 25% increase. At higher speeds it gets even worse. At lower speeds (0.5 m/s) this step is about 10%. This generates discretization errors. Instead of using the time at which the bubble first passed the plane, the time at which the center of gravity of the bubble passed the plane is used. These values are less affected by the discretization errors because they are based on the entire bubble volume and do not have to be integer values. If the bubble edge is studied, a difference of one pixel can have a very large influence. Whereas a difference of one pixel will only slightly change the position of the center of gravity. This will give a more reliable result.

Instead of using 10 samples from the detectors for one reconstruction, less samples could be used. This will increase the time resolution, and reduce the discretization problems when detecting bubble speed. It will also increase the noise levels in the reconstruction. This will make the data obtained using these reconstructions less reliable. The noise is caused by the fact that the photon detection process is similar to a Poisson process. The standard deviation of the measured value will be the square root of the mean. Having a higher photon count will make it's standard deviation, and thus the error and noise, relatively smaller.

Now that the bubble size in $\text{pixel}^2 \cdot$ sample time and the speed are known, a true bubble size can be calculated. The size of a matched bubble is found by averaging the size detected in both planes. This size in $\text{pixel}^2 \cdot$ sample time is converted to $m^2{\cdot}s$ using the column diameter and sample time. If this is multiplied by the detected speed in m/s, the true volume is found in m^3.
This makes it possible to obtain a spherical equivalent diameter of each bubble, which can be compared to literature. A histogram of the detected spherical equivalent bubble diameters using the method described above, can be found in figure 3.13.

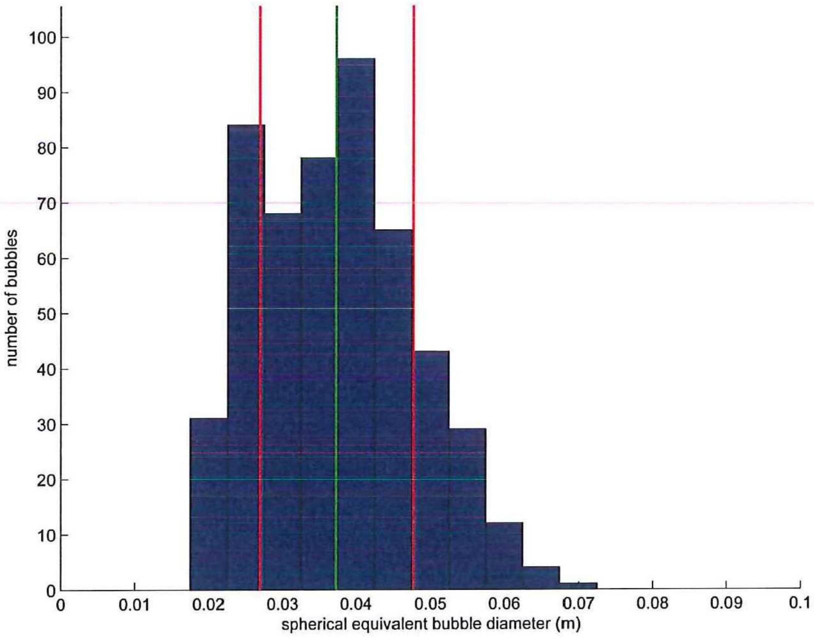

Figure 3.13: Histogram of the spherical equivalent diameter of the bubbles matched. The green line shows the mean value (3.7 cm) and the red ones are placed at one standard deviation (1.0 cm) from the mean. 607 μm polystyrene particles fluidized using the distribution plate at 3 bar_{abs} with a gas velocity of 0.14 m/s, studied at a height of 199 mm above the plate.

3.5 Particles size distribution

Particle size and bulk density determine the type of fluidization behavior and make it possible to compare the measured quantities to the theoretical values. Therefor it is important to know these two values. The density is easy to determine using a weighing scale and a measuring cup. The size of the particles is more difficult. However the Beckman Coulter LS 230 laser diffraction particle size analyzer at the Proeffabriek can be used to measure the particle size distribution.
This showed that the polystyrene spheres that were sold as having a mean diameter of 560 μm, actually have a mean diameter of 607 μm, see 3.14.

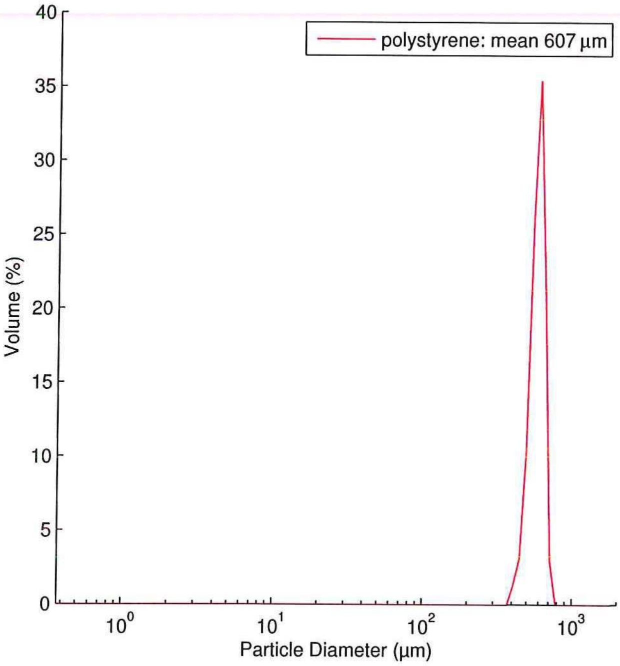

Figure 3.14: Particle size distribution for the polystyrene particles.

CHAPTER 4

Experiment results

This chapter will give an overview of the most important results obtained using the setup and methods described in the previous chapter. The effect of pressure and the effect of fines-content is studied. The pressure measurements are done using a distribution plate and a single jet as bubble source. The fines-content measurements were only done using a distribution plate.

4.1 Pressure effects

Using an elevated pressure inside the vessel will affect the behavior of the fluidized bed in it. Literature shows that fluidization will occur at a lower superficial gas velocity (e.g. Olowson and Almstedt (1991)) and overall bubble size will be smaller (e.g. Weimer and Quarderer (1985)).

The pressure effect study will be done using polystyrene particles with a bulk density of 625 kg/m^3. The bed inside the stainless steel column has a diameter of 25 cm and a height of about 55 cm. For the first measurement series the bed was fluidized using a distribution plate at the bottom of the column. For the second measurement this plate was used to bring the bed just below the minimum bubbling velocity, and use a single jet mounted above the plate to produce bubbles.

The average diameter of the polystyrene particles was determined to be 607 μm. There is little spread in the particles diameters (see figure 3.14). This is a Geldart B powder.

Minimum fluidization velocity

The moment at which the bed stops expanding and becomes fluidized is easy to determine if the vessel is not sealed and the bed can be seen and disturbed by hand. If the bed is not fluidized, disturbances in the bed surface caused by moving bed material will not disappear quickly. If the bed is fluidized, disturbances will immediately disappear; it's not possible to makes 'dunes' of bed material.
If the gas velocity is increased to the minimum fluidization value, a higher value for u_{mf} will be found than if the bed is already fluidized and the gas velocity is lowered unto the bed no longer is fluidized. For 607 μm polystyrene particles at atmospheric pressure the flow was found to be 350 l/min, which corresponds to a superficial gas velocity of 0.12 m/s.
Studying the precise moment at which the minimum fluidization velocity, u_{mf}, is reached, is difficult using X-rays. Studying the moment at which bubbles start showing up, u_{mb}, however, is quite simple. Bubbles above a certain size will show up as district temporary increases in detector signal. Studied relatively high up in the bed will make sure that if there are bubbles, they will be bigger and therefor easier to notice in the detector signal. Using the X-ray setup the results obtained are shown in figure 4.1, for both the superficial gas velocity and the normal volume flow. For the pressurized measurements these normal volume flows are the volumes that the flows would have under atmospheric conditions (so it is actually a mass flow).

For Geldart B powders the minimum bubbling velocity should be nearly equal to the minimum fluidization velocity. Working with the polystyrene spheres under atmospheric conditions a minimum fluidization velocity of 0.12 m/s is found, but no bubbles are seen in the X-ray detector signals until a gas velocity of 0.17 m/s (500 l/min). If the bed is studied by looking at it, only very small bubbles appear once in a while at velocities below this 0.17 m/s. So this velocity gives the velocity at which the

entire bed starts bubbling.
This could be explained by the fact that the polystyrene particles do fall into the Geldart B category, but are not too far from the line that separates them from the Geldart A particles. Before the bed becomes fluidized, the bed is seen to expand slightly. This is an indication that the powder is an A powder, although it's bulk density and particle size clearly place it in the B category.

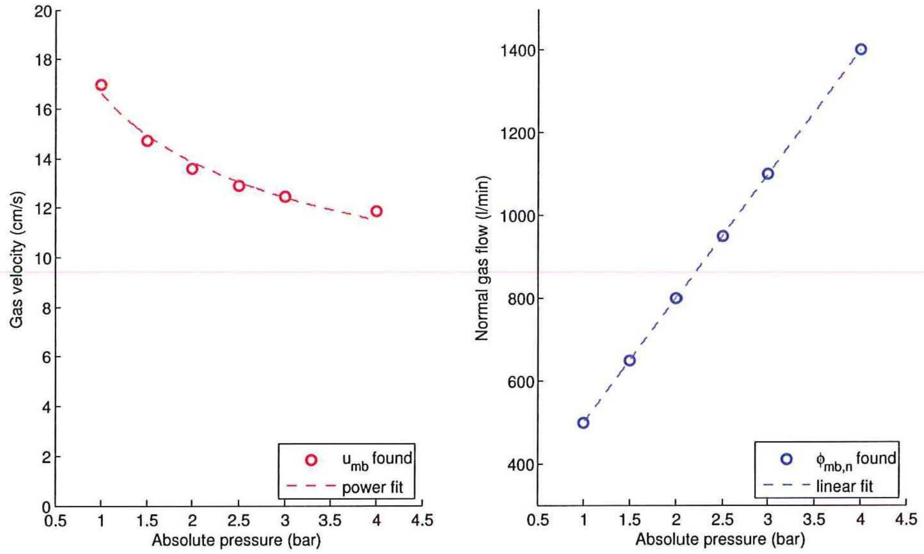

Figure 4.1: Graph of minimum bubbling velocity u_{mb} and minimum normal volume flow $\phi_{mb,n}$ for different pressures, 670 μm polystyrene.

The lowering of u_{mb} can be explained by the fact that the gas density will increase with increasing pressure. Equation 2.4 shows that if the density increases, the u_{mf} will decrease. The results are similar to what is reported in literature (e.g. Olowson and Almstedt (1991) or Kawabata et al. (1981)). These results show the regions which are worth studying. The pressurized measurements were done at the flow that corresponds to the minimum bubbling velocity, one below this velocity and three above it. The following settings were used to study the effects of pressure on a bed fluidized using the distribution plate:

Heights above plate	Flow setting	Pressure (abs)
126 mm	$\phi_{mb,n}$ - 150 norm. l/min	1 bar
159 mm	$\phi_{mb,n}$	2 bar
199 mm	$\phi_{mb,n}$ + 150 norm. l/min	3 bar
279 mm	$\phi_{mb,n}$ + 300 norm. l/min	4 bar
359 mm	$\phi_{mb,n}$ + 450 norm. l/min	5 bar
439 mm		
519 mm		

For the single jet measurements the same pressures and height were used. The single jet opening is mounted 109 mm above the distribution plate, so the heights above the jet will be shifted from the distribution plate by this distance. The flow from the single jet was set in l/min, and at higher pressures this was corrected so that the same volume of gas will be passed through the jet. This means that the gas velocities for the various settings will be the same at every pressure.

Heights above jet	Jet flow setting / gas velocity at jet	Pressure (abs)
17 mm	40 l/min / 53 m/s	1 bar
50 mm	55 l/min / 72 m/s	2 bar
90 mm	70 l/min / 92 m/s	3 bar
170 mm	85 l/min / 113 m/s	4 bar
250 mm	100 l/min / 133 m/s	5 bar
330 mm		
410 mm		

At these settings a 60 second measurement was done both for the distribution plate and the single jet. But before these results are studied the setup and the scripts are tested using synthetically generated reconstructions and (moving) phantoms.

4.1.1 Synthetic data and phantoms

To determine the accuracy and sensitivity to certain variables synthetic reconstructions and phantoms were used. Because the values that should come out of the system are known, this will give an indication of the reliability of the results obtained using the setup.

Synthetic reconstructions

Some synthetic reconstructions were generated. These consist of a 55 x 55 pixel grid, with a value of 0 outside a bubble and 1 a the bubble. No noise was added to this data. To see if the bubble detection script finds the correct bubble size and the bubble matching script finds the correct speed and volume, several synthetic reconstructions were made. These were put through the scripts; the results can be found in figure 4.2.

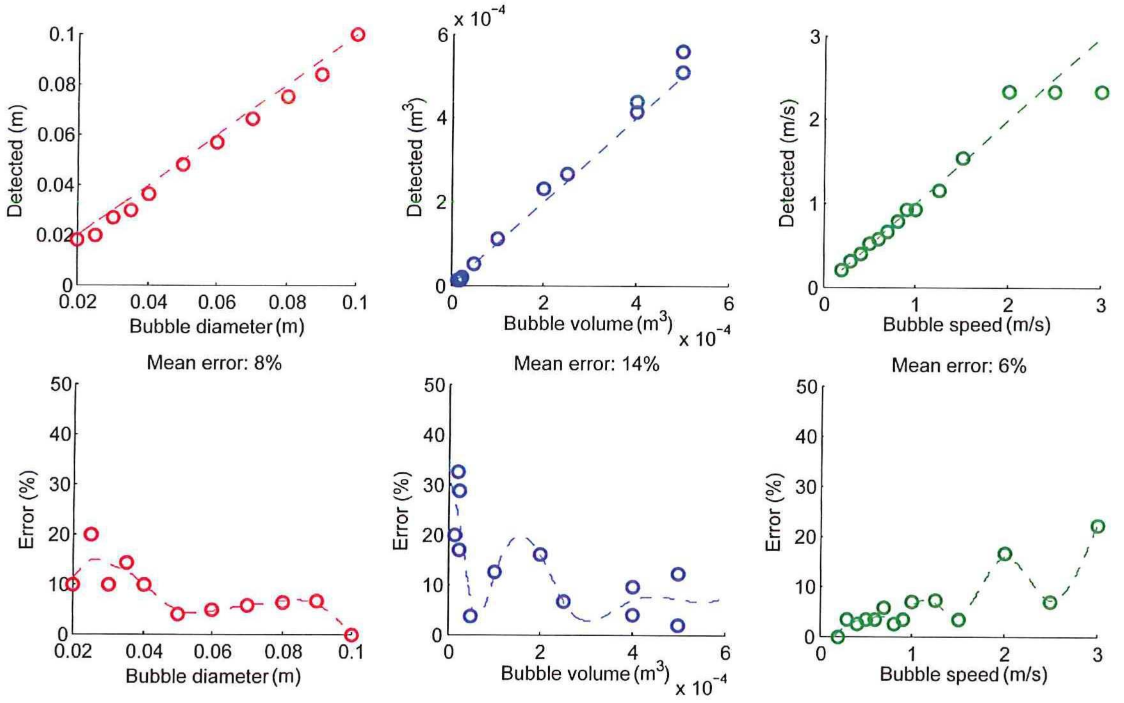

Figure 4.2: The synthetic reconstructions were processed, the output and the corresponding errors are shown, dashed lines have no physical meaning.

This clearly shows the effects of the discretization in space and time. Small bubble diameters are not detected accurately, as a consequence their volumes are also not accurate. High bubble speeds are also not detected accurately. However, if the bubble diameter is above about 4 cm and the speed stays below 1.5 m/s the results have an error of less then 10%.

Threshold determination

To determine the edge of the bubble correctly a threshold must be chosen. In the reconstructions a value of 0 represents particles and a value of 1 represents gas. At the bubble edge there is a gradient in the reconstruction. If a phantom with known inner diameter and a very thin perspex wall is inserted in the bed, the measurements can be reconstructed and a threshold can be chosen so that the correct surface area is found. This proves to be a sensitive parameter. For a 52 mm inner diameter phantom a threshold value can be determined quite easily, see figure 4.3. This is done using 607 μm polystyrene particles and the steel vessel. A value of 0.17 seems to be the correct value. If the threshold is changed by 10%, the detected surface will change by roughly 3%.
Choosing a lower threshold value would make the detection of smaller bubbles more reliable, but it will also result in more noise being identified as a bubble. Especially in the steel vessel there is a significant amount of scatter, which will show up as noise. A phantom with an inner diameter of 22 mm was difficult to detect reliably, especially if the 52 mm phantom was present as well. This shows that bubbles with a diameter of less than 2.5 cm are difficult to detect.

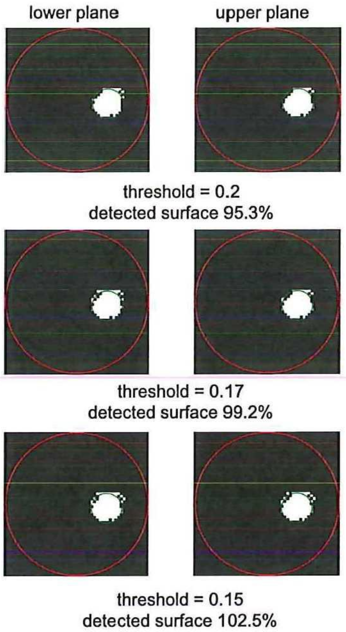

Figure 4.3: Influence of threshold choice on detected surface of 52 mm inner diameter phantom. Green shows the inner phantom diameter, red shows vessel inner wall.

Phantom speed

To verify the entire process an artificial bubble of known size is moved through the bed at a known speed. This artificial bubble is a thin-walled perspex cylinder with an inner diameter of 46 mm and an inner height of 75 mm, attached to a metal rod which is attached to a vertical traverse. A picture of the cylinder can be seen in figure 4.4. The volume of the air inside the cylinder is 124.6 cm^3. The uncertainty in this value will be about 3%.
This traverse is set at a speed of about 1 m/s. The exact speed is measured by using a 500 fps high speed camera and a ruler. The arm of the traverse with the artificial bubble in the bed attached to it, moved a distance of 10.0 cm in 46 frames. So the speed was found to be 1.0869 m/s. If frame count were to be off by one frame and the measurement by 0.1 cm, the value would change by 3%. This is a worst case scenario estimate of the error; a value of 0.5% (0.05 cm and half a frame error) seems more reasonable. The same speed was found when the action was repeated. Because the lights in the room must be switched off during the actual X-ray measurement, the speed of the traverse can only be studied when no real measurements are done. The X-ray detectors react to the light, which will cause noise in the measurement.
The bed of 607 μm polystyrene particles was set at minimum fluidization, which was found to be 0.12 m/s. The cylinder was pulled up through the bed and the measurements were reconstructed. This was done twice to make sure the results were consistent.

Raw data

Because there will only be one object moving near the center of the vessel, it is easy to identify the passing artificial bubble. Studying the signal from one of the detectors from the middle of the array, should make it possible to see the artificial bubble passing and determine it's speed using the signal from both the lower and upper detector. To make the signal easier to interpret it has been de-noised using a Daubechies wavelet. The results can be seen in the top figure 4.5. In all graphs the various parts

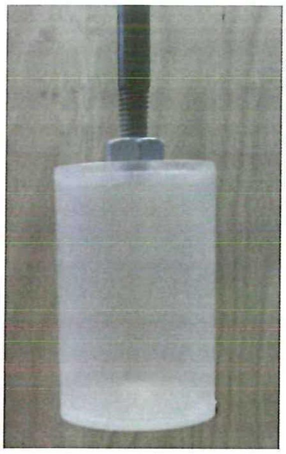

Figure 4.4: The cylinder (inner height 75 mm, inner diameter 46 mm) used as an artificial bubble, attached to a metal rod.

of the artificial bubble can clearly be distinguished, such as the metal bolt and top lid (indicated by 1) and the bottom lid (2) passing through the plane.
Although only one distinct signal was expected, there are clearly two 'things' passing the measurement planes. The second signal can be explained by the fact that the bed has to fill the void left by the artificial bubble. Since the artificial bubble is moving quite fast, it leaves a significant void behind.
For some detectors the signal before the bubble will be lower than after because the metal rod is between the detector and the X-ray tube. If detector 16 in array 1 is used, a time difference of 40 samples was found for the first measurement. Using the fact that the sample rate is 2.5 kHz and the plane distance 1.86 cm, a speed of 1.1625 m/s is found for the first measurement. Using the same method a speed of 0.9687 m/s if found for the second measurement. This gives an error of 7% and -11% respectively. The top lid of the artificial bubble gives a distinct dip in the signal, which was used to determine the speed. Taking the bottom lid will give 0.9687 m/s (-11%) and 1.1625 m/s (7%).

It is also possible to take the average of all the lower detectors and plot this. If the same is done for the upper detectors and the results are de-noised, this leads to the graph shown in the lower half of figure 4.5. The detected speeds are now 0.9687 m/s and 1.0109 m/s. The errors are -11% and -7% respectively. Taking the bottom lid will give 0.9687 m/s (-11%) and 1.1341 m/s (4%).
One would expect that taking the average of all detectors would give a smooth signal. However, a lot of noise is still present. The frequency spectrum of this averaged signal shows that lower frequencies (20 $\sim$ 40 Hz) contribute most to this signal. There is no single frequency that jumps out.
If the signal is not de-noised and the bottom lid of the cylinder is studied, speeds of 1.0814 m/s (-0.5%) and 1.0109 m/s (-7%) are found. This shows that it is possible to find very accurate speeds using the unmodified raw signal, but it is more difficult to obtain consistent results because the signal is not so clearly distinguishable from the noise.

It can be concluded that using the raw data it is possible to find the speed with an error of about 10%. However, it will only work if there is only one bubble present at a time in the measurement planes.

Reconstructed data

If the data is used to make reconstructions, there are also two distinct 'bubbles' passing the planes. If the reconstructions are processed by the bubble detection script, this shows two bubbles passing right after each other, see figure 4.6. The top bubble is the reconstruction of the cylinder. Smooth walls would be expected, but there are bulges near the top. This can be explained by the fact that the cylinder is pulled through the bed at a high speed; small air pockets will develop around the top of the cylinder.

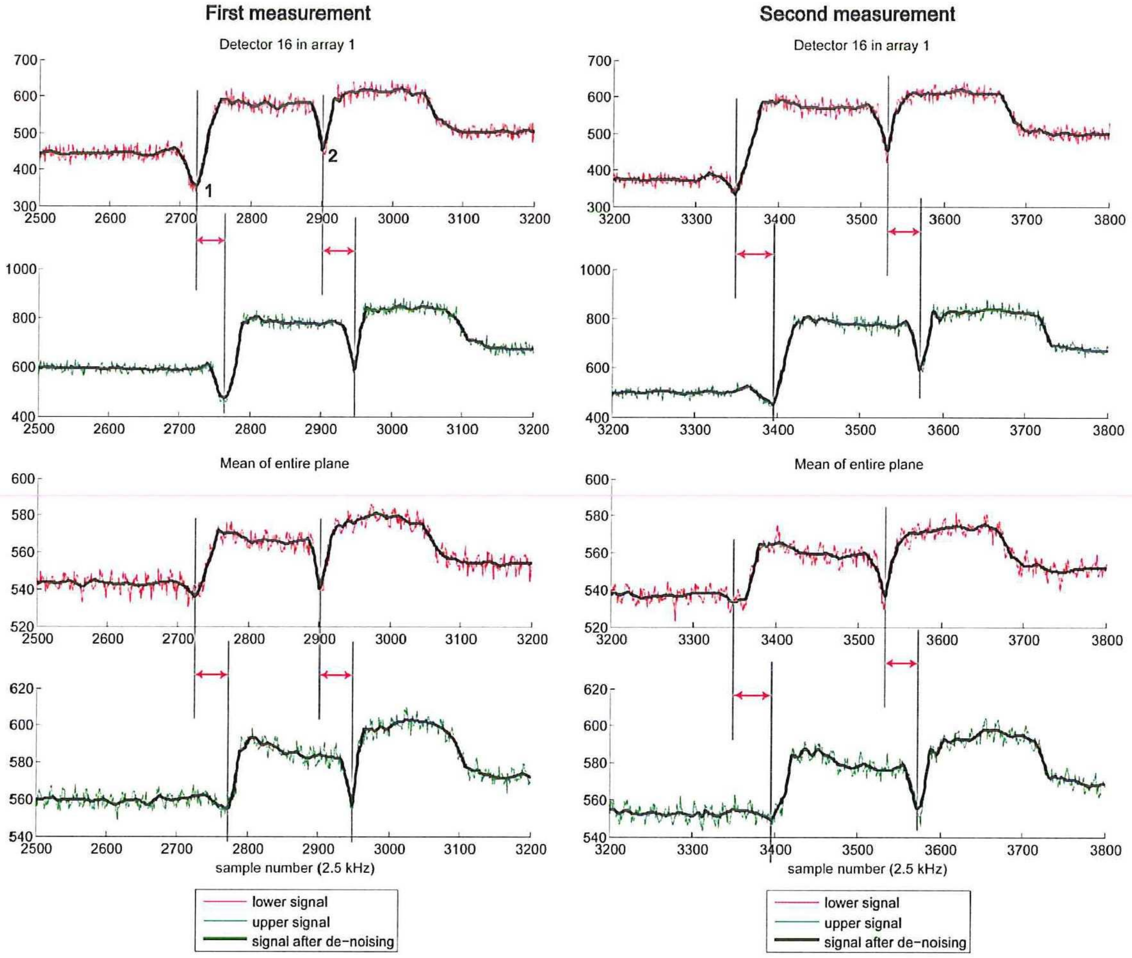

Figure 4.5: Detectors signal with artificial bubble passing through. The collapsing bed behind the bubble is clearly visible, bolt and top lid (1) and bottom lid (2) of the cylinder give a distinct signal.

Using this reconstruction, a speed and a volume can be calculated. To do this the bubbles detected in both planes must be matched. Usually there are many bubbles and the standard deviation in their various properties gives a good matching range. When there are only a few bubbles this does not work so well. Therefor the matching criteria were put in manually. Since there are only a few bubbles to be matched, this will not cause any problems.

For the first measurement the detected volume is 120 cm^3 (error -4%) and the detected speed is 1.2206 m/s (error 12%). For the second measurement we find a volume of 113.6 cm^3 (error -9%) and a speed of 1.1749 m/s (error 8%).
This shows that the data obtained using the reconstructions also has an error of about 10%.

A summary of the results from the artificial bubble measurements is shown in the table.

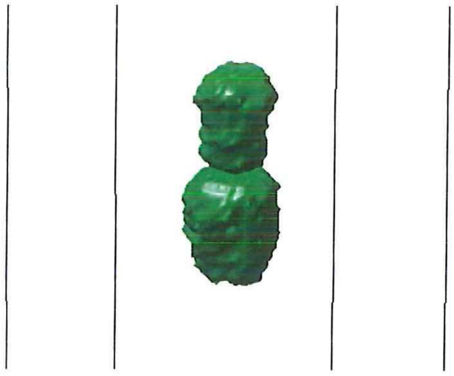

Figure 4.6: Reconstructed bubbles when phantom is pulled through bed. Top bubble is the actual phantom, bottom bubble is the bed collapsing behind the phantom.

measurement	first run	error	second run	error
actual cylinder speed	1.0869 m/s	±0.5%	1.0869 m/s	±0.5%
de-noised data (single) top lid speed	1.1625 m/s	7%	0.9687 m/s	-11%
de-noised data (mean) top lid speed	0.9687 m/s	-11%	1.0109 m/s	-7%
de-noised data (single) bottom lid speed	0.9687 m/s	-11%	1.1625 m/s	7%
de-noised data (mean) bottom lid speed	0.9687 m/s	-11%	1.1341 m/s	4%
raw data (mean) bottom lid speed	1.0814 m/s	-0.5%	1.0109 m/s	-7%
reconstructed data speed	1.2206 m/s	12%	1.1749 m/s	8%
actual cylinder volume	124.6 cm^3	±3%	124.6 cm^3	±3%
reconstructed data volume	120 cm^3	-4%	113.6 cm^3	-9%

It is important to note that the distance between the planes is determined experimentally as well and the planes are not exactly parallel, since they originate from a single source. Also the planes have a finite thickness. These are all contributions to the error as well.

4.1.2 Measurement results

After studying the artificial data and artificial bubble it is clear that the data obtained using the X-ray setup will typically have an error of 10%. Several properties of the bubble can be studied using the setup. Two frequently studied properties are the spherical equivalent diameter of the bubble and the bubble rise velocity.

4.1.3 Spherical equivalent diameter

A frequently studied parameter in literature is the spherical equivalent bubble size. This is the diameter the bubble would have had if it would have been perfectly spherical. In our measurements the volume of a bubble can be found. Using $d_e = (\frac{6V_b}{\pi})^{1/3}$ the spherical equivalent diameter of a bubble with a detected volume can be found.

During a single measurement run of 60 seconds typically more than 100 bubbles are detected and matched. There is a distribution in the bubble diameters. This means a mean value and a standard deviation can be calculated. Such a distribution for a single measurement run can be seen in figure 4.7. If the mean values for several measurement runs are plotted, trends become visible. The mean values are shown as circles. To get an idea of the spread around this mean value, the standard deviations will be plotted as asterisks.
Two measurement series have been done, one using the distribution plate as the gas supply, the second

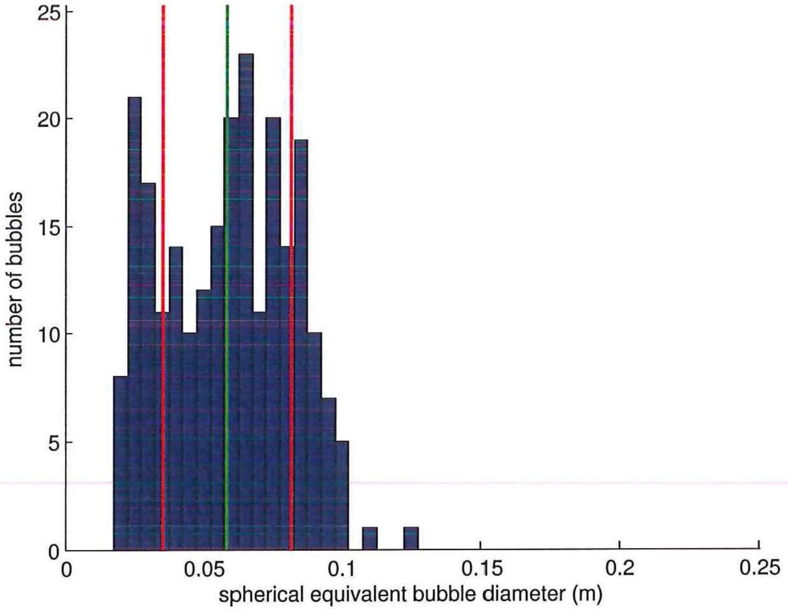

Figure 4.7: Histogram of 239 detected spherical equivalent bubble diameters for a single 60 second measurement run. During this measurement run the superficial gas velocity was 0.126 m/s, normal gas flow 1850 l/min, pressure 5 bar_{abs}, height 439 mm above distribution plate in the 25cm steel vessel. The green line shows the mean value (5.9 cm), the red lines show the standard deviations (2.3 cm)

using the distribution plate to bring the bed to minimum fluidization and then using a single jet to produce bubbles. The advantage of the single jet will be that only one bubble is present at the same time in the measurement plane. All these bubbles will also be roughly centered, because the jet in mounted in the middle. First the results from the distribution plate are studied.

4.1.4 Distribution plate

In total 175 measurement runs were done using the distribution plate. Some measurements showed no bubbles, which was not unexpected since the gas velocities were below u_{mb}.

Studied at fixed height

The effect of pressure and gas flow settings on the spherical equivalent bubble diameter can be seen in figure 4.8. This plot shows the normal gas flow and the bubble diameter for various pressures at a height of 439 mm above the distribution plate. Fits were made using Darton's relation (equation 2.10) for spherical equivalent bubble diameter, these are shown by the dashed lines. This equation has a single fitting parameter A_0, which is the catchment area. This is the area from which gas is drawn into the bubble stream. According to Darton the value of A_0 should decrease rapidly with increasing height. Above 0.2 m it should be approximately 0.

A higher vessel pressure leads to a larger catchment area for the bubbles. Studying the bed higher above the distribution plate also leads to a larger catchment area. This is unexpected; the height is already included in the Darton model, so the catchment area should not have to be increased to fit the data. Instead, it should approach zero, if a porous plate is used and the bed is studied further away from the plate.

Instead of plotting the diameter against normal gas flow, it can also be plotted against superficial gas velocity. This is the same data, but plotted in a different way. The results from studying the bed at 439 mm above the distribution plate are shown in figure 4.9. These kinds of plots can be made for all heights

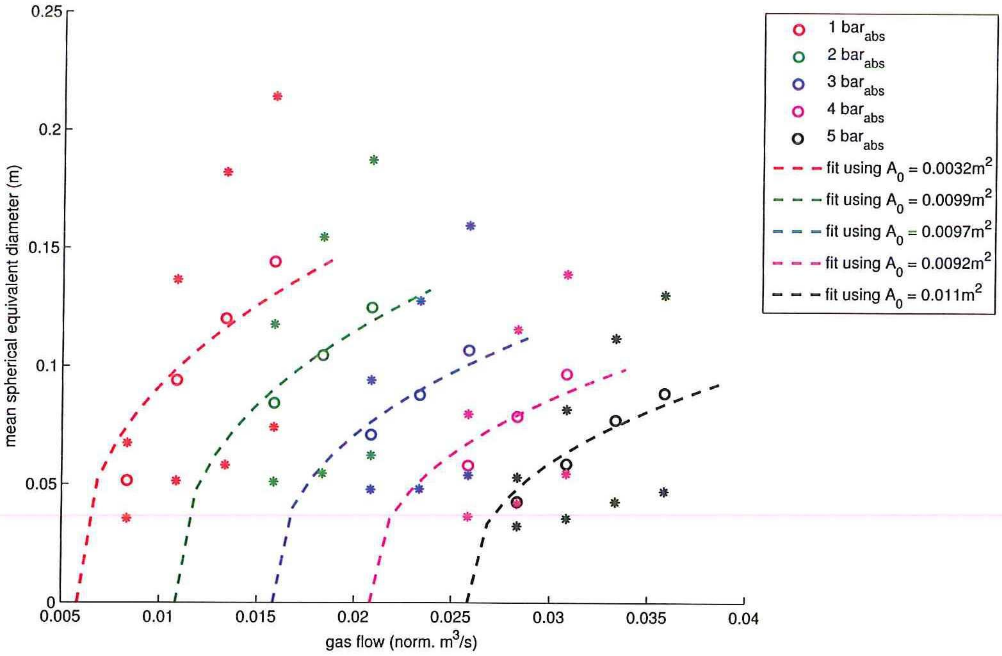

Figure 4.8: Bubble size, distribution plate, fixed height: Spherical equivalent bubble diameter for various normal gas flows at different pressures. 607 μm polystyrene in 25 cm steel vessel, 439 mm above distribution plate. Fits made using Darton's relation.

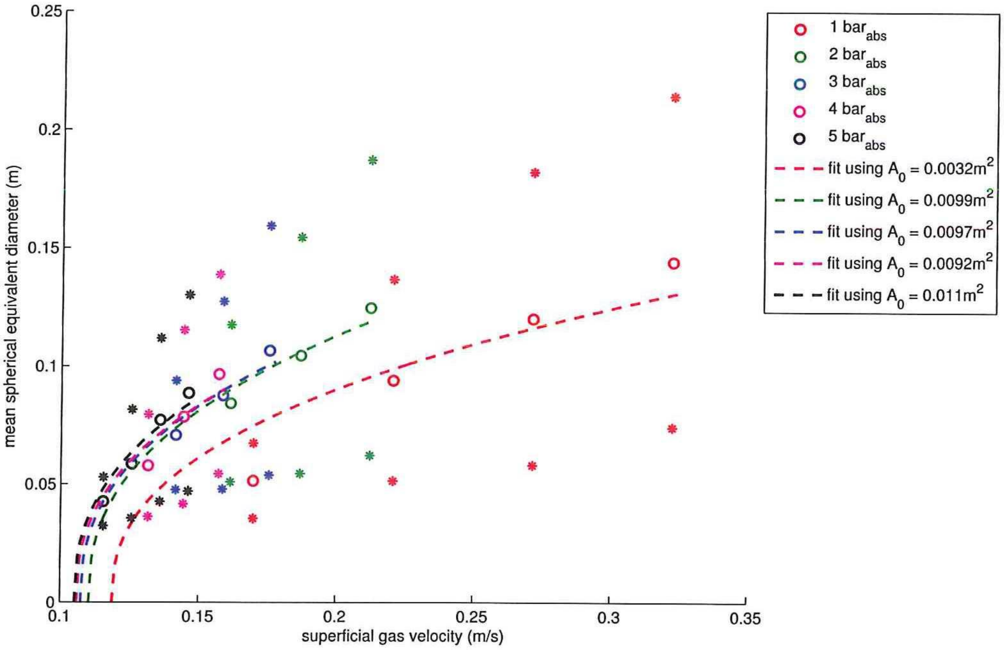

Figure 4.9: Bubble size, distribution plate, fixed height: Spherical equivalent bubble diameter for various superficial gas velocities at different pressures. 607 μm polystyrene in 25 cm steel vessel, 439 mm above distribution plate. Fits made using Darton's relation.

at which measurements were done. These can be found in appendix A1.

A plot of the catchment area A_0 versus the measurement height can be found in figure 4.10. It is clear that the catchment area must be increased to make the data fit if the height is increased. This is not what is expected. The cause of this is not very clear.
The increase in pressure also requires and increase in the catchment area to make the data fit. This is not very strange since at higher pressures more gas (weight) is required to form a bubble of a certain diameter. The Darton model does not take pressure into account directly. The lower u_{mf} does of course appear in the Darton model.

Studied at fixed pressure

The measurements were done at pressures ranging from 1 to 5 bar$_{abs}$. If these results are studied separately, results as in figure 4.11 can be found. The bubble diameter can also be plotted against the gas flow at a fixed pressure. This results in graphs such as figure 4.12. Here the catchment area increases again with the height in the bed. Plots for other pressures can be found in appendix A2.

Studied at fixed flow

All measurements are done at several flow settings, based on the u_{mb}. One below this value and 3 above it. This makes it possible to plot results for one of these flows as well, see figure 4.13. Again it is seen that a higher pressure leads to a larger catchment area. Plots for other flows can be found in appendix A3.

4.1.5 Single jet

For the single jet measurements the gas velocity was set to minimum fluidization. For higher pressures the minimum fluidization was estimated from the minimum bubble velocity. The single jet was used to create bubbles. In total 119 single jet measurements were done.
Using the available materials it was not possible to achieve the desired volume flows at 4 and 5 bar. At 4 bar only 40 and 55 l/min could be realized. At 5 bar not even 40 l/min was possible. The reason for this is that the pressure at which the air is supplied (about 7 bar) is not high enough to sustain these high flows through a relatively small diameter (~5 mm inner diameter) tube connecting to the jet.

Studied at fixed height

The results from the single jet measurements are nowhere near as good as the results from the distribution plate measurements. Far fewer bubbles were detected, which led to a much less consistent data set. One of the better results is shown in figure 4.14. This shows the spherical equivalent bubble diameter for bubble at a height of 250 mm above the jet opening. There is no clear trend, the fits based on Darton's model are shown but they show an inconsistent trend. The fitting parameter values A_0 are not shown because they won't make sense. Whereas the bubbles clearly reduced in size as the pressure increased in the distribution plate measurements, here this is effect is far less clear. Plots of different heights can be found in appendix A4.

Studied at fixed pressure

Again there is not a consistent trend to be found if the results are plotted at the various pressures. The results for 2 bar$_{abs}$ can be seen in figure 4.15. The fits using Darton's relation again do not show a consistent behavior as the flow increases. These results can also be plotted against the height above the jet opening. The results are again not very convincing, see figure 4.16. Plots of other pressures can be found in appendix A5.

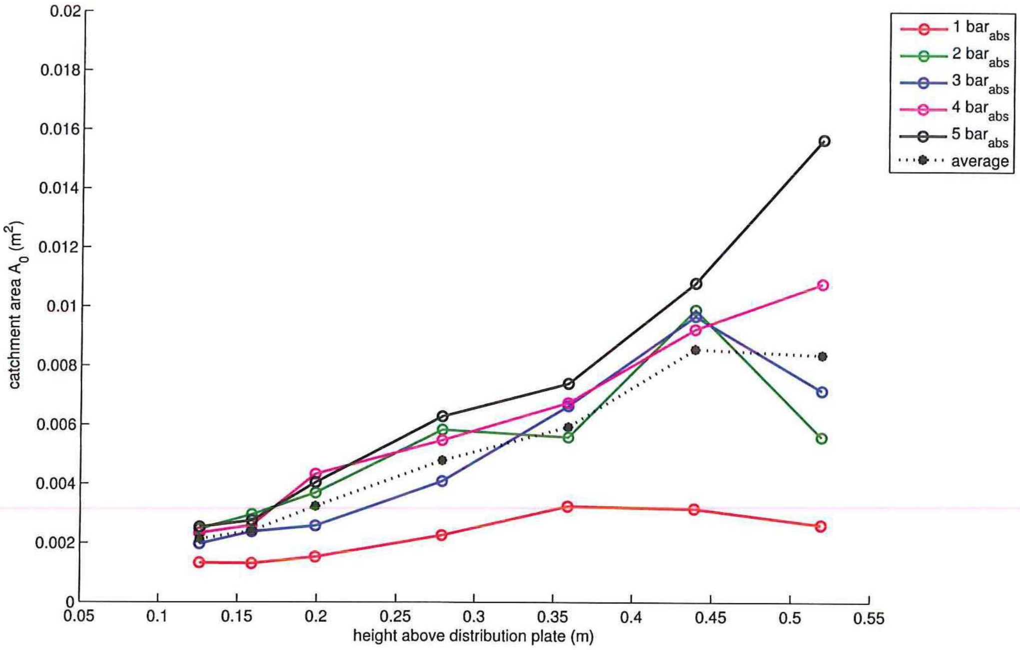

Figure 4.10: Bubble size, distribution plate, fixed pressure: Catchment area found using Darton fits for various heights at different pressures. 607 μm polystyrene in 25 cm steel vessel.

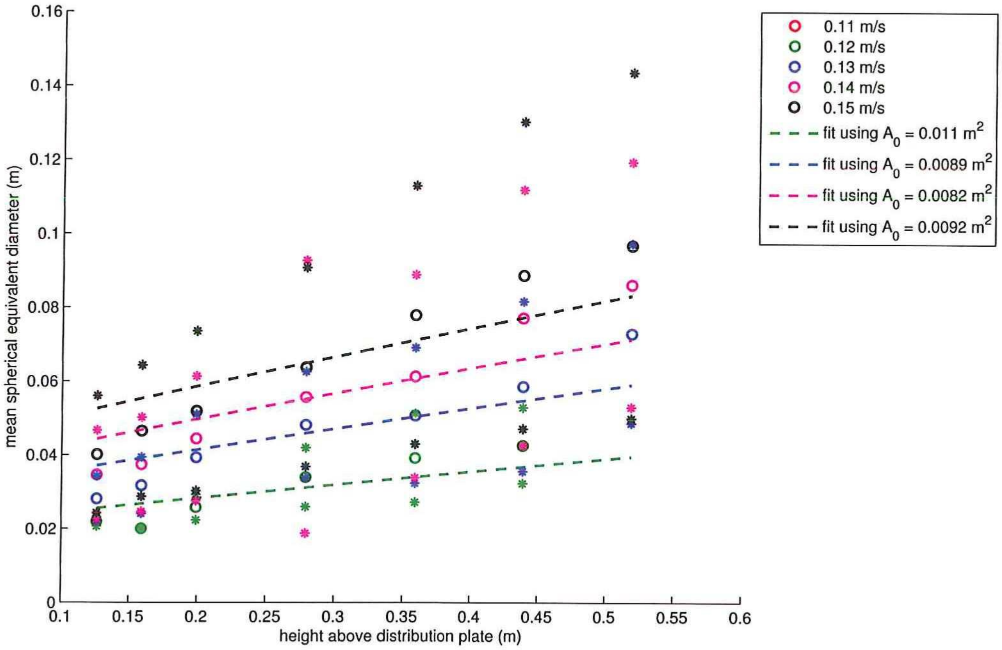

Figure 4.11: Bubble size, distribution plate, fixed pressure: Spherical equivalent bubble diameter for various superficial gas velocities at different heights. 607 μm polystyrene in 25 cm steel vessel, 5 bar_{abs} vessel pressure. Fits made using Darton's relation.

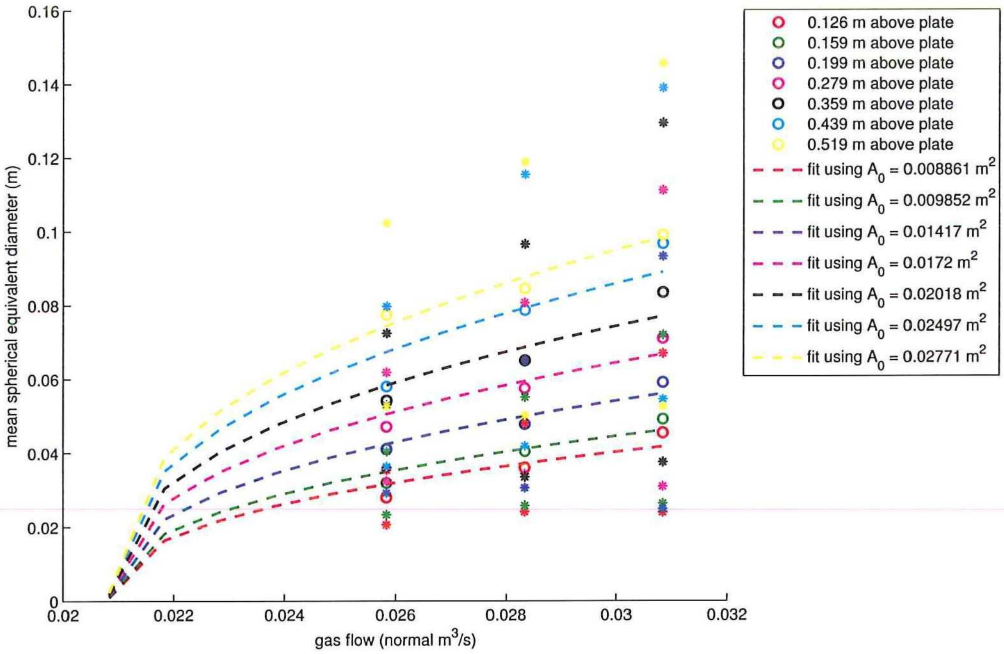

Figure 4.12: Bubble size, distribution plate, fixed pressure: Spherical equivalent bubble diameter for various normal gas flows at different heights. 607 μm polystyrene in 25 cm steel vessel, 4 bar_{abs} vessel pressure. Fits made using Darton's relation.

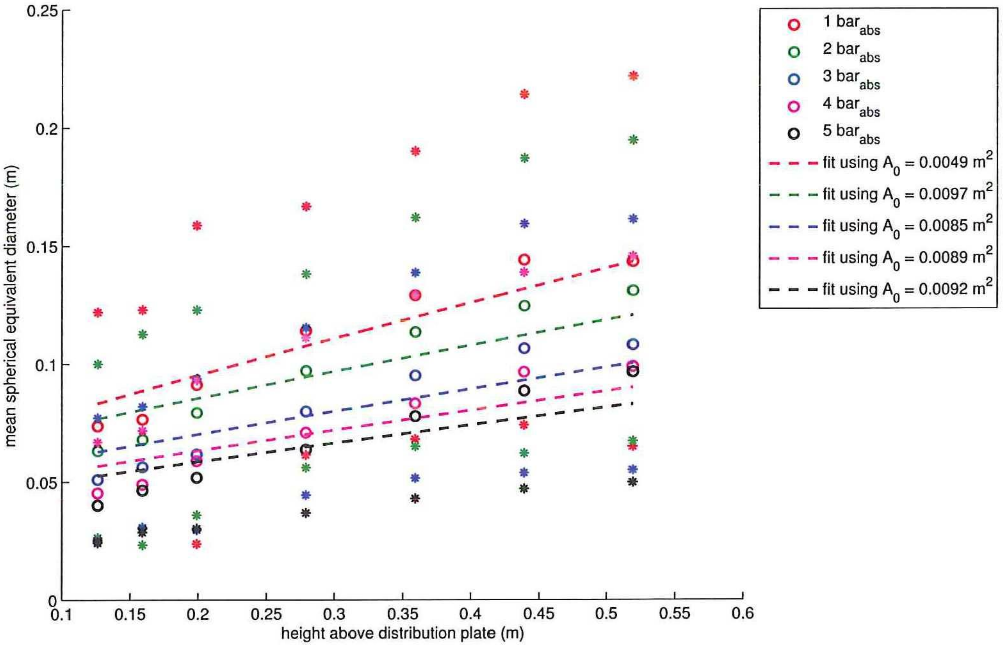

Figure 4.13: Bubble size, distribution plate, fixed flow: Spherical equivalent bubble diameter for various heights at different pressures. 607 μm polystyrene in 25 cm steel vessel, flows are $u_{mb} + 450$ normal l/min. Fits made using Darton's relation.

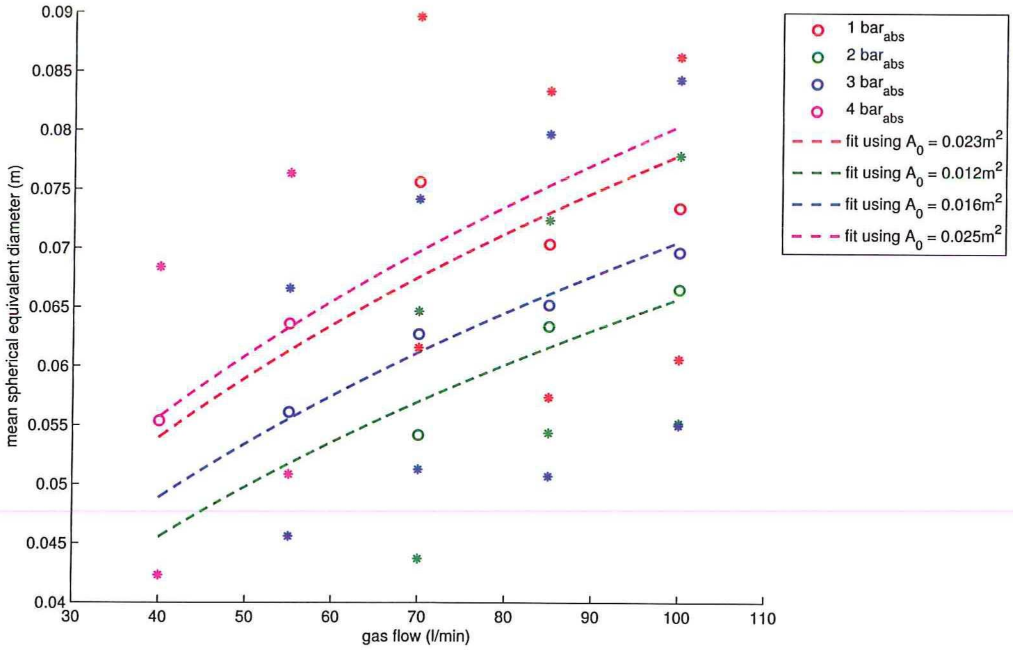

Figure 4.14: Bubble size, single jet, fixed height: Spherical equivalent bubble diameter for single jet flows at different pressures. 607 μm polystyrene in 25 cm steel vessel, at 250 mm above single jet opening. Fits made using Darton's relation.

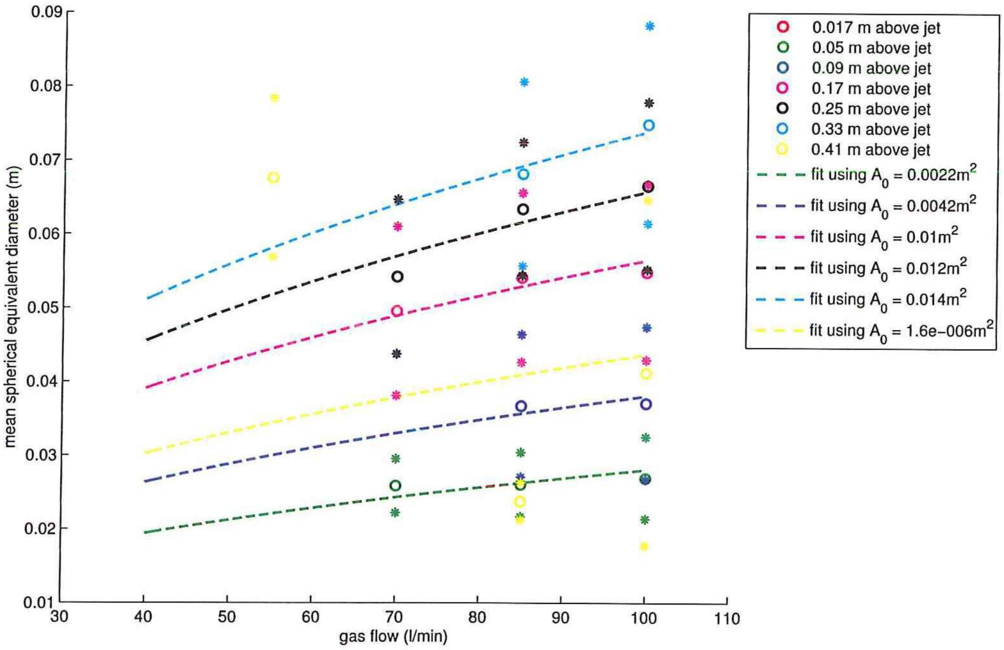

Figure 4.15: Bubble size, single jet, fixed pressure: Spherical equivalent bubble diameter for single jet flows at different heights. 607 μm polystyrene in 25 cm steel vessel, 2 bar$_{abs}$. Fits made using Darton's relation.

Studied at fixed flow

When studying the results at a fixed flow, a graph such as figure 4.17 is produced. The bubble diameter is again not very consistent. Plots of other flows can be found in appendix A6.

The results from the single jet measurements give far more erratic results than the distribution plate measurements. There are several factors that could explain why the results are not as good as the distribution plate series.
First, there are far less bubbles that are detected in a measurement run; for a distribution plate run the number of bubbles is usually more than 100 (it can be above 1000 for measurements low in the bed), whereas a single jet measurement could be based on only 20 bubbles or so.
Second, the bed was set to minimum fluidization using the distribution plate. But these flow settings were extrapolated from the minimum bubbling flows, because the X-ray setup could not accurately detect the minimum fluidization state. The chosen values therefor might not have been the correct ones. Installing pressure sensors in the wind box and the vessel might would have made it possible to determine the onset of fluidization more precisely.
Third, the bubble matching was generally much less successful for the single jet runs. Especially for measurements low in the bed at low flow settings bubble matching is difficult. For distribution plate measurements the amount of matched bubbles out of the detected bubbles can drop to around 50%, but it is usually around 70%. For the single jet measurements, however, it will drop to less than 10%. There is often a significant difference between the number of bubbles that are detected and the detected sizes in the lower and upper plane, as can be seen in figure 4.18. If the bed is studied close to the jet, the distance between the planes is significant, and bubbles will not be the same in the lower and upper plane.

Summary

The reduction in bubble size, for a given gas flow rate, that is expected when the pressure inside the vessel is raised, is observed. The spherical equivalent bubble diameters appears to be behaving the way Darton's relation describes, except for the fact that the catchment area parameter does not become smaller when studying the bed further from the distribution plate.

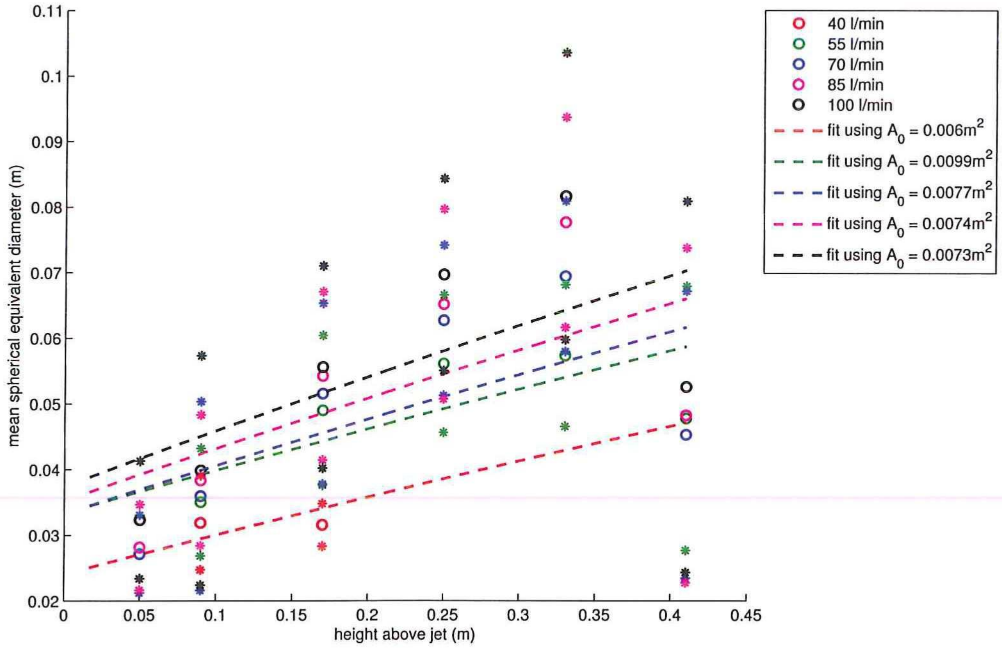

Figure 4.16: Bubble size, single jet, fixed pressure: Spherical equivalent bubble diameter for several heights at different single jet flows. 607 μm polystyrene in 25 cm steel vessel, 3 bar$_{abs}$. Fits made using Darton's relation.

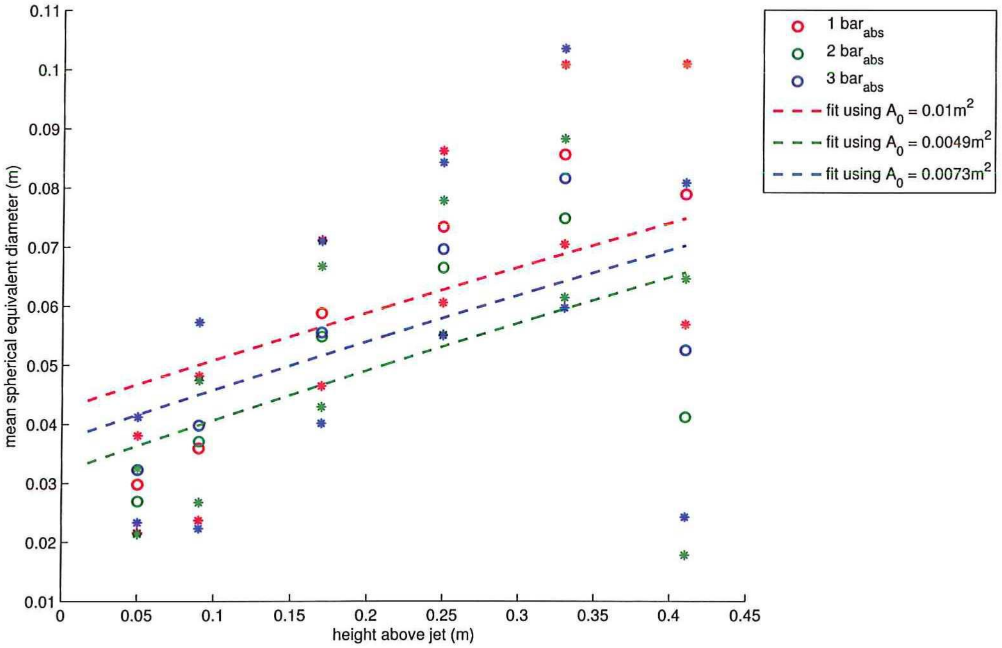

Figure 4.17: Bubble size, single jet, fixed flow: Spherical equivalent bubble diameter for several heights at different pressures. 607 μm polystyrene in 25 cm steel vessel, 100 l/min from jet. Fits made using Darton's relation.

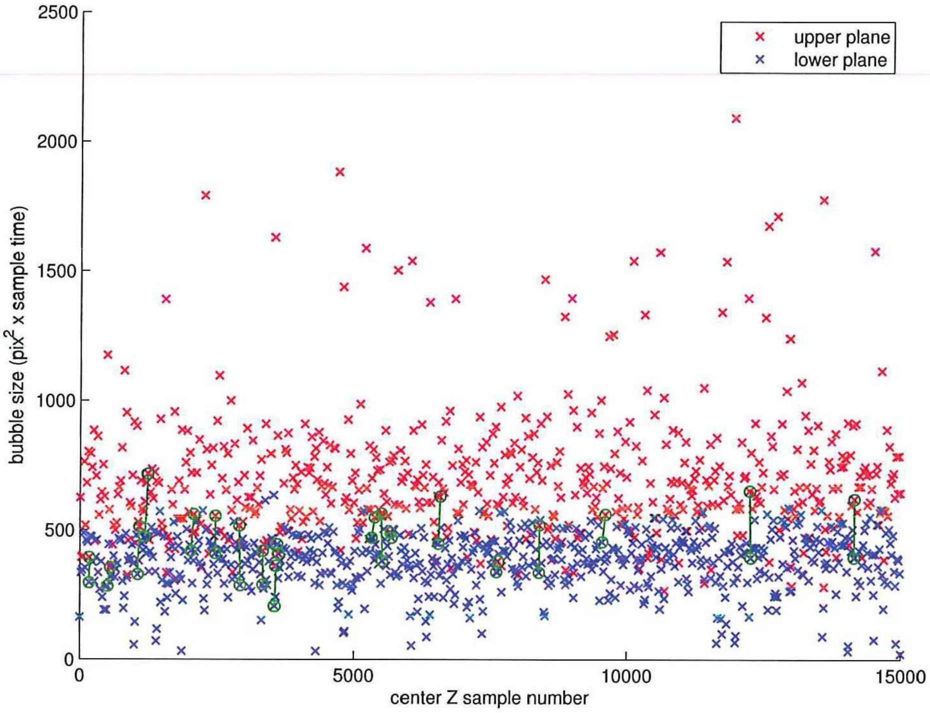

Figure 4.18: Matches made in 60 seconds of single jet data, blue shows data from the lower plane, red from the upper plane. 607 μm polystyrene particles fluidized using the single jet with a flow rate of 100 l/min at 1 bar$_{abs}$, studied at a height of 50 mm above the jet orifice. Only 3% of the detected bubbles could be matched.

4.1.6 Bubble rise velocity

Using the X-ray setup with two measurement planes the bubble rise velocity can be detected. The results of these measurements together with predictions by the model by Hilligardt and Werther (equation 2.8), are shown in the figures below. The model has two parameters, ψ and ν, that depend on the type of particles in the bed and the height of the bed compared to the bed diameter. The appropriate values were chosen for every data point.
A distribution for the detected bubble rise velocities for a single measurement run can be seen in figure 4.19.

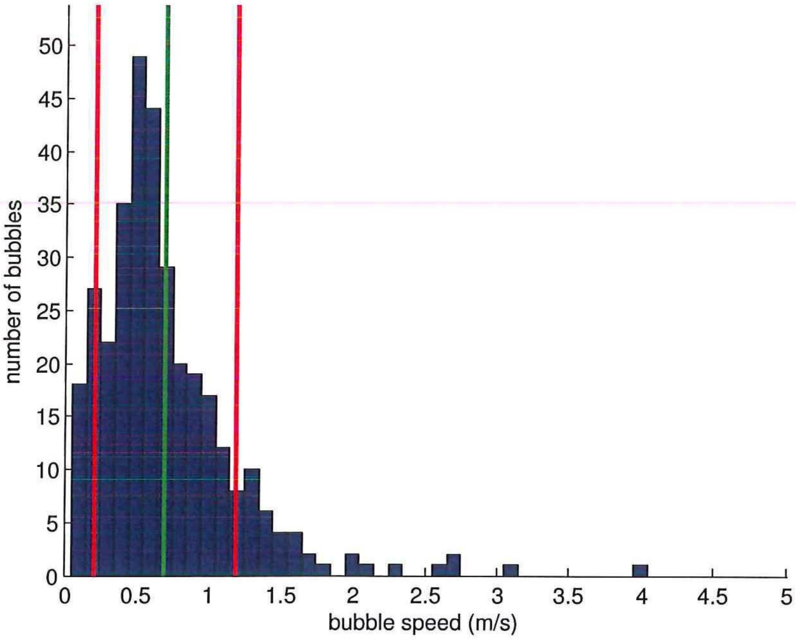

Figure 4.19: Histogram of 336 detected bubble rise velocities (absolute) for a single 60 second measurement run. During this measurement run the superficial gas velocity was 0.16 m/s, normal gas flow 1850 l/min, pressure 4 bar_{abs}, height 359 mm above distribution plate in the 25cm steel vessel. Green line shows mean value (0.70 m/s), red lines show standard deviations (0.49 m/s)

4.1.7 Distribution plate

The results from the distribution plate measurements show a clear rise in velocity higher in the bed. This is also predicted by the models, since they use the bubble size. A larger bubble size will lead to a faster bubble. The bubble rise velocities shown are the velocity a bubble on top of the superficial gas velocity ($u_{br} = u_{bubble\_absolute} - u_{gas}$).

Studied at fixed height

Depending on the height at which the bed is studied and the type of particles, different parameters should be chosen for the Hilligardt and Werther model (equation 2.8). The model uses the spherical equivalent diameter as an input. The measured diameters were used for these plots. If the measurements are studied at fixed heights the results can be plotted for the normal gas flow (figure 4.20) and superficial gas velocity (figure 4.21).
The model seems to slightly over-predicted the speeds, apart from that it matches the data fairly well. Plots for different heights can be found in appendix B1.

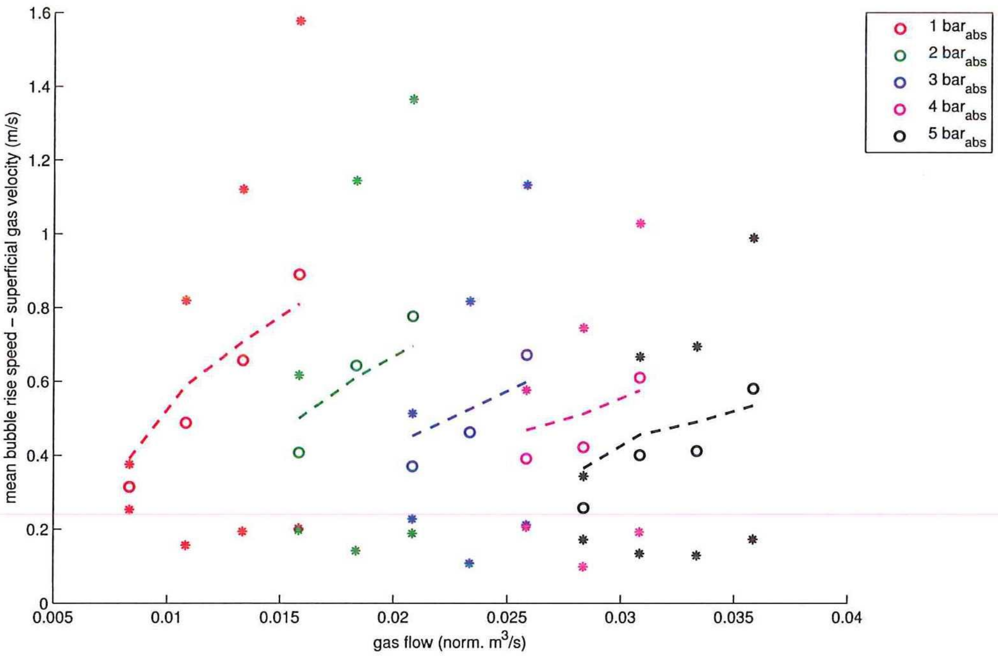

Figure 4.20: Bubble velocity, distribution plate, fixed height: Bubble rise velocity on top of gas velocity for various normal gas flows at different pressures. 607 μm polystyrene in 25 cm steel vessel, 199 mm above distribution plate. Dashed lines are made using Hilligardt and Werther model and detected bubble diameters.

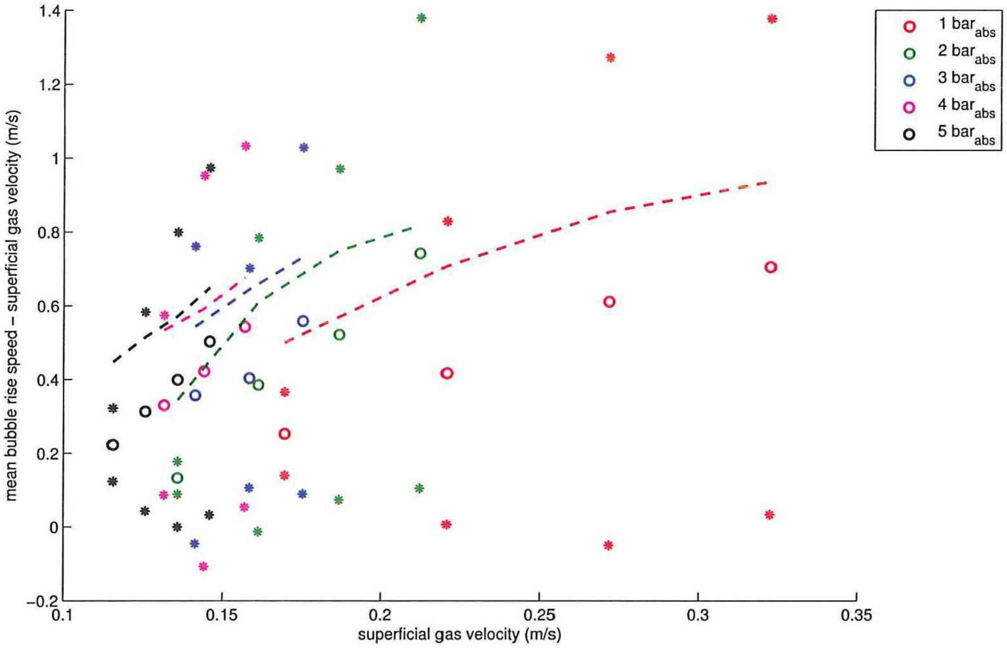

Figure 4.21: Bubble velocity, distribution plate, fixed height: Bubble rise velocity on top of gas velocity for various superficial gas velocities at different pressures. 607 μm polystyrene in 25 cm steel vessel, 359 mm above distribution plate. Dashed lines are made using Hilligardt and Werther model and detected bubble diameters.

Studied at fixed pressure

These measurements were done at pressures ranging from 1 to 5 bar$_{abs}$ as well. These can be studied separately, this results in figures like 4.22. The bubble diameter can also be plotted against the gas flow at a fixed pressure. This results in graphs such as figure 4.23. The model shows a consistent over-prediction of the bubble rise velocities. Plots for other pressures can be found in appendix B2.

Studied at fixed flow

These measurements were done at 5 different gas flow settings. If the results from one of these settings is plotted, graphs like figure 4.24 are the obtained.
Again the model consistently over-predicts the bubble rise velocities. Results for other flows can be found in appendix B3.

4.1.8 Single jet

From the single jet measurements a bubble rise velocity can also be found.

Studied at fixed height

If the measurements are studied at a fixed height in the bed, this gives results like figure 4.25.
The single jet measurements are again not as clear as the distribution plate measurements. The match between the measured data and the model is similar to the distribution plate measurements.
Using the same setup a similar series of measurements was done. The results have been published (Mudde (2011)) and show a reasonable match between the measured bubble rise velocity and size, and the model by Davidson and Harrison (1963). The Hilligardt and Werther model is a refinement of the Davidson and Harrison model, so it is expected that our match would actually be better, but it isn't.

Studied at fixed pressure

These measurements were done at different pressures so they could be studied separately, this results in figures like 4.27 when plotted against bed height and figure 4.26 when plotted against jet gas flow.
Plots for more pressures can be found in appendix B5.

Studied at fixed flow

The results from the single jet can be studied for a fixed flow as well. One of the resulting plots can be seen in figure 4.28.
Appendix B6 contains plots for the other gas flows.

Summary

Overall the detected bubble velocity seems to be lower than the values found using the model by Hilligardt and Werther. The model doesn't take pressure into account, but it uses the bubble size, so that would correct for this. It should be noted that the bubble sizes used for this model are the experimentally determined bubble sizes from the same measurements. Obviously these values are not error free, so the outcome of this model should not be treated as such either.

It is interesting to note that the measurements high in the bed show a better agreement between measured bubble velocity and calculated velocity using the detected size and the Hilligardt and Werther model. This could mean that the model is not applicable to the situation lower in the bed, even though this model is frequently used. Or the detected average bubble size lower in the bed is too small.

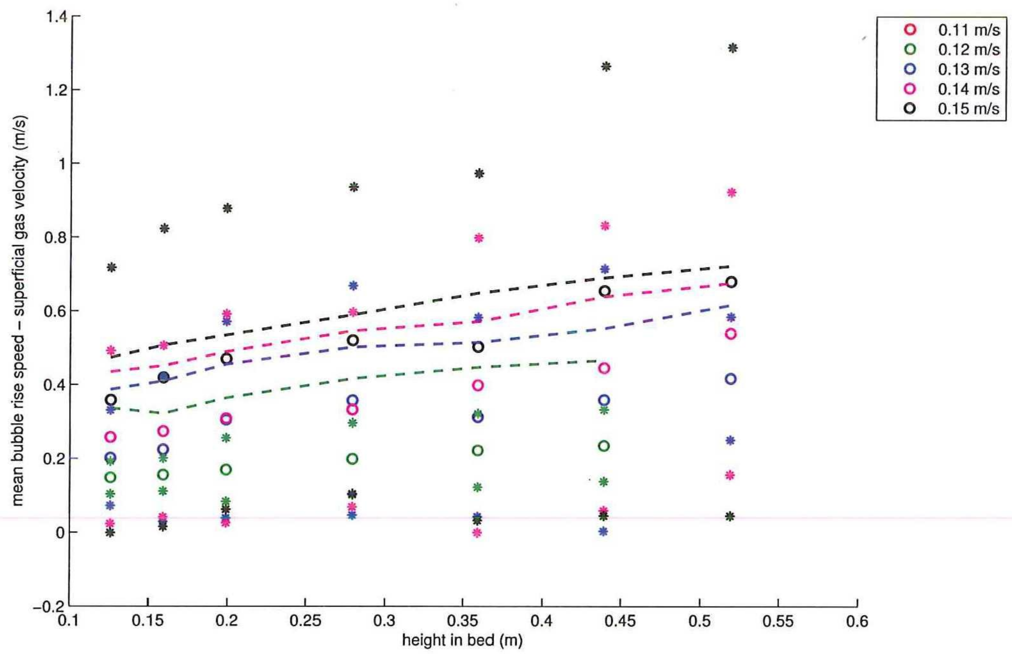

Figure 4.22: Bubble velocity, distribution plate, fixed pressure: Bubble rise velocity on top of gas velocity for various heights at different flow settings. 607 μm polystyrene in 25 cm steel vessel, 5 bar_{abs} vessel pressure. Dashed lines are made using Hilligardt and Werther model and detected bubble diameters.

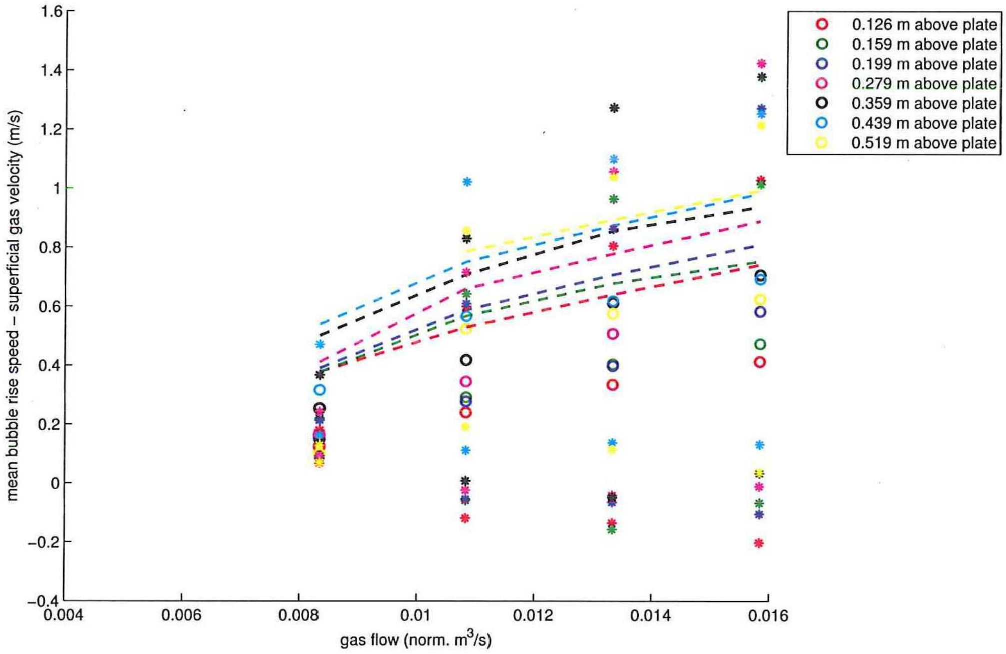

Figure 4.23: Bubble velocity, distribution plate, fixed pressure: Bubble rise velocity on top of gas velocity for various flow settings at different heights. 607 μm polystyrene in 25 cm steel vessel, 1 bar_{abs} vessel pressure. Dashed lines are made using Hilligardt and Werther model and detected bubble diameters.

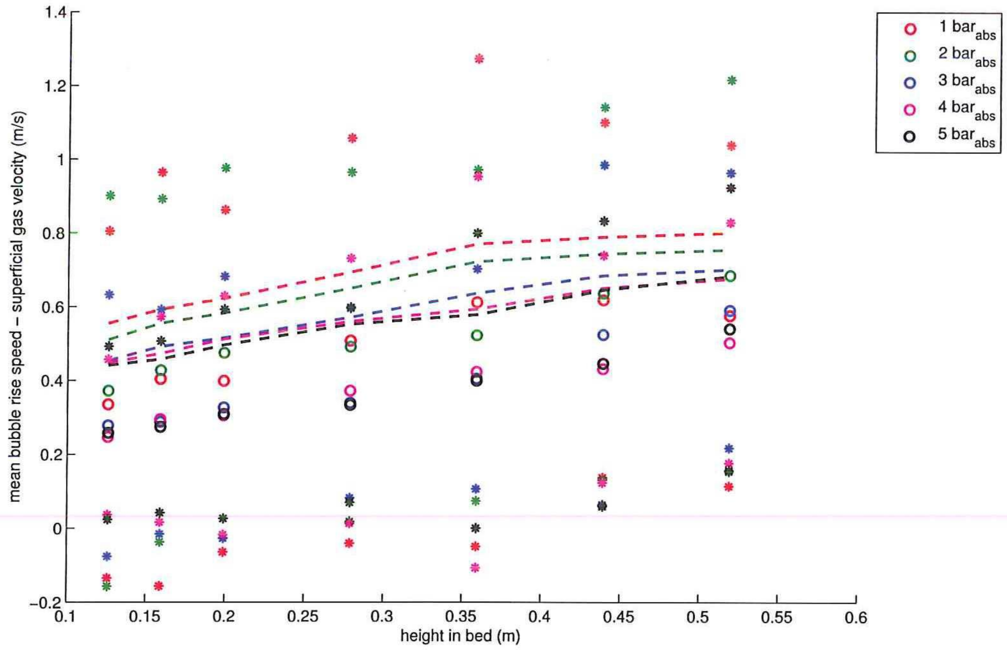

Figure 4.24: Bubble velocity, distribution plate, fixed flow: Bubble rise velocity on top of gas velocity for various flow settings at different heights. 607 μm polystyrene in 25 cm steel vessel, at flows of u_{mb} + 300 normal l/min. Dashed lines are made using Hilligardt and Werther model and detected bubble diameters.

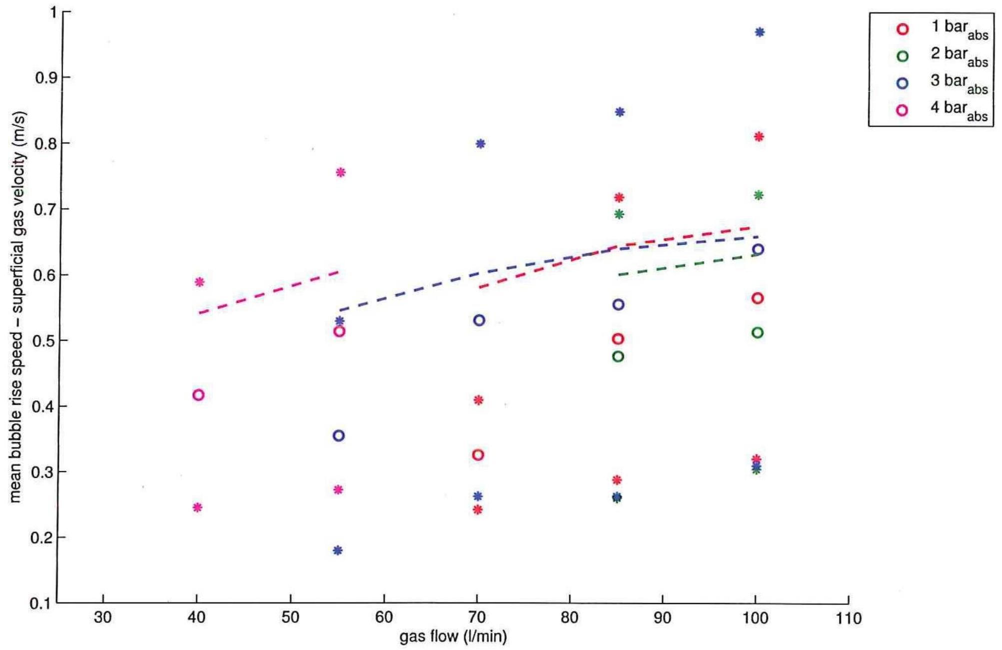

Figure 4.25: Bubble velocity, single jet, fixed height: Bubble rise velocity on top of gas velocity for various gas flows from the single jet at different pressures. 607 μm polystyrene in 25 cm steel vessel, 330 mm above jet opening. Dashed lines are made using Hilligardt and Werther model and detected bubble diameters.

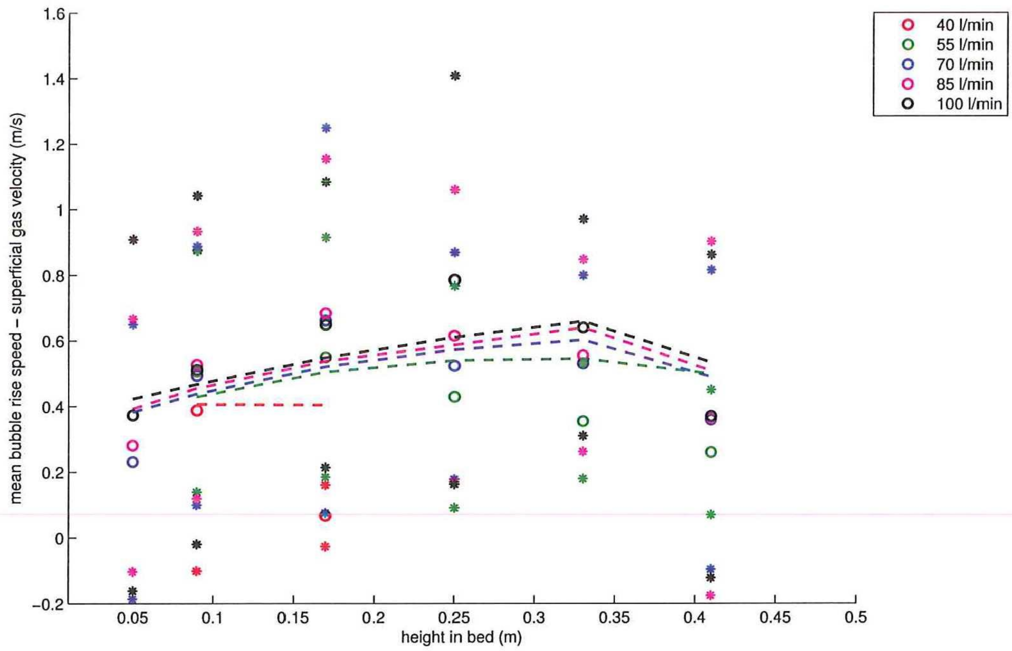

Figure 4.26: Bubble velocity, single jet, fixed pressure: Bubble rise velocity on top of gas velocity for various bed heights from different single jet flows. 607 μm polystyrene in 25 cm steel vessel, 3 bar$_{abs}$ vessel pressure. Dashed lines are made using Hilligardt and Werther model and detected bubble diameters.

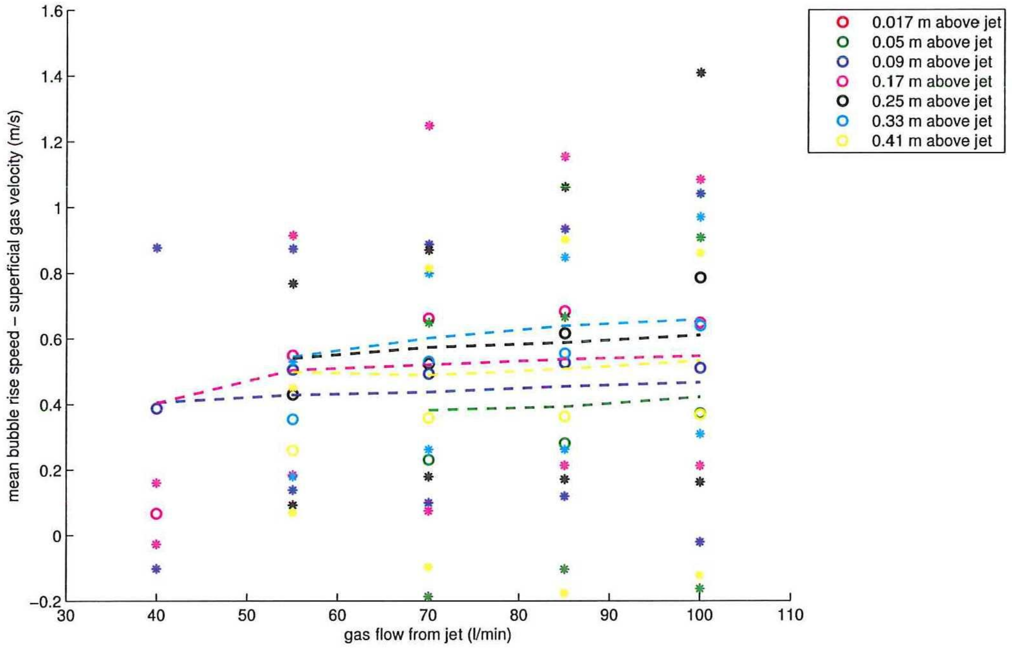

Figure 4.27: Bubble velocity, single jet, fixed pressure: Bubble rise velocity on top of gas velocity for various jet flows at different bed heights. 607 μm polystyrene in 25 cm steel vessel, 3 bar$_{abs}$ vessel pressure. Dashed lines are made using Hilligardt and Werther model and detected bubble diameters.

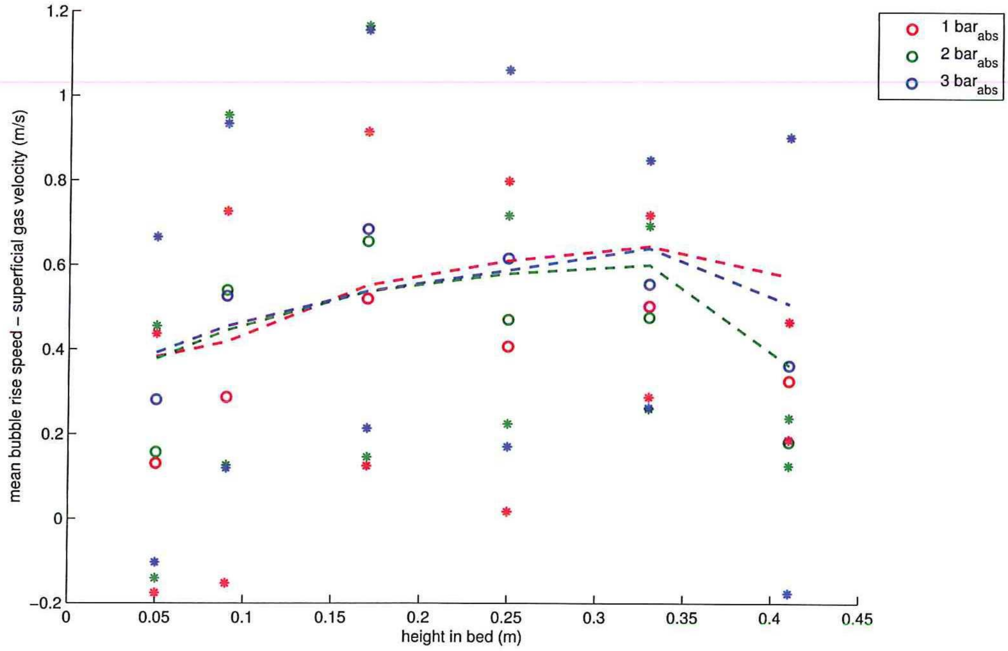

Figure 4.28: Bubble velocity, single jet, fixed flow: Bubble rise velocity on top of gas velocity for various bed heights at different pressures. 607 μm polystyrene in 25 cm steel vessel, 85 l/min from the single jet. Dashed lines are made using Hilligardt and Werther model and detected bubble diameters.

4.1.9 Error estimation

The values for the flows are treated as if they are error free. This is of course not the case, since the mass flow controllers used are not uncertainty free. If the mass flow controllers are connected in series, their measurements can be compared. The Bronkhorst mass flow controller proved unreliable at flows below 300 l/min, so it was not used for these flow rates. At values above this, it showed a difference of about 5% compared to the big Brooks controller. The Brooks always showed a slightly higher value. This Bronkhorst controller is quite new, so it's calibration is probably still quite accurate.
The small (100 l/min) and large (1200 l/min) Brooks controllers that were used for the single jet (and later on for fines measurements) showed a difference of about 20%. The large Brooks controller always gave a value slightly higher, but this was at the very bottom of it's range, so it is not too strange that the results are not very accurate.

It is interesting to see how much of the gas volume is recovered during the measurements. The amount of gas that is pumped through the vessel in one measurement run is known (gas flow rate x measurement time = $V_{tot.meas}$) and the amount of gas that is required to start seeing bubbles is also known, ϕ_{mb} x measurement time = V_{mb}. The volume required to start seeing bubbles is 'lost', but the rest should be recovered in the form of bubbles, $V_{bubbles} = V_{tot.meas} - V_{mb}$. The sum of the volume of all detected bubbles should be $V_{bubbles}$.
This assumes that the bubbles behave as if they are ping-pong balls; they have a gas volume inside them and transport this through the bed. This is not correct; gas is continually circulating inside the bubble and the cloud around the bubble. It will be difficult to make a distinction between the cloud of the bubble and the bulk of the bed using the measurement output. For very fast bubbles the cloud will be very thin, but for bubbles rising at speeds ranging from 0.2 to 1 m/s it will be significant. Using equation 2.9, we expect the radius of the cloud of a bubble traveling at u_{br} = 0.2 m/s to be about 75% more than the radius of the bubble. For a bubble that rises at u_{br} = 1 m/s, this will be about 10% for the type of particles that we use.
Furthermore, a bubble must be perfectly detected and correctly matched before it's volume can be calculated accurately.
A few measurement runs of 60 seconds were studied, the results are summarized in the table below.

measurement	bubbles matched	expected	detected	performance
dist_plate_199mm_abv_plate_0bar_0950lmin	60%	0.45 m^3	0.72 m^3	160%
dist_plate_279mm_abv_plate_0bar_0800lmin	66%	0.3 m^3	0.21 m^3	69%
dist_plate_359mm_abv_plate_0bar_0650lmin	66%	0.15 m^3	0.12 m^3	80%
dist_plate_439mm_abv_plate_0bar_0650lmin	70%	0.15 m^3	0.17 m^3	114%
dist_plate_519mm_abv_plate_0bar_0950lmin	66%	0.45 m^3	0.44 m^3	97%
dist_plate_359mm_abv_plate_1bar_0950lmin	74%	0.15 m^3	0.16 m^3	104%
dist_plate_359mm_abv_plate_2bar_1250lmin	71%	0.15 m^3	0.11 m^3	71%
dist_plate_359mm_abv_plate_3bar_1550lmin	74%	0.15 m^3	0.13 m^3	88%
dist_plate_359mm_abv_plate_4bar_1850lmin	74%	0.15 m^3	0.15 m^3	101%
average all measurements that contain bubbles				94%

This first impression shows that a very high percentage of the volume is retrieved. Even though not all bubbles are matched, a very high volume is recovered in the form of bubbles. However, sometimes the detected volume can be more than 300% of the expected volume, see the histogram in figure 4.29.

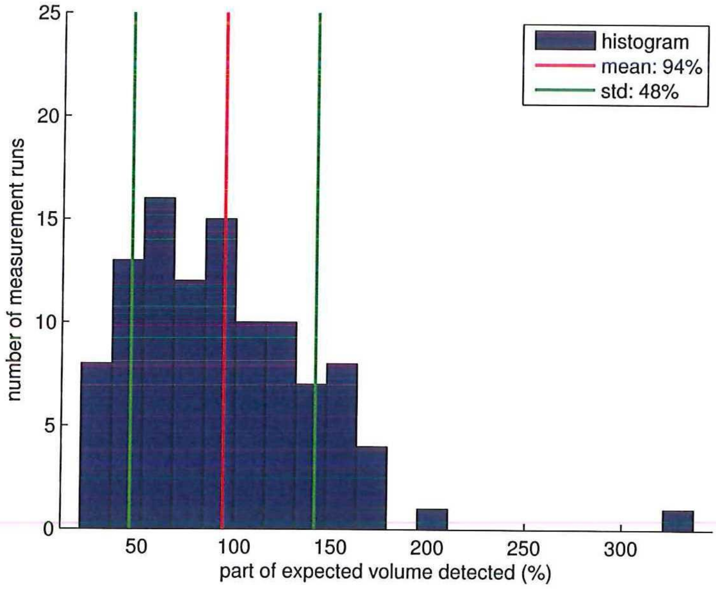

Figure 4.29: Histogram that shows the ratio between the actually detected volume of the bubbles and the expected volume based on the assumption that bubbles contain their gas (ping-pong balls). The mean is 94% with a standard deviation of 48%.

A changing pressure inside the vessel does not seem to influence the ratio between the detected and expected volumes. If the data is plotted differently, we do see a trend. This can be seen in figure 4.30. Here the ratio is plotted for various flows and heights. The different pressures are averaged into one value, since they don't seem to have much influence.

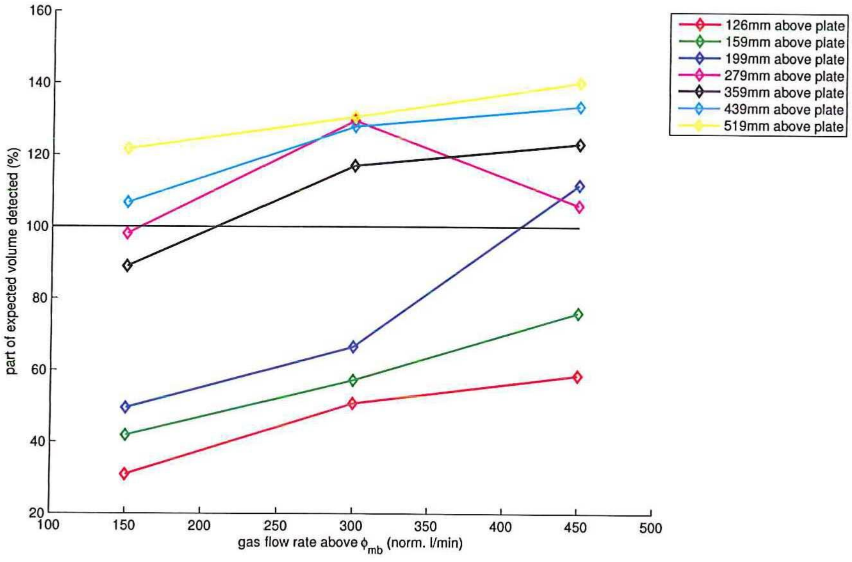

Figure 4.30: Plot that shows the ratio between the actually detected volume of the bubbles and the expected volume based on the assumption that bubbles contain their gas (ping-pong balls) for various gas flows and heights. Flows are in normal l/min above minimum bubbling flow.

Clearly the bubble volumes low in the bed and at lower gas flow rates are under detected, but the bubble volumes high in the bed and at high gas flow rates are over detected. This is interesting, because what

separates these two categories is their rise velocity.
A scatter plot can be made of the mean bubble rise velocity and the ratio of the detected and expected volume of every measurement run. This results in figure 4.31. In the plot a power fit is added using the available data. Also the ratio of the bubble to cloud and bubble volume together is plotted for the bubble rise velocities. This shows that the detection ratio is too high, even at lower bubble velocities.
The setup detects voids in the fluidized bed and determines their volume. The amount of gas that is part of a bubble is not only the gas that is in the void, but also the gas that is in the cloud. The setup will see the cloud as part of the bed, due to the threshold. The green line in figure 4.31 would suggest that the volume detection ratio would be even lower, if the setup would only detect voids. However, the threshold that was used was chosen as low as possible. So parts of the clouds were still seen as a bubble.

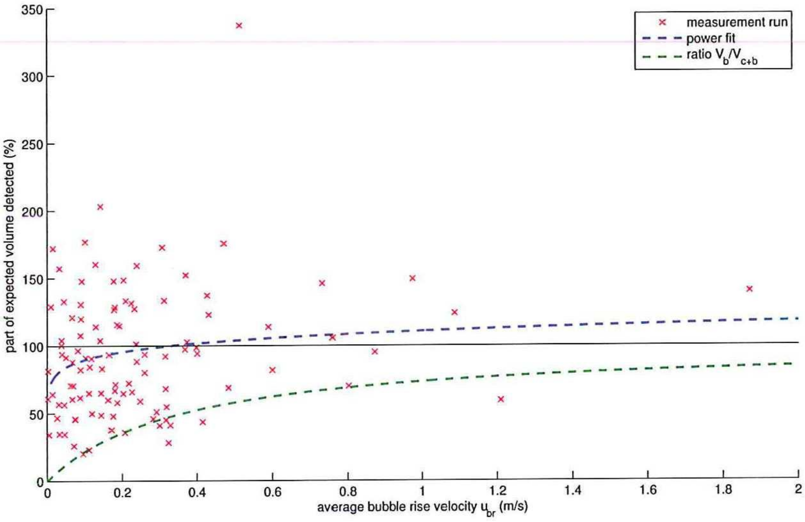

Figure 4.31: Plot that shows the mean bubble rise velocity and the ratio of the detected and expected volume of every measurement run, the blue line is a power fit, the green line is the ratio of the bubble to cloud volume for a u_{mf} of 12 cm/s.

The low threshold selection and because of that, a too high volume that is recovered, might explain why the Hilligardt and Werther model consistently over-predicts the bubble rise velocity; it uses bubble diameter as an input.
The percentage of matched bubbles doesn't say much about the volume that is lost in this way; the unmatched bubbles are usually the smaller bubbles or only noise and not even a real bubble.

It might also be that the calibration is not suitable for all heights in the bed. The reference measurements that were used to correct for the drift in the detectors were done only once a day, at an arbitrary height. The voidage of the bed will have an impact on the amount of radiation that is detected. The voidage low in the bed might be different from the voidage high in the bed. For a bed that is fluidized using very high velocity gas this is a well known fact (Kunii and Levenspiel (1991) chapter 8), but for velocities used in our measurements this is not expected. Comparing the detectors signals of the bed that is minimally fluidized at different height should therefor give roughly the same result. This was done for the atmospheric distribution plate measurements. The result can be found in the table below.

height above plate	mean array 1	mean array 2	mean array 3	mean all
126 mm	562.6	560.3	470.3	531.1
156 mm	563.3	559.7	471.0	531.3
199 mm	568.6	566.3	475.0	536.6
279 mm	573.1	570.8	477.9	540.6
359 mm	566.4	564.2	473.6	534.8
439 mm	563.8	562.5	469.0	531.8
519 mm	564.1	583.5	497.1	548.2

This shows that the signal of a minimally fluidized bed will not change significantly with height. The different pressures do not effect this either.

The reconstructions can also be studied. First the pixels that have been identified as being part of a bubble are set to zero. The values of the other pixels are add up. This "rest signal" would be zero in an ideal case. That would mean that there is no noise and the calibration is perfect. If these values are high this would mean that there is a lot of noise or the calibration does not represent the situation in the bed very well. If the rest signal is averaged for the different pressures and plotted for the height at which the bed is studied, figure 4.32 is obtained. It must be said that these results were obtained from only the first few seconds of the reconstructions. Doing it for the entire 60 second data set would take too much time and, considering the two test cases that have been done up to 60 seconds, does not give very different results.

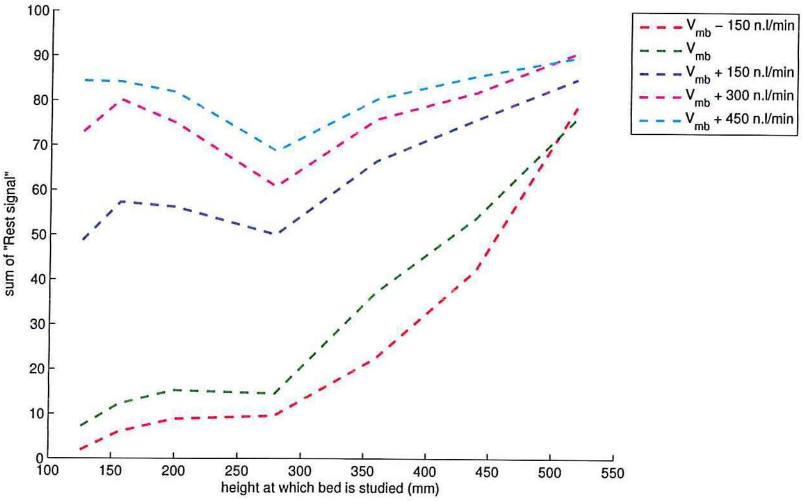

Figure 4.32: Plot of "rest signal" after pixels detected as bubbles have been removed. Lines are averaged values for all pressures.

It is clear that at higher flow rates there is more "rest signal". Also the height at which the bed is studied has a strong influence on the amount of rest signal. This could mean that the noise would increase for higher flows and heights, but this is not seen in the raw signal. It would also be difficult to explain considering that the only thing that changes is the table height. This seems unlikely.

This means that the calibration does not give a good representation of the bed at high flows and high above the distribution plate. This might also explain why these measurements show a too high recovered bubble volume. The voidage of the bed might increased significantly, although this does not show up in the raw detector signal.

In all plots the mean bubble size is used, the error in this value should be smaller than the error in the detected size of a single bubble. It is difficult to give an indication of the error in this value, because the measurement will be different every time. The standard deviation will give an indication of the variation of the values found.

The daily drift in the detector signal can for a great deal be dealt with using the daily correction factor. Of course this can only give an indication at that moment in time. But doing a reference measurement for every measurement would be very cumbersome.

The height at which the bed is studied is controlled by raising or lowering the vessel on a vertically adjustable table. This table is moved using a hydraulic ram. Over longer periods of time the table will slowly drop. This is in the order of a few millimeters overnight. During a 60 second measurement run this drop can safely be ignored. The height of the table compared to the floor was measured using a flexible steel rule. The floor consists of wooden sheets, which are a little bit flexible, so there might be an error of a few millimeters. This is also negligible compared to the other sources of errors.

The correct alignment of the vessel in the middle of the setup is quite important. The vessel is held in place by metal studs. The alignment of the vessel with the X-ray sources was checked using a dedicated wooden fitting rod. This was done each time the height of the table was changed. A misalignment of a millimeter or 2 might have occurred, but this will not have had significant effects.
The stainless steel that is used as a material for the vessel will cause a detectable amount of noise in the signal. The X-rays are scattered much more by steel than by, for instance, perspex. However, since the measurements are done at high pressure, the strength of the steel is required.

4.2 Fines effects

For 6 mixtures of fines measurements were done to study the effect of fines on bubble size. These mixtures consist for a part of base particles, PurAlox SSCa-5/200 and part fines, PurAlox SCFa-230. The mean particle size for SSCa-5/200 was determined to be 77 μm and 38 μm for SCFa-230. See figure 4.33 for the detected particle sizes. The bulk density of these particles is 680 kg/m^3 and 620 kg/m^3, respectively.

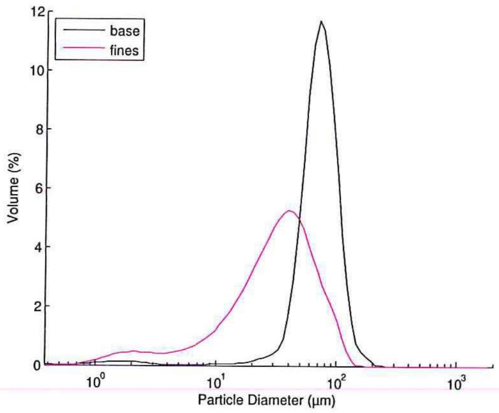

Figure 4.33: Particle size distribution for base (SSCa-5/200) and fine (SCFa-230) particles.

A mix of particles consists of a batch of 22.5 kg of particles. The fines content is expressed in weight-percentage, ranging from 0 to 50%. These mixtures were used to measure bubble properties at various heights and gas velocities. The measurements were only done relatively high in the bed because lower in the bed the bubbles will be too small to detect accurately. The measurements for different heights were only done at a gas velocity of 8 cm/s. The measurements for different gas velocities (2 - 10 cm/s) were all done at 500 mm above the distribution plate. Even at the lowest gas velocities bubbles can clearly be seen. The minimum bubbling velocity was reached the moment the gas flow controller started working, if was not possible to determine the minimum fluidizaton or bubbling velocities accurately using this controller. The minimum fluidization velocity will be around 0.3 cm/s, according to literature.

An overview of the measurement settings is shown in the table below.

Fines content	Heights above plate	Gas velocity
0 $\%_{weight}$	300 mm	2 cm/s
10 $\%_{weight}$	350 mm	4 cm/s
20 $\%_{weight}$	400 mm	6 cm/s
30 $\%_{weight}$	450 mm	8 cm/s
40 $\%_{weight}$	500 mm	10 cm/s
50 $\%_{weight}$		

All measurements were done in the perspex column, with an inner diameter of 24 cm. The top of the column was closed by a lid, with filters attached to it inside the column.

Previous work (e.g. Beetstra et al. (2009) or Krishna (1988)) has shown that if the fines content of a particle mixture is increased, the bubble size will decrease and so the conversion-rate for chemical reactions will increase. The reduction in bubble size should be visible in measurements from the X-ray setup.

4.2.1 Calibration and threshold

Using the same method as with the polystyrene particles a calibration was done using the base particles (same as 0% fines). This calibration was used for all mixes, the detector signal does not differ very much from mix to mix.

Using the 52 mm inner diameter phantom a threshold was selected. A threshold value of 0.12 gave satisfactory results (99% or surface area recovered).

If this threshold value is used on the actual measurements it appears that only noise is detected. If a higher threshold is chosen, the measurements start to make more sense, see figure 4.34. A threshold of 0.4 will lead to bubbles that appear to be connected, which should have been detected as separate bubbles. If a value of 0.6 is used too much information will be lost. A value of 0.5 seems to be a reasonable compromise. This is also the value that was previously used by Mudde et al. (2010).

The calibration together with the threshold determined using a phantom, make it possible to determine bubble sizes accurately. If the threshold is set to a higher value, the detected volumes will be smaller, because more pixels are considered to be part of the bulk of the bed.
As a consequence the the detected sizes are no longer a correct representative of the true bubble size. That is why the bubble size is sometimes normalized at 0% fines to be able to compare the results. A similar approach is used by Beetstra et al. (2009).

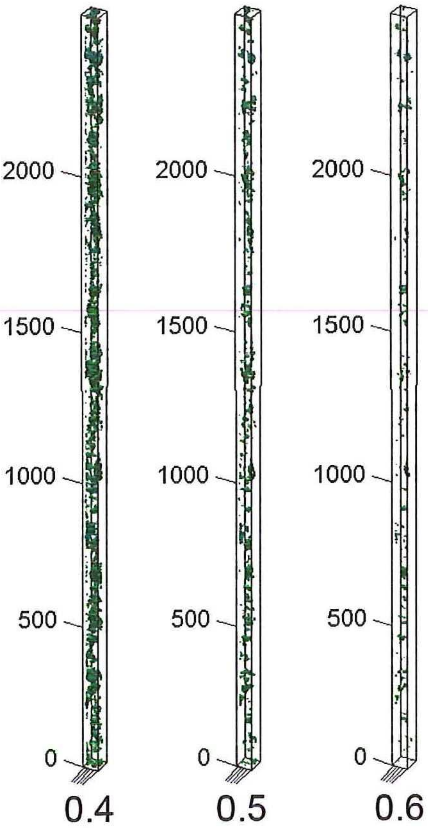

Figure 4.34: Consequences of threshold choice, detected bubbles in first 2500 samples of 40% fines, 8 cm/s gas velocity, 500mm above the distribution plate. A threshold of 0.4 is too low and 0.6 too high. 0.5 was used.

The reason that such a high threshold value is required is that the calibration does not seem to represent the bed once it is in a fluidized state. The bed expands quite significantly when it becomes fluidized. If the bed is at rest it has a height of about 50 cm. It becomes about 10 cm higher when it becomes fluidized. If the fines content is increased, the bed seems to expand even more. Once the gas flow is turned off, it slowly settles back into the state it had at rest. This can take several minutes.
Even if there are no bubbles present in the (minimally) fluidized bed, the bed density is not the same as in the calibration (rest) state. The reconstruction program will recognize this as a bubble. But since it sees this on all it's detectors, it will smear this detected 'bubble' all over the reconstruction. If the detector signals were noiseless, this would lead to a uniformly gray reconstruction. In real measurements this leads to reconstructions such as in figure 4.35.
The different fines mixtures have a slightly different density, ranging from 680 kg/m^3 for 0% fines to 650 kg/m^3 for 50% fines, and also a slightly different X-ray absorption. If the average of the signal of a full bed at rest is compared to the base particles used for calibration (same as the 0% mixture), the differences are larger than the day to day drift that is to be expected. But they do not vary consistently depending on fines content; there is no clear relation visible, see figure 4.36. Using the correction factor will be the most effective solution to correct for these differences, because doing a calibration for every mixture will take a lot of time.

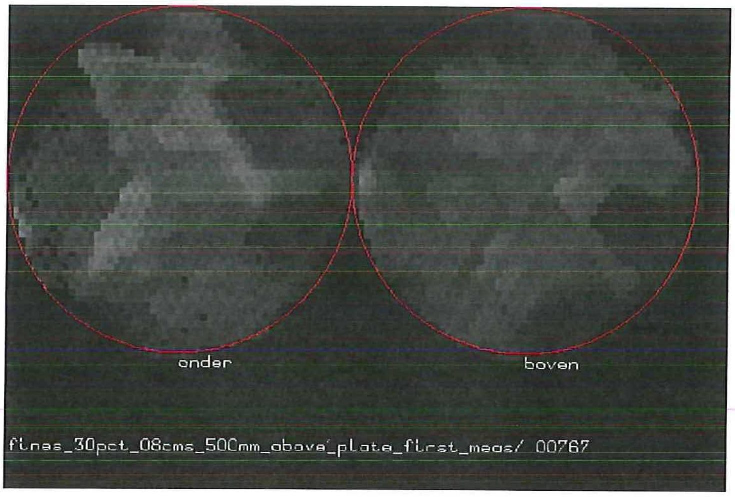

Figure 4.35: Reconstructed tomogram of 30% fines, 8 cm/s gas velocity, 500mm above the distribution plate. No bubble is present, but a 'bubble' is smeared out over the whole plane.

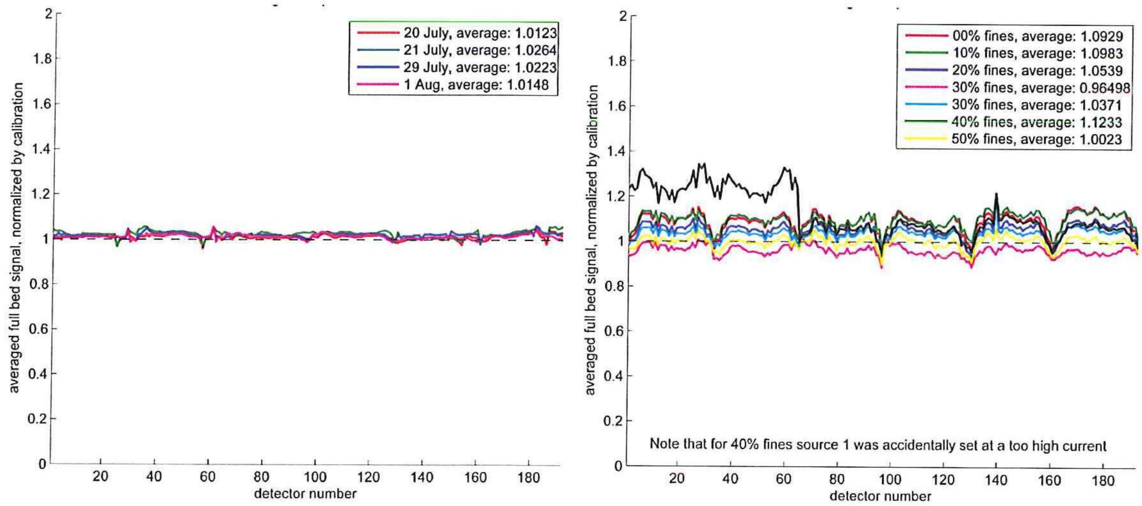

Figure 4.36: Full bed at rest, measurements done on various days for the 607 μm polystyrene particles (left) and for different fines mixtures (right). Both are normalized using their respective calibrations. The 30% mixtures was studied twice and the 40% measurement was done using X-ray source 1 set to a too high current. The data for the 40% mixture was obtained using the correct settings.

4.2.2 Spherical equivalent diameter

As mentioned before, the bubble volume that is detected is not the true bubble volume, because the threshold is chosen in quite arbitrary way. It is not obtained using a calibration. That is why the mean spherical equivalent bubble diameter is normalized for several plots.

Studied at various heights

The measurements have been done at different heights in the bed, ranging from 35 to 50 cm above the distribution plate. These measurements were all done at a superficial gas velocity of 8 cm/s. The results are plotted in figure 4.37. This plot shows that raising the fines content of a mixture will lead to smaller bubbles. However, it should be noted that the bubble diameter that is given will be a under estimate, due the high threshold that was needed. These results can also be normalized at 0% fines (figure can be found in appendix C), this shows that higher in the bed the addition of fines makes a slightly bigger difference. The averaged bubble diameter reduction over all heights for the different fines contents is shown in the table below.

Fines content	$10\%_w$	$20\%_w$	$30\%_w$	$40\%_w$	$50\%_w$
Relative size	-3.3%	-7.6%	-16.8%	-16.2%	-21.1%

Studied at various flows

The measurements have been done at superficial gas velocities ranging from 2 to 10 cm/s. The bubble diameters were normalized at 0% fines content and plotted in figure 4.38. This shows that there is a reduction in bubble diameter for all gas velocities. The graph that shows the not-normalized data can be found in appendix C. The average bubble diameter for all flows was compared to the initial diameter. The results are shown in the table below.

Fines content	$10\%_w$	$20\%_w$	$30\%_w$	$40\%_w$	$50\%_w$
Relative size	-1.9%	-7.3%	-9.2%	-13.6%	-21.7%

These results can be compared directly with the results by Beetstra et al. (2009). In her paper she describes an automated setup were bubble sizes were determined using observed pressure fluctuations and data from optical probes. The experiments were conducted in a stainless steel column of 40 cm high with an internal diameter of 7.3 cm. The results of this comparison can be seen in figure 4.39. It should be noted that the measurements done by Beetstra were done at a height of 14 cm, whereas the measurements by the author were done at 50 cm above the distribution plate. The results by Beetstra show a larger reduction in bubble size. The same kind of particles were used for both the authors and Beetstra's measurements. The clear growth of bubbles at low gas velocities seen by Beetstra in the results based on pressure fluctuations, is not observed by this author. Beetstra did not see this growth in the optical probe measurements. She speculated that the smaller bubbles might move around the probes, so only larger bubbles would be detected. Detecting small bubbles using the X-ray setup is also difficult, especially with the high threshold value. So they might not have been detected by the X-ray setup either.

Studied at various fines contents

The fines content of the mixtures varied from 0 to 50 %. These have been plotted separately as well, either for various bed heights (figure 4.40) or various gas velocities (figure 4.41).

Summary

It is clear that the addition of fines will result in a significant reduction in bubble size. Although the reduction is less than is reported in literature (up to 40 %), a reduction of up to about 20% is still observed. Especially when the bed is studied at high gas velocities and far above the distribution plate.

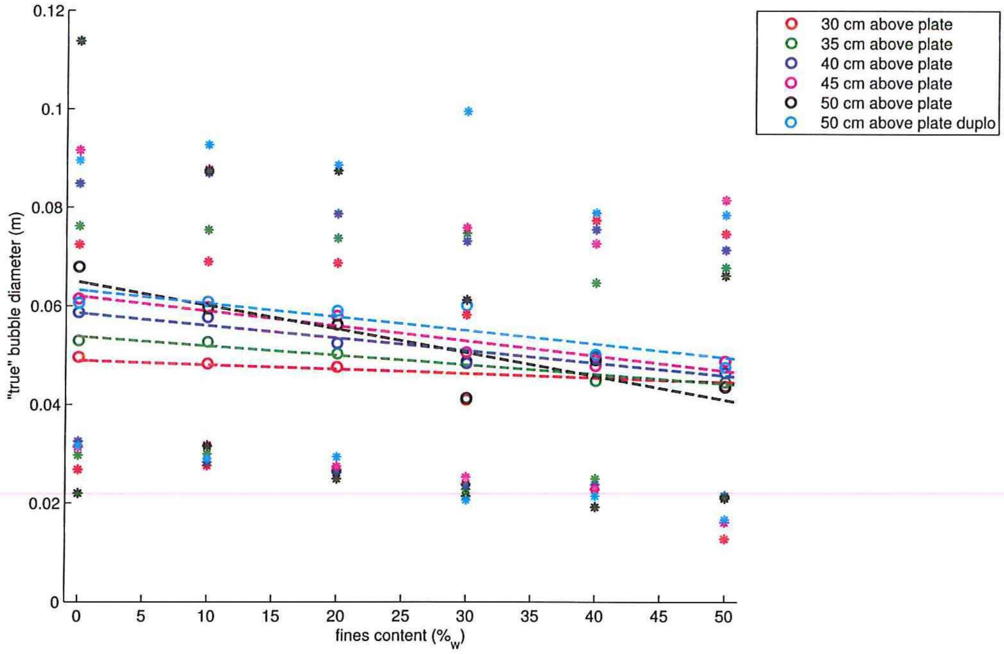

Figure 4.37: Bubble size, fines, various heights: Spherical equivalent bubble diameter for various fines contents at several heights in the bed. Superficial gas velocity is 8 cm/s. Dashed lines are linear fits.

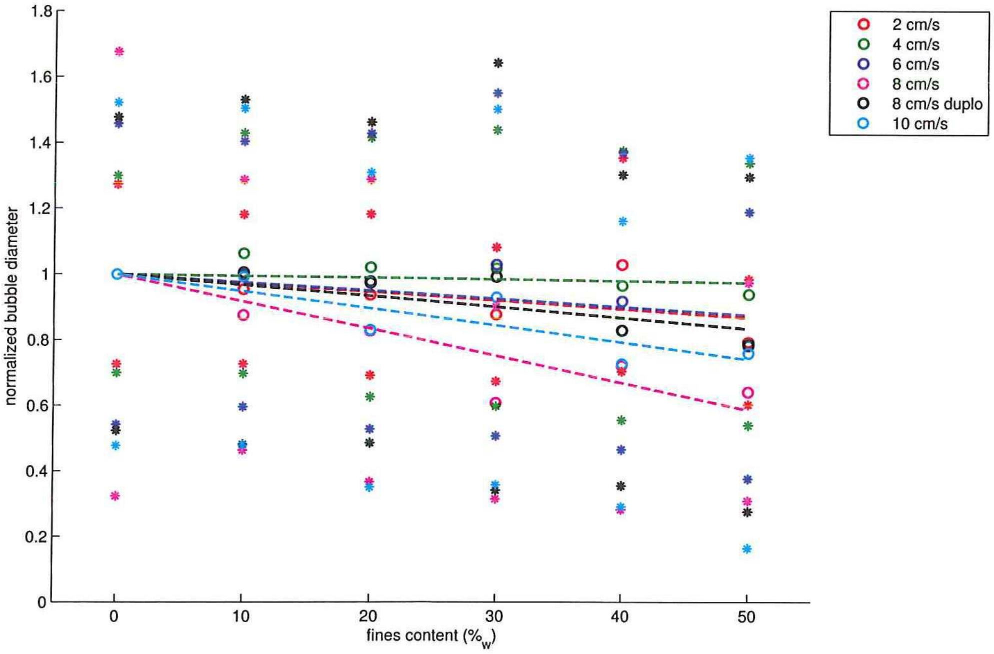

Figure 4.38: Bubble size, fines, various flows: Normalized spherical equivalent bubble diameter for various fines contents at several superficial gas velocities. The bed is studied at 500 mm above the distribution plate. Dashed lines are linear fits.

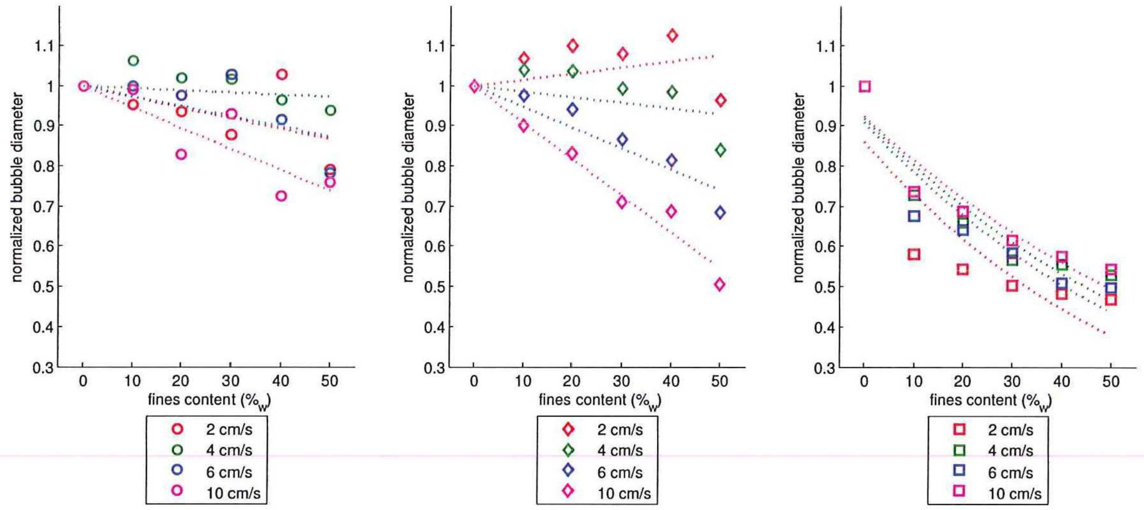

Figure 4.39: Normalized spherical equivalent bubble diameters for various fines contents at several gas velocities. Left: measurements done by this author. Center: pressure fluctuation measurements done by Beetstra et al. (2009). Right: optical probe measurements done by Beetstra et al. (2009). Dashed lines are linear (left and center) and exponential (right) fits.

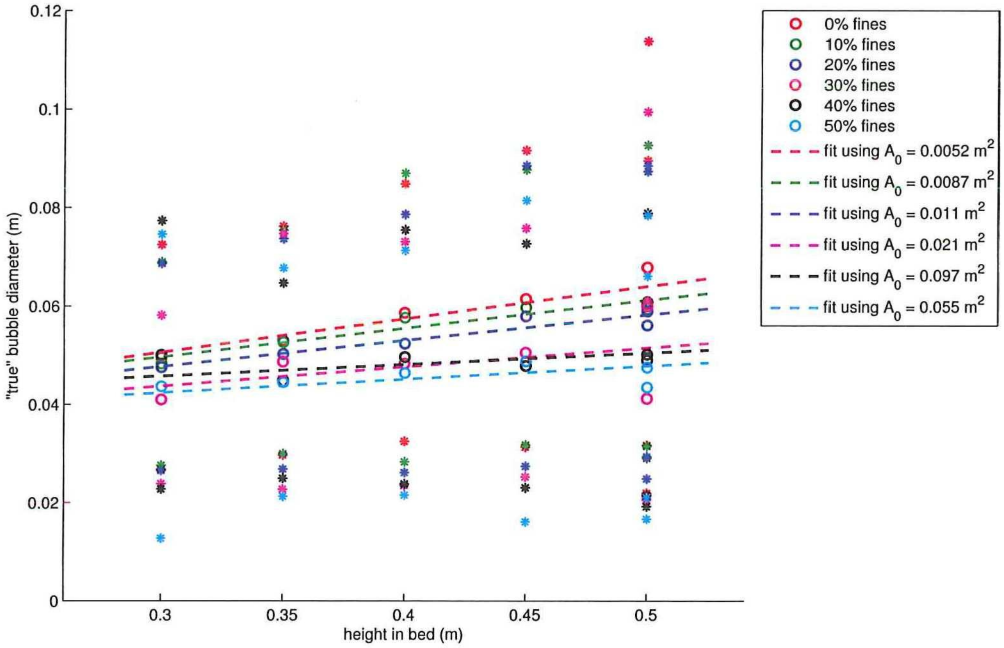

Figure 4.40: Bubble size, fines, various fines contents: Spherical equivalent bubble diameter for various heights in the bed for several fines contents. The gas velocity is 8 cm/s. Dashed lines are fits using Darton's model.

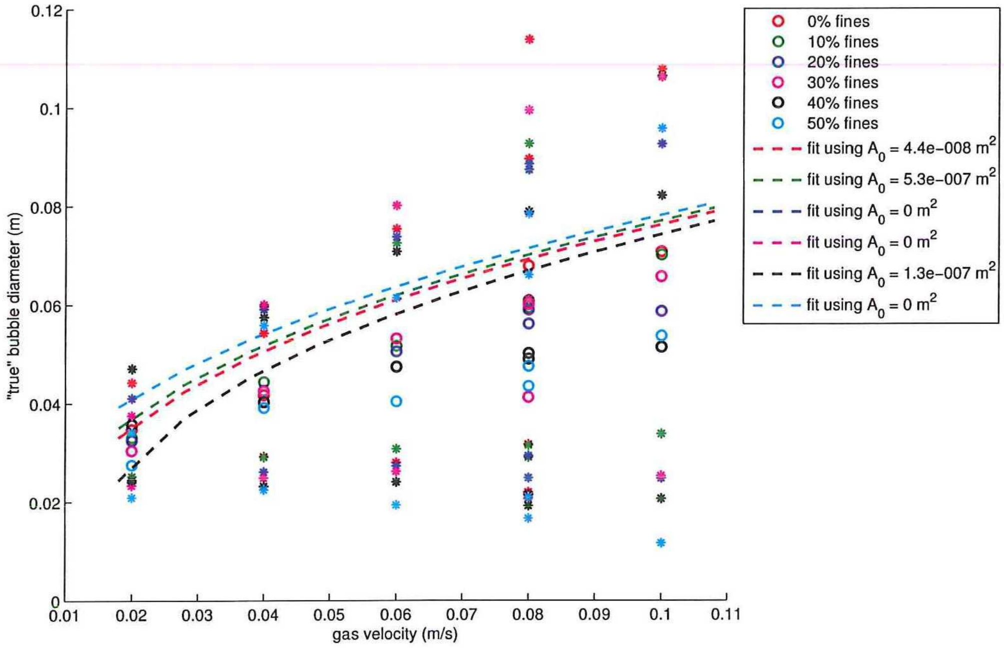

Figure 4.41: Bubble size, fines, various fines contents: Spherical equivalent bubble diameter for various superficial gas velocities at several fines contents. The bed is studied at 500 mm above the distribution plate. Dashed lines are fits using Darton's model.

4.2.3 Bubble rise velocity

The bubble speed is also determined from the measurements. These speeds will be more reliable than the bubble volumes, which were unreliable due to the high threshold value. The speed is determined from the time at which the center of the bubble passes the measurement planes. This will not be affected as much by the threshold choice. The model by Hilligardt and Werther (1986) should be able to predict the bubble rise velocity.

Studied at various heights

The bed is studied at different heights at a gas velocity of 8 cm/s. The results are plotted in figure 4.42. The model shows results that are very close to the measured values at low fines contents. The higher the fines content, the more the bubble speed is over-predicted. The fact that the model matches the measurement data is slightly surprising because the model uses the detected spherical equivalent diameter of the bubbles as an input.

Studied at various flows

The speed can also be detected for various gas velocities. The results are shown in figure 4.43. Again the model gives values that a slightly too high if the fines content is high.

Studied at various fines contents

The bubble rise velocity can also be studies for different fines contents. The results plotted against the height at which the bed is studied are shown in figure 4.44. The results plotted against the gas velocity can be found in figure 4.45. Both plots clearly show that the model over-predicts the bubble rise velocity at high fines contents. For low contents it appears to match quite well.

Summary

Overall the results for the bubble rise velocities give a good indication of the effect of fines. Increasing the fines leads to smaller bubbles, which will rise more slowly. But the fines seem to make the bubbles rise even slower than could only be explained by the decrease in size.

4.2.4 Error estimation

In several plots the results for the 30% fines measurements show a slightly lower value than might be expected, based on the trends. This can be explained by the fact that the filters might have become clogged during these measurements. This was not always noticed immediately and lead to the exhaust of the vessel being blocked and a slow build up of pressure inside the vessel. As seen earlier in this report, a higher pressure leads to smaller bubbles.

For instance, the measurements done at 50 cm above the distribution plate at a gas velocity of 8 cm/s for the 30% mixture, were done twice, as for all mixtures at these settings. Of these two resulting data points for the 30% mixture, one lies were it would be expected, based on the trends. But the other shows a much smaller spherical equivalent bubble diameter, 4.1 cm compared to 6.0 cm. Looking at the measurements done at different vessel pressures (see figure 4.13), the increase in pressure due to the filters getting clogged could be estimated to be around 2 bar. However, it should be noted that the particles studied here are Geldart A particles, whereas the pressurized measurements were done using Geldart B particles. Also, the gas velocity was not constant, since the pressure increased gradually. This makes it difficult to compare the results. Geldart A particles generally show a more dramatic reaction to increases in pressure, so the increase in pressure will probably be significantly less than 2 bar.

Half-way the 30% fines measurement series the column built up too much pressure, which led to a small crack in the perspex column. This measurement was discarded of course. After the column was repaired, the vessel was extended using an extra 50 cm section and the filters were monitored more carefully. The addition of the extra 50 cm column section greatly reduced the amount of dust that was

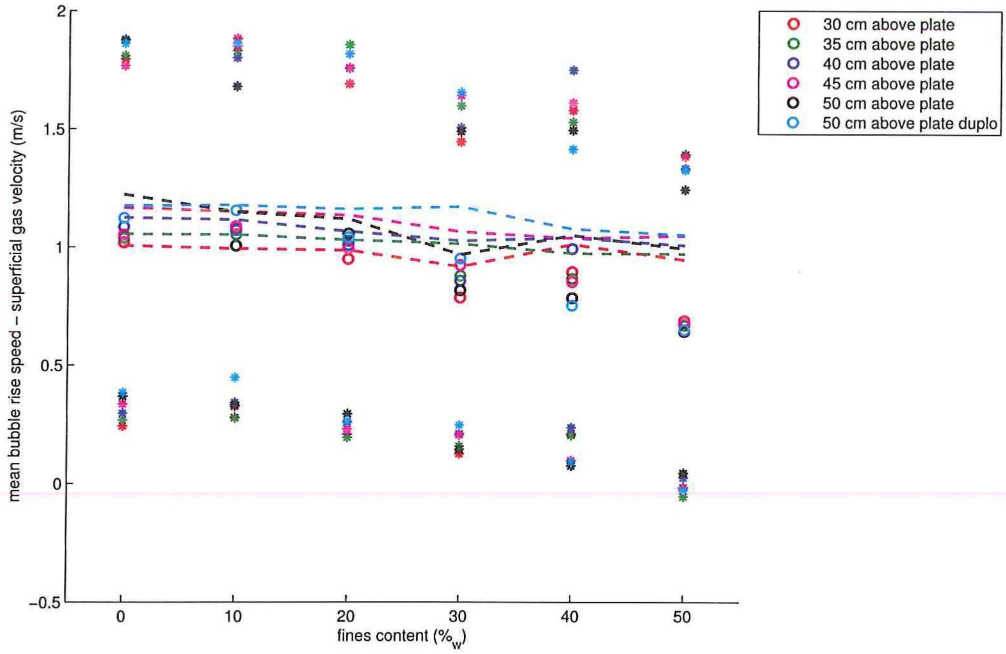

Figure 4.42: Bubble velocity, fines, various heights: Bubble rise velocity for various fines contents at several heights in the bed. Superficial gas velocity is 8 cm/s. Dashed lines are made using the Hilligardt and Werther model.

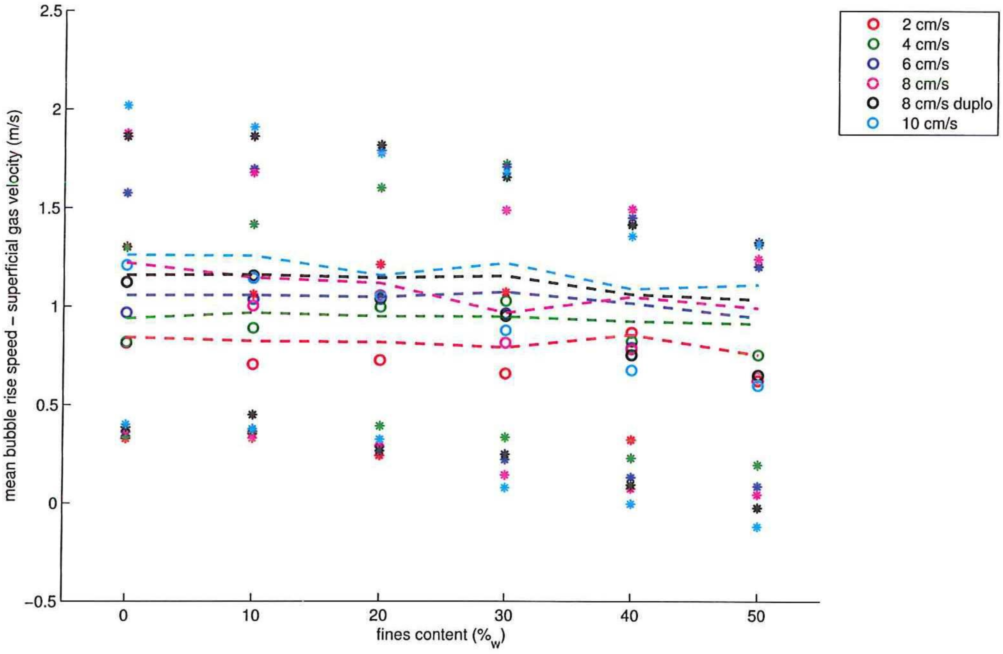

Figure 4.43: Bubble velocity, fines, various flows: Bubble rise velocity for various fines contents at several superficial gas velocities. The bed is studied at 500 mm above the distribution plate. Dashed lines are made using the Hilligardt and Werther model.

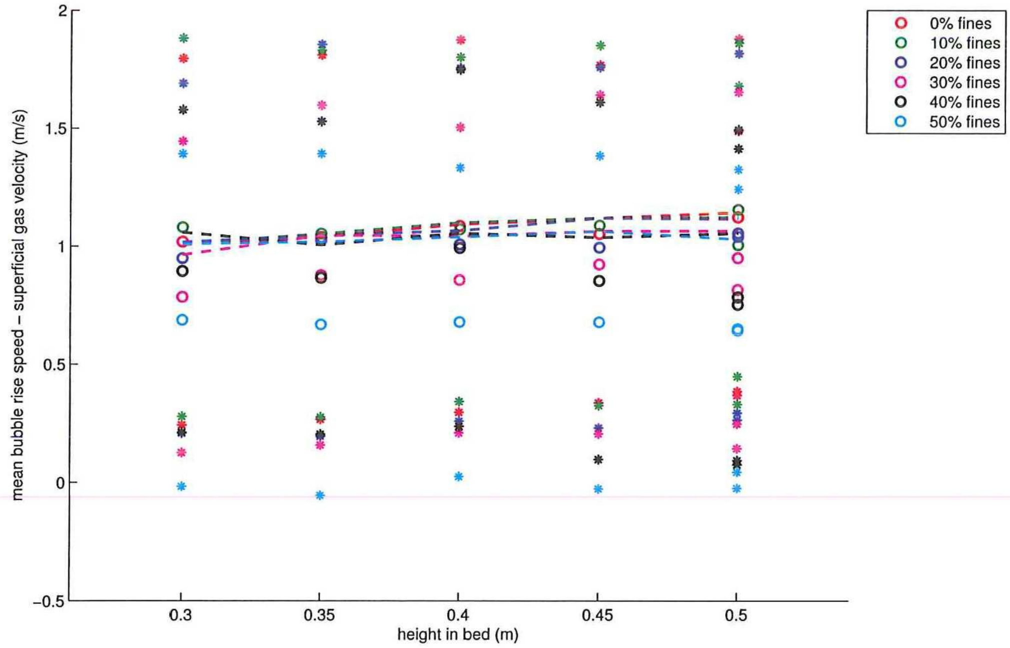

Figure 4.44: Bubble velocity, fines, various fines contents: Bubble rise velocity for various fines contents at several superficial gas velocities. The bed is studied at 500 mm above the distribution plate. Dashed lines are made using the Hilligardt and Werther model.

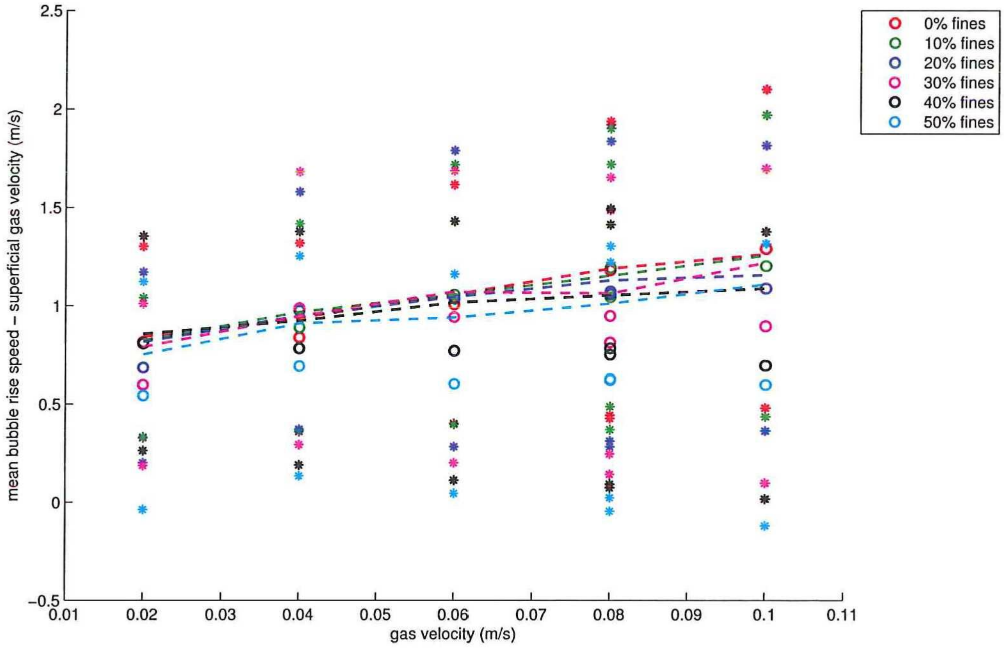

Figure 4.45: Bubble velocity, fines, various fines contents: Bubble rise velocity for various fines contents at several superficial gas velocities. The bed is studied at 500 mm above the distribution plate. Dashed lines are made using by the Hilligardt and Werther model.

collected on the filter surface.

The measurements at 50 cm above the distribution plate and a gas velocity of 8 cm/s were done twice to verify the consistency of the measurements. In some cases these measurements gave significantly different results.

The same sources of error will play a role as in the pressure measurements. The noise in the detector signals will be less in this case, because the vessel is made of perspex instead of stainless steel.

Because the bed expands significantly before it becomes fluidized, the full bed calibration is not an accurate representation of a fluidized bed without bubbles. This mismatch causes the relatively high noise seen in the reconstructions, see figure 4.35. This requires the use of the very high threshold value. Due to the mismatch of the calibration, the reconstruction program always tries to distribute the wrongly detected gas. If a bubble is actually present, it's detected size will most likely be too high. This is interesting, because that could explain why the bubble rise velocities are correctly predicted by the Hilligardt and Werther model, which used bubble size as input. The detected bubble sizes might not have been so bad.
To get a feeling for this, the same can be done as has been done with the pressure-measurements; the total detected bubble volume should be about the same as the total gas flow minus the gas flow needed to fluidize the bed. To be able to calculated the expected volume, the minimum fluidization velocity must be known. This was not determined in these measurement series. The value determined by Beetstra et al. (2009) was around 0.3 cm/s. This values was used to obtain the results in the table below.

measurement	bubbles matched	expected	detected	performance
fines_00pct_02cms_500mm_above_plate	81%	0.046 m^3	0.011 m^3	24%
fines_00pct_04cms_500mm_above_plate	83%	0.10 m^3	0.032 m^3	32%
fines_00pct_06cms_500mm_above_plate	79%	0.15 m^3	0.087 m^3	56%
fines_00pct_08cms_500mm_above_plate	77%	0.21 m^3	0.12 m^3	57%
fines_00pct_08cms_500mm_above_plate_duplo	82%	0.21 m^3	0.35 m^3	169%
fines_00pct_10cms_500mm_above_plate	79%	0.26 m^3	0.20 m^3	76%
average all measurements				42%

These results are generally much lower than seen for the Geldart B pressurized measurements. Most of them are between 20 and 60%, as can be seen in the histogram in figure 4.46.
If the ratio between the expected and detected volume is plotted for various heights and gas velocities (figure 4.47), a similar trend as seen previously is seen. Although the very high ratios, well about 100%, are not seen. This suggests that the size of the cloud around the bubbles might also play a role, like in the Geldart B particles measurements. This can be verified in the same way as has been done before, see figure 4.48. Nearly all measurement runs are below the V_b/V_{c+b} ratio. This ratio approaches unity quickly because of the low minimum fluidization velocity. This suggests that the high threshold might have more impact on the detected bubble volumes than the cloud around the bubbles.

The "rest signal" of the reconstructions is also studied for the fines measurements. This is done in the same way as with the pressurized measurements. The result can be seen in figure 4.49. This shows that there is a lot more rest signal in the fines reconstructions than in the pressurized reconstructions. This is caused by the high threshold choice. Also it is clear that there is much more rest signal if the fines content goes up. There is not such a clear effect caused by the increasing height or gas velocity. The increase of rest signal with increasing fines is caused by the fact that the calibration becomes a worse representation of the situation in the bed once it becomes fluidized. During the measurements it was observed that increasing the fines content leads to a more significant bed expansion before it becomes fluidized. Therefor the voidage will have increased, which in turn increased the amount of rest signal.

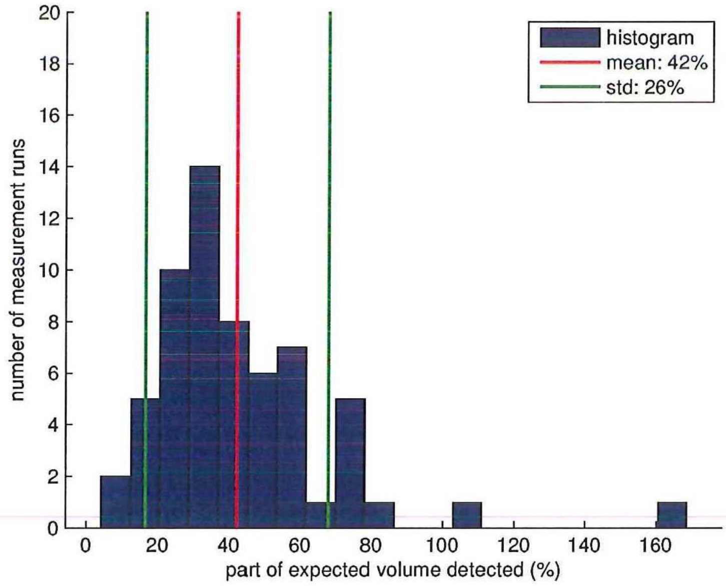

Figure 4.46: Histogram that shows the ratio between the actually detected volume of the bubbles and the expected volume based on the assumption that bubbles contain their gas (ping-pong balls) for the fines measurements. The mean is 42% with a standard deviation of 26%.

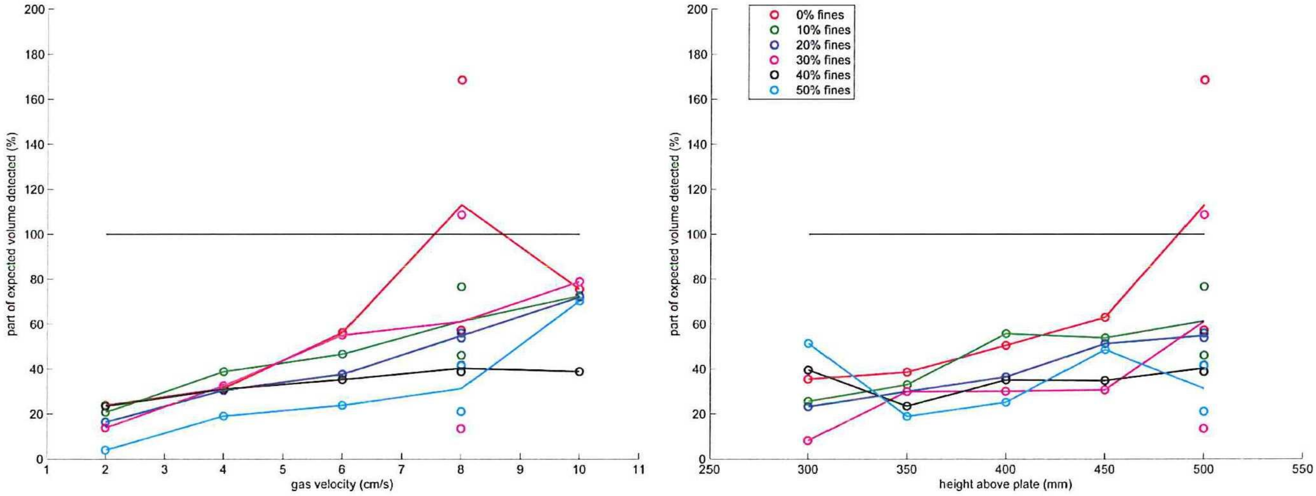

Figure 4.47: Plot that shows the ratio between the actually detected volume of the bubbles and the expected volume based on the assumption that bubbles contain their gas (ping-pong balls) for various gas flows and heights for the fines measurements.

To see if all bubbles were detected by the X-ray setup the surface of the bed was filmed using a high speed camera. The camera was set at 200 frames/s. The bed was studied just underneath the surface using the X-ray setup. Both the X-ray detector signal and the high speed camera recorded about 5 bubbles per second at a superficial gas velocity of 1.1 cm/s. This means that the detection of the amount of bubbles high in the bed is reliable, this says nothing about the reliability of the bubble size or velocity that is detected using the X-ray setup.

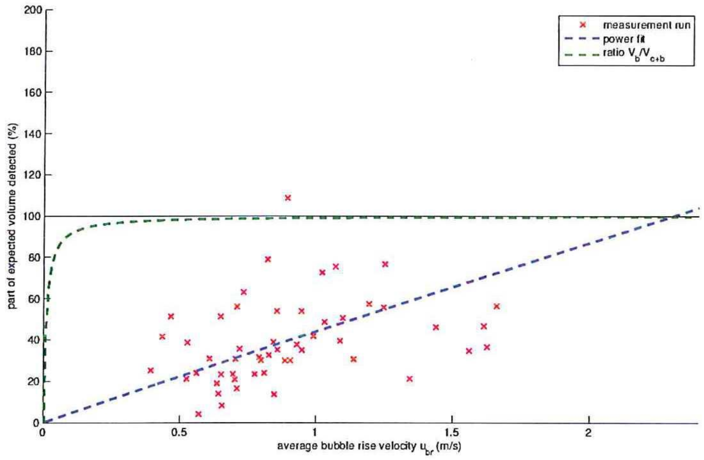

Figure 4.48: Plot that shows the mean bubble rise velocity and the ratio of the detected and expected volume of every fines measurement run, the blue line is a power fit, the green line is the ratio of the bubble to cloud volume for a u_{mf} of 0.3 cm/s.

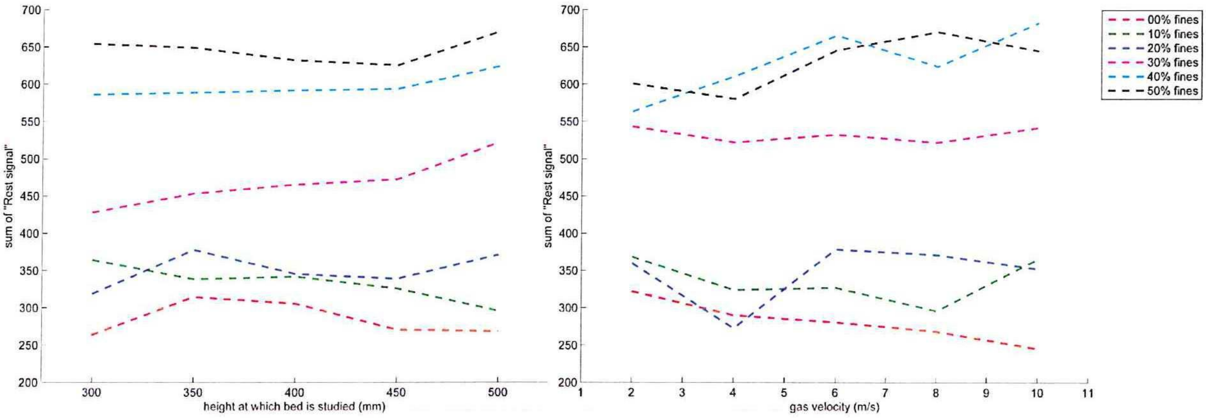

Figure 4.49: Plot of "rest signal" after pixels detected as bubbles have been removed from fines measurements. Left for different heights at a gas velocity of 8 cm/s and right for different gas velocities at 500 mm above the distribution plate

4.2.5 Filter solution

The fine particles used in the fines measurements cause a lot of dust when fluidized, especially at speeds beyond 6 cm/s. This is unwanted for two reasons. First, the smallest particles are ejected from the bed the most, this will change the particle size distribution during the measurement. Second, the room will get very dusty, which is bad for the electronics in the room and might be harmful for the people that work there. A solution to this problem was found using simple and readily available materials.

The vessel was closed by installing a lid on top of the column. In this lid three filters were installed, see figure 3.5. These filters were quite effective in stopping particles from leaving the vessel. Particles are stopped and stay on the filter surface. This makes it necessary to tap the filters after every measurement run to clean them. The more clogged the filters are, the higher the pressure drop over these filters will be. This pressure drop is undesirable as it will pressurized the perspex column. If the pressure becomes higher the gas will start leaking out at the mating surfaces of the various column sections.

In extreme cases the filters can get completely clogged and if the column is put together tightly, it will not let out any gas anymore. This will cause the pressure to build up inside the column. If the pressure of the supply line is high enough this will damage the perspex column. This has happened on one occasion. The supply line pressure was very high (~6 bar). This pressure was lowered from that moment on. It was set so that it was still possible to achieve the desired gas velocities, but no higher than that.

The current filter setup still lets through a very small amount of particles. If the setup were to be pressurized the exiting air will be passed through a valve. These valves can be damaged by these fines particles. Multiple filters in series could be a solution if pressurized measurements are done using small particles. Particles that pass the first filters will not be able to be returned to the bed by tapping the filters. Using higher quality filters might improve performance as well.

4.2.6 Lifting of the bed

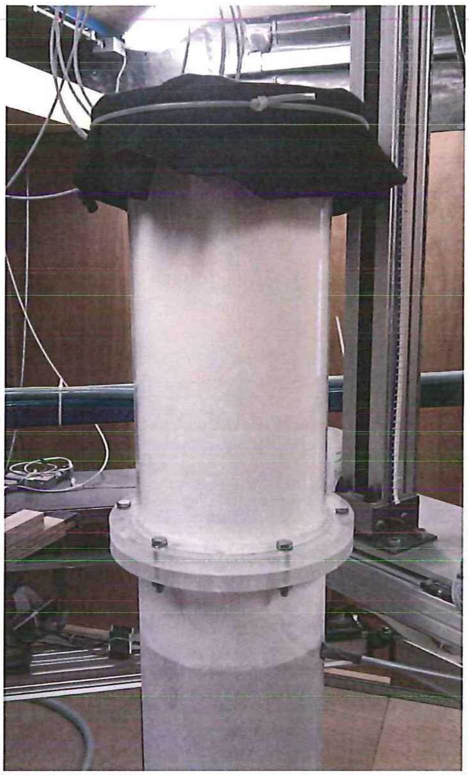

Figure 4.50: The vessel after a mixture of fines has risen to the top of the column and completely blocked the filters. Black cloth on top is used as an extra filter.

If the bed of smaller particles is fluidized from rest, it will be lifted as a plug inside the column at first. It will start to crumble from the bottom and form a fluidized bed on top of the distribution plate, until the entire plug of particles has been broken up in this way. If the gas velocity is set very high from the beginning, the plug will rise quickly to the top of the vessel, blocking the filters, before it can completely crumble, see figure 4.50. This will prevent any gas from passing through the filters. That is why the bed must be fluidized by slowly increasing the gas velocity. Especially if the bed has been left overnight. The particles seem to stick more to each other if the bed has not been fluidized for a while.

The sticking of the particles is also seen with the larger polystyrene particles. The sticking is probably due to moisture getting into the bed. Leaving the bed to run for a while will remove this moisture.

4.3 Particle distribution after fluidization

After the beds of various fines mixtures have been fluidized they were switched off abruptly. The vessel was opened and samples of the particles were taken at the bottom (5 cm above distribution plate), around half-way the bed (35 cm above distribution plate) and just below the bed surface. If the particles were taken directly from the surface the dust that has fallen down from the filters will give a distorted picture.

Of these samples the particle size distribution was determined and compared to the roughly expected distribution based on the measurements of the base and fine particles separately. For the 20% and 30% mixtures the results have been plotted in figure 4.51 and 4.52, respectively. Plots for the other mixtures can be found in appendix D.

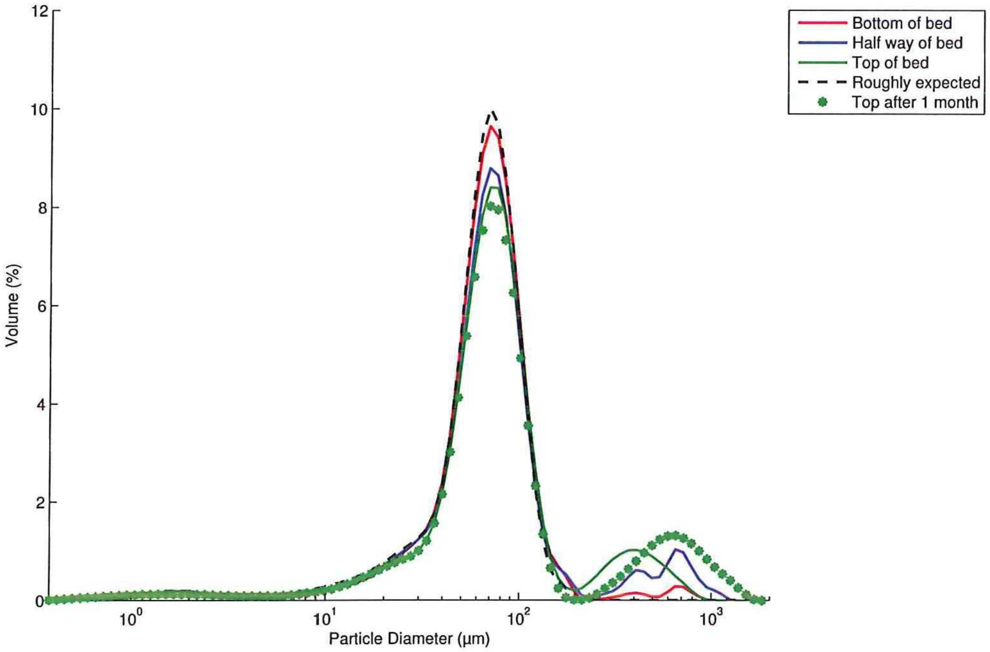

Figure 4.51: Particles size distribution for 20% fines mix. The amount of large particles ($\sim 500\mu$m) is unexpected.

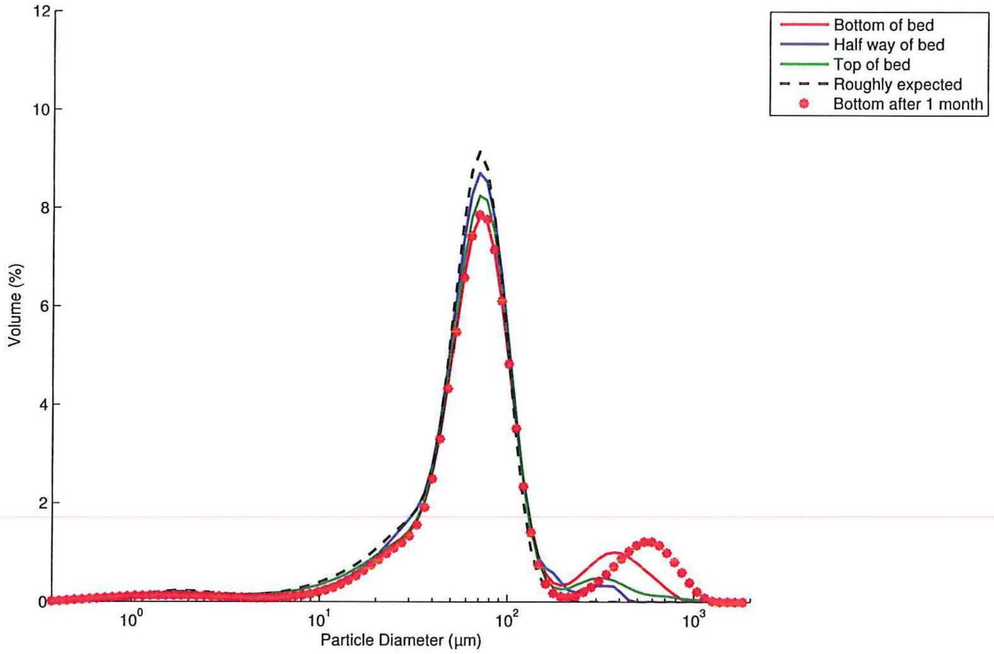

Figure 4.52: Particles size distribution for 30% fines mix. The amount of large particles ($\sim 500\mu$m) is unexpected.

There is no consistent difference in particle size distribution for the various bed heights. This means that the bed is well mixed. The gas velocity before the flow was switched off was 8 cm/s.

In all these measurements significant amounts of large particles ($\sim 500\mu$m) are detected. These are unexpected as they have not been found in the base and fines particles separately. The movement of the particles inside the perspex column might have charged the particles. If particles stick together they will be detected as a larger particle. The particles have been left in glass jars for about one month. After that, their size distribution was determined again. This is shown using the stars in the plots. The large particles are still detected. Actually even larger particles are detected. The electrical charge would have been gone after a month of being at rest. This suggests that another mechanism is responsible for the particles sticking together. Moisture is a likely candidate.
The base and fine particles showed the big particles as well after being stored for a month. This rules out the possibility that the large particles were 'made' during fluidization.

4.4 Bubble shape

Using the X-ray setup it is possible to create pseudo-3D images of the bubbles in the bed. The images show bubbles with spherical capped nose and a cusp at the bottom. A few bubble are shown in figure 4.53. Of course there are also bubbles that do not have such typical shapes. These are pseudo 3D-images since the z-axis is actually time, instead of space. These images are similar to the images produces by Kai et al. (2005).

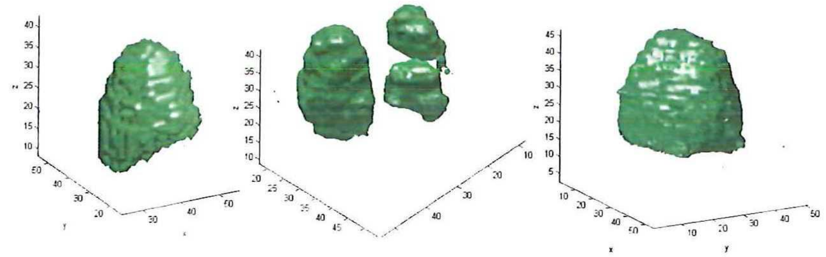

Figure 4.53: Several pseudo 3D-images of reconstructed bubbles. In the middle a group of bubbles is shown.

4.5 Wake effects

Bubbles that are close together will be influenced by each others gas flows. This can be seen by studying their speeds. Since a large database of bubbles and their properties has been built up during the measurements, these effects can be extracted from the data quite easily.
Two bubbles that follow each other are studied. Only bubble pairs that do not overlap are selected, one must clearly be the leading bubble and the other the trailing bubble. A plot of the relative speed difference between the bubbles compared to the average of both their speeds, against the time between the bubble centers, can be made. A positive relative speed is defined as the trailing bubble being faster then the leading one. If there is little time between the bubbles they should influence each other more dramatically.
A plot has been made for all bubbles that have been detected during the polystyrene distribution plate and fines measurements and do not overlap. That is a total of more than 32000 bubbles. The color of the markers is determined by the distance of the bubble centers in the xy-plane. If there is no distance between the bubbles in the xy-plane they follow each other exactly, as seen in figure 2.5(a). These points are colored blue. If the xy-distance between the bubble is big, the marker will be red. It is expected that a strong acceleration of the trailing bubble will be seen if the bubbles are vertically aligned. The results are shown in figure 4.54.

It is clear that bubbles have greater influence on each other if they are closer together. The color is nearly uniformly distributed, this means the leading bubble is roughly equally often accelerated as decelerated. The same holds for the trailing bubble. This is unexpected, since the theory by Clift and Grace states that the trailing bubble will be accelerated strongly, without influencing the leading bubble too much. Although there appears to be a stronger presence of blue in the region of a faster trailing bubble when the bubbles are close together. A similar plot is made, but now the colors are determined by the relative size difference between the bubbles. If the leading bubble is bigger, the marker will be red. If the leading bubble is smaller, the marker will be green. The plot is shown in figure 4.55. This plot shows that if the trailing bubble is larger it will also be faster than the leading bubble (green has high relative speed difference values). This is not surprising as bigger bubbles are faster in general.

These are not the results that are expected. In the plots the bubble center of gravity is used to determine the speed as well as the time between the bubbles. The leading edge of a bubble can be used as well, but this does not show the expected relation either. Looking at other properties, such as the bubble speed compared to the average bubble speed or the distance between bubbles (by taking their average speed and time between them) does not show anything similar to what would be expected. Why this is, is not clear and would require further investigation.
A more direct comparison between the Clift and Grace model and the measurement data would be interesting, but could not be done due to time constraints.

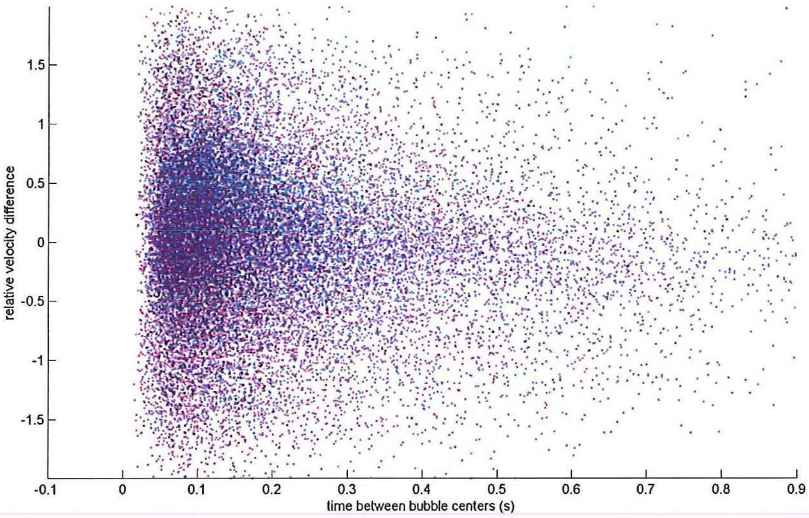

Figure 4.54: Relative bubble rise velocity (positive means trailing bubble is faster) compared to time between bubbles. Blue: xy-distance is small, red: xy-distance is big.

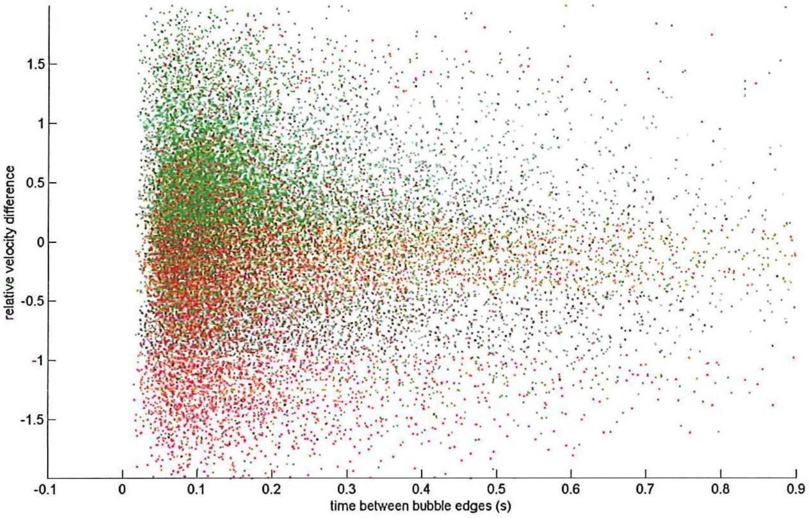

Figure 4.55: Relative bubble rise velocity (positive means trailing bubble is faster) compared to time between bubbles. Green: trailing bubble is larger, red: leading bubble is larger.

4.6 Bubble size - rise velocity relation

Using the various measurements that have been done it would be interesting to see if a relation for the bubble size and rise velocity can be verified. The rise velocity can be plotted against the spherical equivalent diameter. This is done in figure 4.56. A power fit done on the measurement data gives similar results as the Hilligardt and Werther model. Even though the fit shows a line that is somewhat like the model, the model does not give a very accurate indication of what is actually happening. There is a very large spread in the bubble size and rise velocity. All the bubbles that are plotted in the figure are detected in a single measurement run, where gas velocity, particle type and height at which the bed was studied were all kept constant. The model is only useful for calculating the mean bubble size.

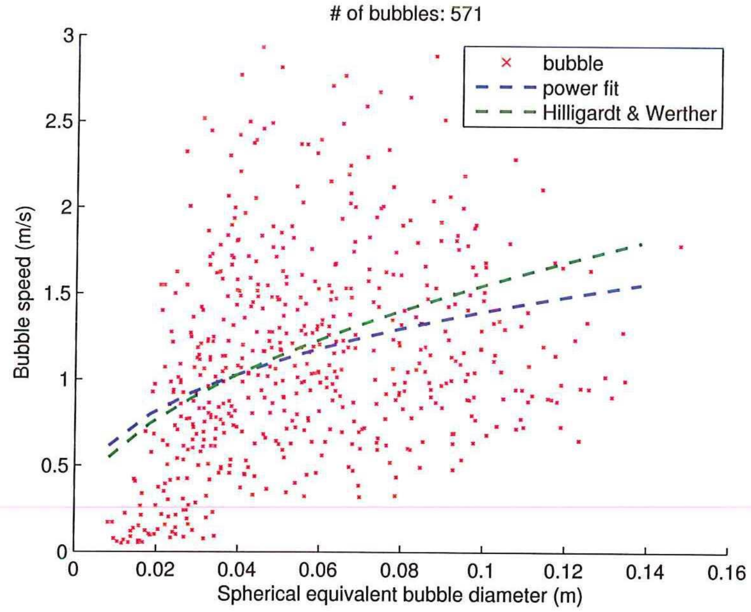

Figure 4.56: Bubble rise velocity set out agains their size for a 0% fines mixture, fluidized with a superficial gas velocity of 8 cm/s, studied at a height of 50 cm above the distribution plate. The blue line shows a power fit and the green lines is made using the Hilligardt and Werther model.

4.7 Increasing temporal resolution

For reconstructions 10 samples are averaged into 1 reconstruction. It is possible to make a reconstruction of every sample. This will make the temporal resolution 10 times higher. However, the reconstructions will be noisier. see figure 4.57. If this is done on the data recorded when the artificial bubble (124.6 cm^3) was pulled through at 1.0869 m/s we see that the detected bubble speed is 1.2153 m/s (error 12%) for the first run and 1.1981 m/s (error 10%) for the second run. The detected volume is 121.9 cm^3 (error -2%) and 115.9 cm^3 (error -7%) for the first and second run, respectively.
These values show that it is possible to use the reconstructions with a higher temporal resolution, but that they do not necessarily provide more accurate results.
The temporal resolution is 10 times higher but the required disk space and CPU time is approximately 10 times as high as well. So reconstructing large data sets at this temporal resolution is not attractive. It is possible to study a small amount of data very accurately though.

measurement	first run	error	second run	error
actual cylinder speed	1.0869 m/s	±3%	1.0869 m/s	±3%
250 Hz reconstructions	1.2206 m/s	12%	1.1749 m/s	8%
2500 Hz reconstructions	1.2153 m/s	12%	1.1981 m/s	10%
actual cylinder volume	124.6 cm^3	±3%	124.6 cm^3	±3%
250 Hz reconstructions	120 cm^3	-4%	113.6 cm^3	-9%
2500 Hz reconstructions	121.9 cm^3	-2%	115.9 cm^3	-7%

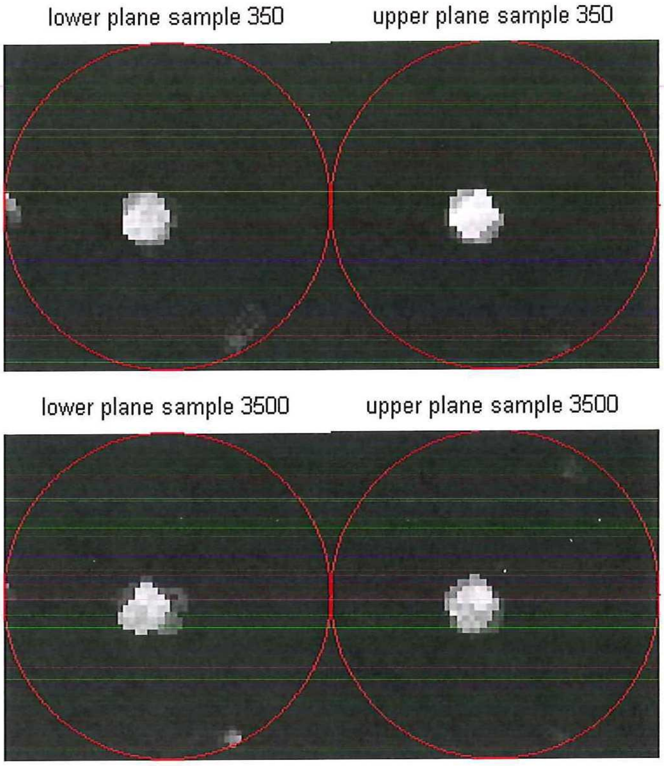

Figure 4.57: Top: reconstruction done using 10 detector samples, bottom: reconstruction using one detector sample. Data is from the second artificial bubble being pulled through the bed.

CHAPTER 5

Conclusions and recommendations

To summarize this report the most important conclusions are written down in this chapter. Recommendations are also made to improve measurement results in the future and prevent people from making the same mistakes.

5.1 Conclusions

Several conclusions can be drawn from the measurements done.

Using the X-ray setup at the Kramers Lab it is possible to detect the volume and even the shape of bubbles in a fluidized bed. Measuring for a longer period (60 seconds) makes it possible to detect many bubbles (more than 500 for fine particle beds) and get a better insight into the properties of these bubbles in a fluidized bed. Doing measurement under pressure and with particles that cause a significant amount of dust, is possible.

It has been demonstrated that an increased pressure inside the vessel that contains the fluidized bed leads to smaller bubbles. The flow of gas can be increased from 500 l/min at 1 bar_{abs} to 1700 l/min at 5 bar_{abs} before bubbles start appearing. The results show a very consistent reaction to the higher pressures; the average bubble size clearly decreases with increasing pressure at the same normal gas flow rate. It was possible to fit the detected spherical equivalent bubble diameters using the model developed by Darton et al. (1977).

The increase in fines content will lead to smaller bubbles. In the $50\%_{weight}$ fines mixture a 20% smaller bubble diameter can be seen for the higher gas velocities. This is less than has been seen by others (Beetstra et al. (2009)), and could be explained by the fact that a high threshold was needed to be able to reliably detect bubbles. The smaller bubbles might have not been detected because of this causing a bias towards larger bubbles.

Both the increase in pressure and the increase in fines content have proven to reduce the average size of the bubble in a fluidized bed at a given gas flow rate. This will improve the performance of a bed if it is used in a gas conversions process. The need for a strong vessel and filters are drawbacks, but can easily be overcome.

5.2 Recommendations

The results can be improved if the match between the calibration and the actual bed is better. This is especially seen in the measurements using the fine particles. It might be useful to try to do a calibration while the bed is minimally fluidized. Actually, just below the minimum bubble velocity would be ideal. This is difficult, because the device currently used to calibrate will sink if the bed is fluidized. Also, fine particles may cause a lot of dust, even if they are only minimally fluidized.
If calibrating in this way would be possible, a lower threshold can be used in the fine particle measurements. This will lead to a more accurate bubble size detection.
It might also be possible to do a calibration in the way that is currently done, but later adjust this using

the measurements at minimum fluidizaton or bubbling velocity. This should be explored further to improve the accuracy of the setup.
As part of this calibration, phantoms of different sizes should be use to determine the correct threshold values in a minimally fluidized bed.

When determining the true size of a bubble, not only should the size of the void in the bed be considered, but also the size of the cloud that is surrounding the void. Determining the transition from bubble void to cloud, and from cloud to bulk of the bed, especially, will be difficult to do accurately. It will be strongly dependent on the threshold choice.

The X-ray setup makes it possible to examine many properties of the bubbles. The interaction between bubble pairs is a very interesting phenomenon to study. Based on literature the trailing bubble is expected to be accelerated into the leading bubble wake, although this has not been observed clearly during this research.

When a bed of fine particles is fluidized in a closed vessel with filters installed, it is important to prevent to filters from clogging. This can be done by actively monitoring the pressure in the vessel, above the bed.

It would be interesting to do pressurized measurements using the fine particles. This would mean that the filter solution would have to be improved. Higher quality filters and multiple filter stages might be a solution. This will cause a larger pressure drop however. This filter setup must be made out of a material that can withstand the high pressures, such as steel. High quality automotive filters can stop 98% of the particles and particles as small as 5.5 μm. This makes them a simple and relatively cheap solution for this problem.

A higher spatial resolution could be achieved if the bed is studied from more angles. The current three X-ray sources give a resolution of about 4 mm per pixel. However it is still difficult to detect a bubble with a diameter smaller than 2.5 cm. Especially if this smaller bubble is accompanied by a larger bubble. The 'shadow' of the larger bubble will make reconstruction of the small one difficult. Installing more sources and detector arrays will reduce this problem and make it possible to get a higher spatial resolution. Using a similar setup but with 18 X-ray sources, a resolution of is obtained of 0.4 mm per pixel. However, this setup can study only small beds with a maximum diameter of 5 cm (Kai et al. (2005)). A higher spatial resolution will set higher requirements for the computer system used to reconstruct the system.

A higher time resolution is possible using the current setup. This will not guarantee better results, however. The amount of noise in the reconstructions is acceptable. The volume and rise velocity for faster bubbles will be reconstructed more reliably. There will be less errors due to the discretization of time. However this will also set higher requirements for the computer system.

Bibliography

A. R. Abrahamsen and D. Geldart. Behaviour of gas-fluidized beds of fine powders part i. homogeneous expansion. *Powder Technology*, 26(1):35 – 46, 1980.

S. Alenius and U. Ruotsalainen. Bayesian image reconstruction for emission tomography based on median root prior. *European Journal of Nuclear Medicine and Molecular Imaging*, 24:258–265, 1997.

J. Alles. A time-resolved x-ray computed tomography for imaging within fluidized beds. Master's thesis, Delft University of Technology, the Netherlands, 2006.

J. Alles and R. F. Mudde. Beam hardening: Analytical considerations of the effective attenuation coefficient of x-ray tomography. 34(7):2882–2889, 2007.

A. H. Andersen and A. C. Kak. Simultaneous algebraic reconstruction technique (sart): A superior implementation of the art algorithm. *Ultrasonic Imaging*, 6(1):81 – 94, 1984.

R. Beetstra, J. Nijenhuis, N. Ellis, and R. J. van Ommen. The influence of the particle size distribution on fluidized bed hydrodynamics using high-throughput experimentation. *AIChE Journal*, 55(8):2013–2023, 2009.

J. V. Briongos, S. Sanchéz-Delgado, A. Acosta-Iborra, and D. Santana. A novel approach for modeling bubbling gas solid fluidized beds. *AIChE Journal*, 57(7):1733–1750, 2011. ISSN 1547-5905.

G. Brouwer and J. van den Eijnde. *Praktische Stralingshygiëne*. Syntax Media, Arnhem, 2008. ISBN 978-90-77423-61-5.

J. Chaouki, F. Larachi, and M. P. Dudukovic. Noninvasive tomographic and velocimetric monitoring of multiphase flows. *Industrial and Engineering Chemistry Research*, 36(11):4476–4503, 1997.

R. C. Darton, R. D. LaNauze, J. F. Davidson, and D. Harrison. Bubble growth due to coalescence in fluidised beds. *Chemical Engineering Research and Design*, 55a:274–280, 1977.

J. F. Davidson. *Fluidization*. Academic Pr, 1985. ISBN 0122055527.

J. F. Davidson and D. Harrison. *Fluidised particles*. University Press, 1963. ISBN 9780608115450.

C. Dechsiri, A. Ghione, F. van de Wiel, H. G. Dehling, A. M. J. Paans, and A. C. Hoffmann. Positron emission tomography applied to fluidization engineering. *The Canadian Journal of Chemical Engineering*, 83 (1):88–96, 2005.

S. Ergun. Fluid flow through packed columns. *Chem. ENG. Prog.*, 48:89–94, 1952.

X. Fan, Z. Yang, D. J. Parker, and B. Armstrong. Prediction of bubble behaviour in fluidised beds based on solid motion and flow structure. *Chemical Engineering Journal*, 140(1-3):358 – 369, 2008.

Y. S. Fangary, M. Barigou, J. P. K. Seville, and D. J. Parker. Fluid trajectories in a stirred vessel of non-newtonian liquid using positron emission particle tracking. *Chemical Engineering Science*, 55(24):5969 – 5979, 2000.

D. Geldart. Types of gas fluidization. *Powder Technology*, 7(5):285–292, 1973.

U. Hampel, M. Speck, D. Koch, H. J. Menz, H. G. Mayer, J. Fietz, D. Hoppe, E. Schleicher, C. Zippe, and H. M. Prasser. Experimental ultra fast x-ray computed tomography with a linearly scanned electron beam source. *Flow Measurement and Instrumentation*, 16(2-3):65 – 72, 2005.

K. Hilligardt and J. Werther. Local bubble gas hold-up and expansion of gas/solid fluidized beds. *German chemical engineering*, 9(4):215–221, 1986.

A. C. Hoffmann and J. G. Yates. Experimental observations of fluidized beds at elevated pressures. *Chemical Engineering Communications*, 41(1-6):133–149, 1986.

M. Jiang and G. Wang. Convergence of the simultaneous algebraic reconstruction technique (SART). *Image Processing, IEEE Transactions on*, 12(8):957 – 961, aug. 2003.

S. Kaczmarz. Angenaherte auflosung von systemen linearer gleichungen. *Bulletin International de l'Academie Polonaise des Sciences et des Lettres. Serie A*, 35:355 – 357, 1937.

T. Kai, M. Misawa, T. Takahashi, I. Tiseanu, and N. Ichikawai. Observation of 3-d structure of bubbles in a fluidized catalyst bed. *The Canadian Journal of Chemical Engineering*, 83(1):113–118, 2005.

A. C. Kak and M. Slaney. *Principles of Computerized Tomographic Imaging*. I.E.E.E.Press, 1989. ISBN 0879421983.

J. Kawabata, M. Yumiyama, Y. Tazaki, S. Honma, T. Chiba, T. Sumiya, and K. Endo. Characteristics of gas-fluidised beds under pressure. *Journal of Chemical Engineering of Japan*, 14(2):85–89, 1981.

R. Krishna. Simulation of an industrial fluidized bed reactor using a bubble growth model. *Chemical Engineering Research and Design*, 66a:463–469, 1988.

D. Kunii and O. Levenspiel. *Fluidization Engineering, Second Edition (Butterworths Series in Chemical Engineering)*. Butterworth-Heinemann, 1991. ISBN 0409902330.

S. Mori and C. Y. Wen. Estimation of bubble diameter in gaseous fluidized beds. *AIChE Journal*, 21(1): 109–115, 1975.

R. F. Mudde. Bubbles in a fluidized bed: A fast x-ray scanner. *AIChE Journal*, 57(10):2684–2690, 2011.

R. F. Mudde, Q. Ricoux, E. C. Wagner, and J. R. van Ommen. Time-resolved x-ray tomography of a fluidized bed of geldart a particles. 2010.

R.F. Mudde, J. Alles, and T. H. J. J. van der Hagen. Feasibility study of a time-resolving x-ray tomographic system. *Measurement Science and Technology*, 19(8):085501, 2008.

R. A. Novelline. *Squire's Fundamentals of Radiology*. Harvard University Press, 1997. ISBN 0674833392.

P. A. Olowson and A. E. Almstedt. Influence of pressure on the minimum fluidization velocity. *Chemical Engineering Science*, 46(2):637 – 640, 1991.

P. N. Rowe. Experimental properties of bubbles. *Fluidization*, pages 121–191, 1971.

P.N. Rowe. Prediction of bubble size in a gas fluidised bed. *Chemical Engineering Science*, 31(4):285 – 288, 1976.

L. G. Shapiro and Stockman. G. C. *Computer Vision*. Prentice Hall, 2001. ISBN 0130307963.

P. S. B. Stewart and J. F. Davidson. Slug flow in fluidised beds. *Powder Technology*, 1(2):61 – 80, 1967.

F. I. H. Verhaart. A time-resolved x-ray computed tomography for imaging within fluidized beds. Master's thesis, Delft University of Technology, the Netherlands, 2007.

E. C. Wagner. Safety report: X-ray tomography scanner. Technical report, Delft University of Technology, 2011.

G. B. Wallis. *One-Dimensional Two-Phase Flow*. McGraw-Hill, 1969.

W. Warsito and L. S. Fan. Neural network based multi-criterion optimization image reconstruction technique for imaging two- and three-phase flow systems using electrical capacitance tomography. *Measurement Science and Technology*, 12(12):2198, 2001.

A. W. Weimer and G. J. Quarderer. On dense phase voidage and bubble size in high pressure fluidized beds of fine powders. *AIChE Journal*, 31(6):1019–1028, 1985.

J. Werther. Die bedeutung der blasenkoaleszenz für die auslegung von gas/feststoff-wirbelschichten. *Chemie Ingenieur Technik*, 48(4):339–339, 1976.

APPENDIX A

Spherical equivalent diameter plots for pressure

A.1 Distribution plate, at fixed height

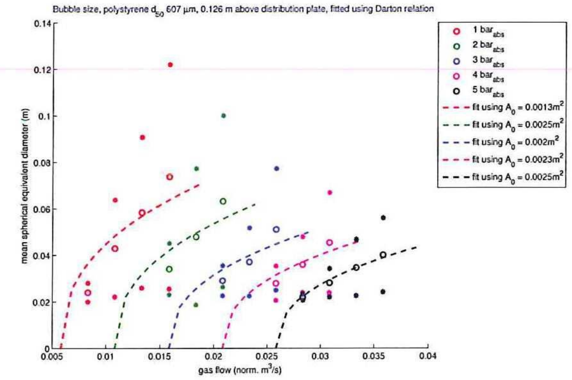

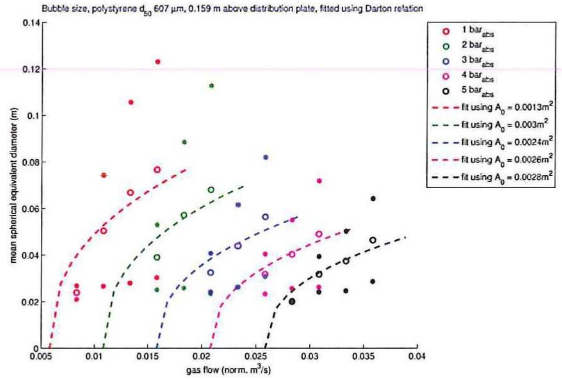

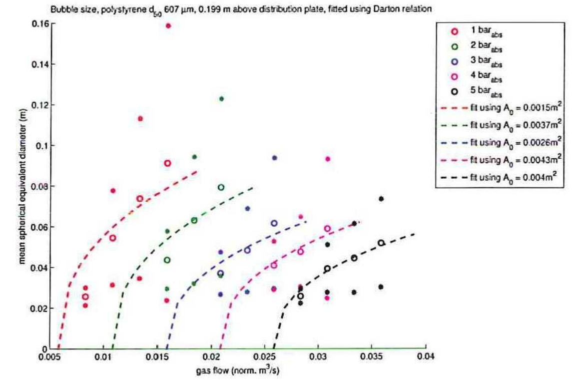

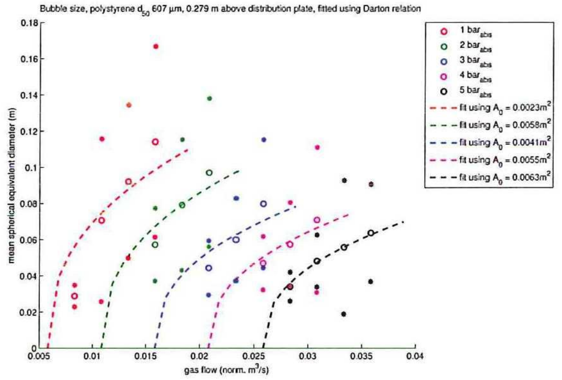

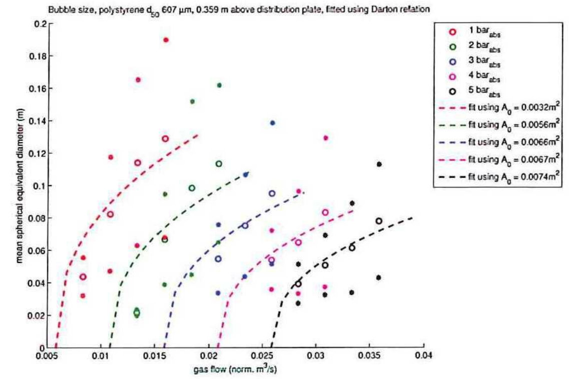

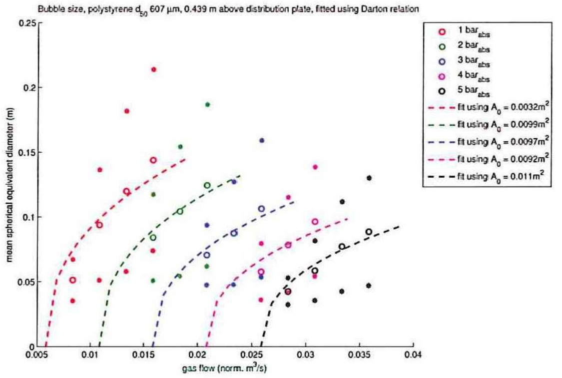

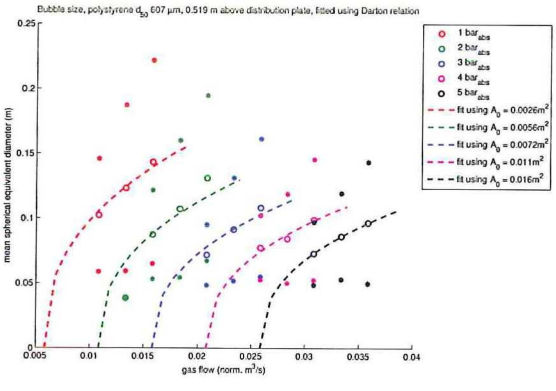
Bubble size, polystyrene d_{50} 607 µm, 0.519 m above distribution plate, fitted using Darton relation
mean spherical equivalent diameter (m)
0
0.05
0.1
0.15
0.2
0.25
gas flow (norm. m^3/s)
0.005
0.01
0.015
0.02
0.025
0.03
0.035
0.04
1 bar_{abs}
2 bar_{abs}
3 bar_{abs}
4 bar_{abs}
5 bar_{abs}
fit using A_0 = 0.0026m^2
fit using A_0 = 0.0056m^2
fit using A_0 = 0.0072m^2
fit using A_0 = 0.011m^2
fit using A_0 = 0.016m^2

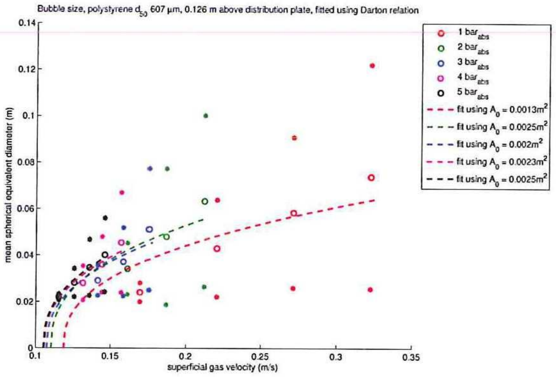
Bubble size, polystyrene d_{50} 607 µm, 0.126 m above distribution plate, fitted using Darton relation
mean spherical equivalent diameter (m)
0
0.02
0.04
0.06
0.08
0.1
0.12
0.14
superficial gas velocity (m/s)
0.1
0.15
0.2
0.25
0.3
0.35
1 bar_{abs}
2 bar_{abs}
3 bar_{abs}
4 bar_{abs}
5 bar_{abs}
fit using A_0 = 0.0013m^2
fit using A_0 = 0.0025m^2
fit using A_0 = 0.002m^2
fit using A_0 = 0.0023m^2
fit using A_0 = 0.0025m^2

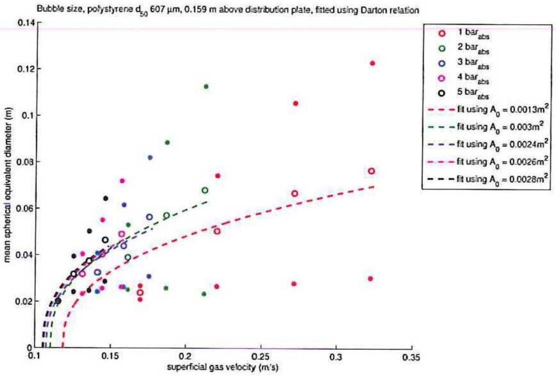
Bubble size, polystyrene d_{50} 607 µm, 0.159 m above distribution plate, fitted using Darton relation
mean spherical equivalent diameter (m)
0
0.02
0.04
0.06
0.08
0.1
0.12
0.14
superficial gas velocity (m/s)
0.1
0.15
0.2
0.25
0.3
0.35
1 bar_{abs}
2 bar_{abs}
3 bar_{abs}
4 bar_{abs}
5 bar_{abs}
fit using A_0 = 0.0013m^2
fit using A_0 = 0.003m^2
fit using A_0 = 0.0024m^2
fit using A_0 = 0.0026m^2
fit using A_0 = 0.0028m^2

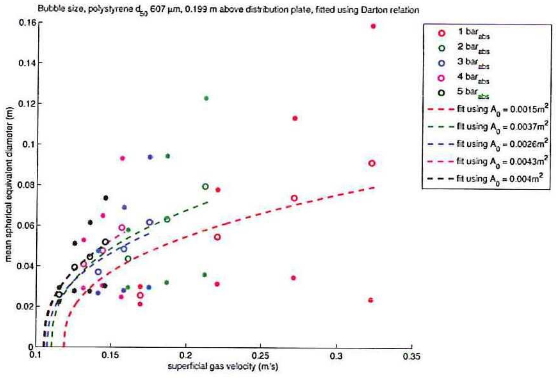
Bubble size, polystyrene d_{50} 607 µm, 0.199 m above distribution plate, fitted using Darton relation
mean spherical equivalent diameter (m)
0
0.02
0.04
0.06
0.08
0.1
0.12
0.14
0.16
superficial gas velocity (m/s)
0.1
0.15
0.2
0.25
0.3
0.35
1 bar_{abs}
2 bar_{abs}
3 bar_{abs}
4 bar_{abs}
5 bar_{abs}
fit using A_0 = 0.0015m^2
fit using A_0 = 0.0037m^2
fit using A_0 = 0.0026m^2
fit using A_0 = 0.0043m^2
fit using A_0 = 0.004m^2

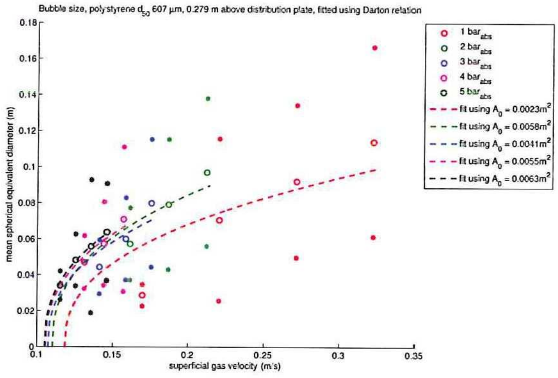
Bubble size, polystyrene d_{50} 607 µm, 0.279 m above distribution plate, fitted using Darton relation
mean spherical equivalent diameter (m)
0
0.02
0.04
0.06
0.08
0.1
0.12
0.14
0.16
0.18
superficial gas velocity (m/s)
0.1
0.15
0.2
0.25
0.3
0.35
1 bar_{abs}
2 bar_{abs}
3 bar_{abs}
4 bar_{abs}
5 bar_{abs}
fit using A_0 = 0.0023m^2
fit using A_0 = 0.0058m^2
fit using A_0 = 0.0041m^2
fit using A_0 = 0.0055m^2
fit using A_0 = 0.0063m^2

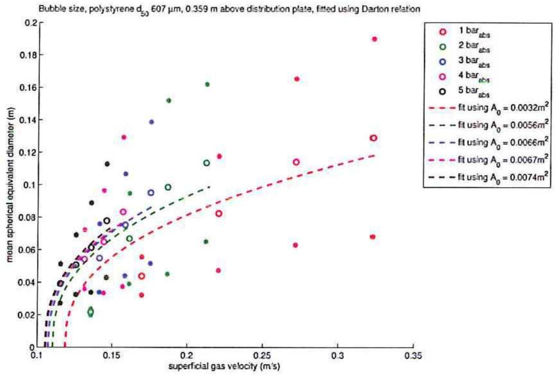
Bubble size, polystyrene d_{50} 607 µm, 0.359 m above distribution plate, fitted using Darton relation
mean spherical equivalent diameter (m)
superficial gas velocity (m/s)
0
0.02
0.04
0.06
0.08
0.1
0.12
0.14
0.16
0.18
0.2
0.1
0.15
0.2
0.25
0.3
0.35
1 bar_{abs}
2 bar_{abs}
3 bar_{abs}
4 bar_{abs}
5 bar_{abs}
fit using $A_0 = 0.0032 m^2$
fit using $A_0 = 0.0056 m^2$
fit using $A_0 = 0.0066 m^2$
fit using $A_0 = 0.0067 m^2$
fit using $A_0 = 0.0074 m^2$

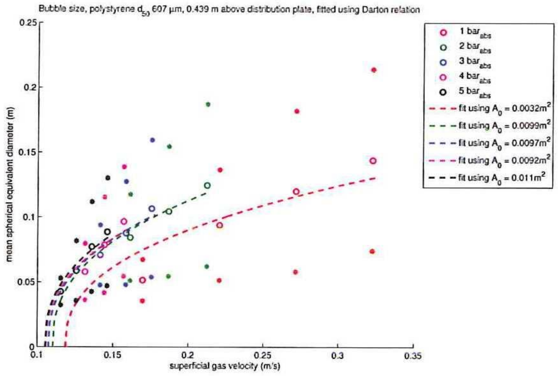
Bubble size, polystyrene d_{50} 607 µm, 0.439 m above distribution plate, fitted using Darton relation
mean spherical equivalent diameter (m)
superficial gas velocity (m/s)
0
0.05
0.1
0.15
0.2
0.25
0.1
0.15
0.2
0.25
0.3
0.35
1 bar_{abs}
2 bar_{abs}
3 bar_{abs}
4 bar_{abs}
5 bar_{abs}
fit using $A_0 = 0.0032 m^2$
fit using $A_0 = 0.0099 m^2$
fit using $A_0 = 0.0097 m^2$
fit using $A_0 = 0.0092 m^2$
fit using $A_0 = 0.011 m^2$

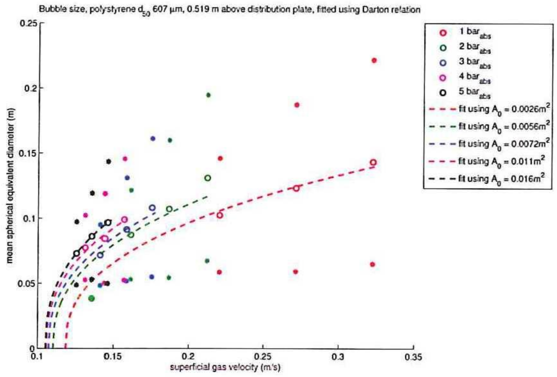
Bubble size, polystyrene d_{50} 607 µm, 0.519 m above distribution plate, fitted using Darton relation
mean spherical equivalent diameter (m)
superficial gas velocity (m/s)
0
0.05
0.1
0.15
0.2
0.25
0.1
0.15
0.2
0.25
0.3
0.35
1 bar_{abs}
2 bar_{abs}
3 bar_{abs}
4 bar_{abs}
5 bar_{abs}
fit using $A_0 = 0.0026 m^2$
fit using $A_0 = 0.0056 m^2$
fit using $A_0 = 0.0072 m^2$
fit using $A_0 = 0.011 m^2$
fit using $A_0 = 0.016 m^2$

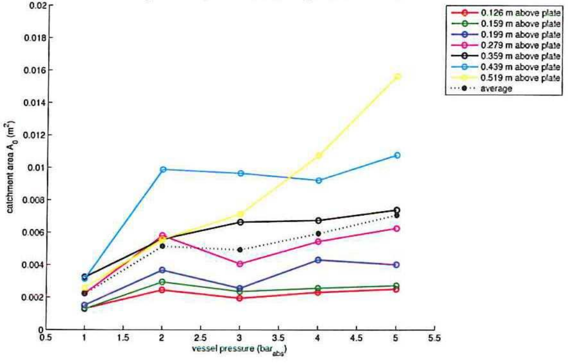
Catchment area A_0 from fits using Darton for polystyrene d_{50} 607 µm, distribution plate
catchment area A_0 (m^2)
vessel pressure (bar_{abs})
0
0.002
0.004
0.006
0.008
0.01
0.012
0.014
0.016
0.018
0.02
0.5
1
1.5
2
2.5
3
3.5
4
4.5
5
5.5
0.126 m above plate
0.159 m above plate
0.199 m above plate
0.279 m above plate
0.359 m above plate
0.439 m above plate
0.519 m above plate
average

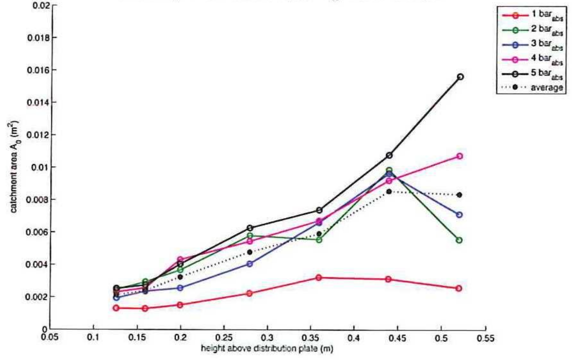
Catchment area A_0 from fits using Darton for polystyrene d_{50} 607 µm, distribution plate
catchment area A_0 (m^2)
height above distribution plate (m)
0
0.002
0.004
0.006
0.008
0.01
0.012
0.014
0.016
0.018
0.02
0.05
0.1
0.15
0.2
0.25
0.3
0.35
0.4
0.45
0.5
0.55
1 bar_{abs}
2 bar_{abs}
3 bar_{abs}
4 bar_{abs}
5 bar_{abs}
average

A.2 Distribution plate, at fixed pressure

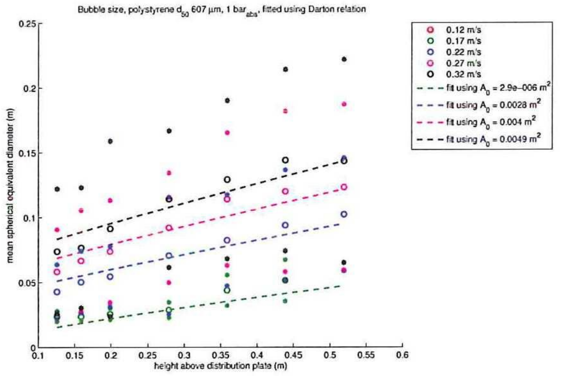

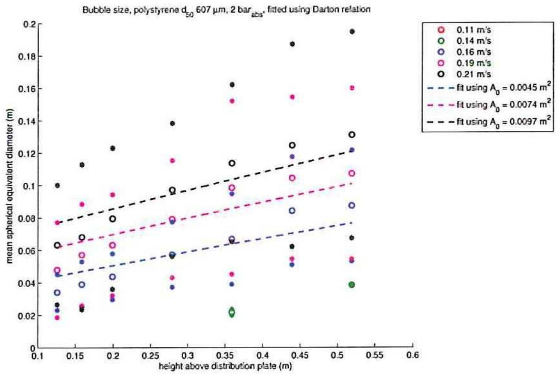

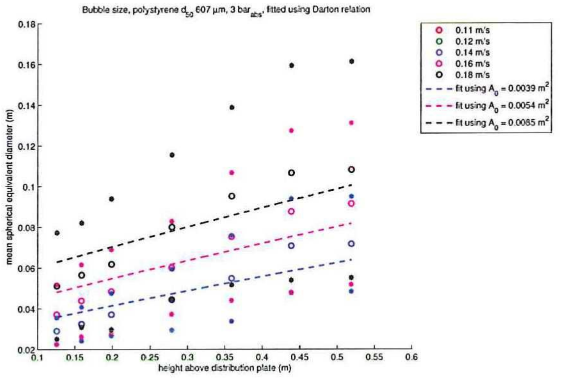

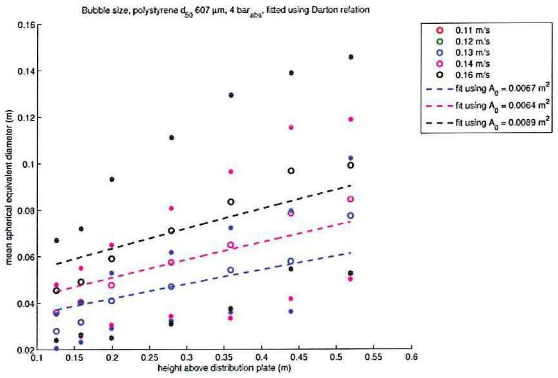

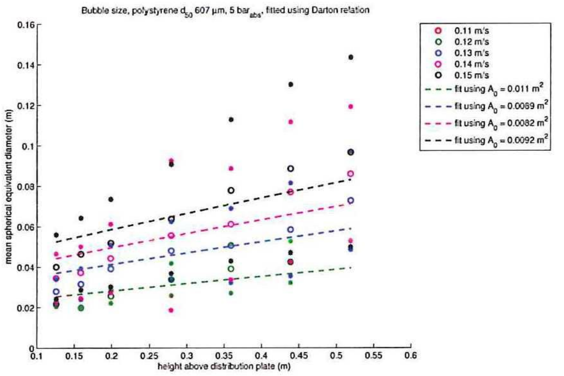

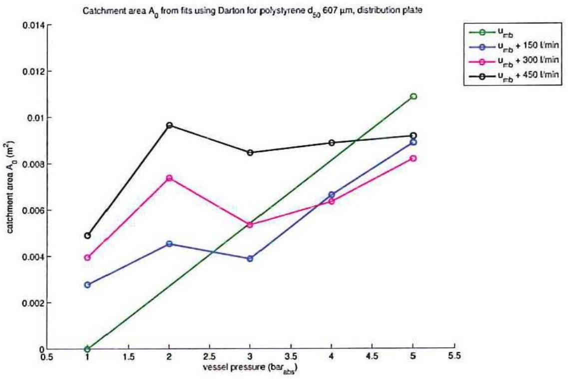

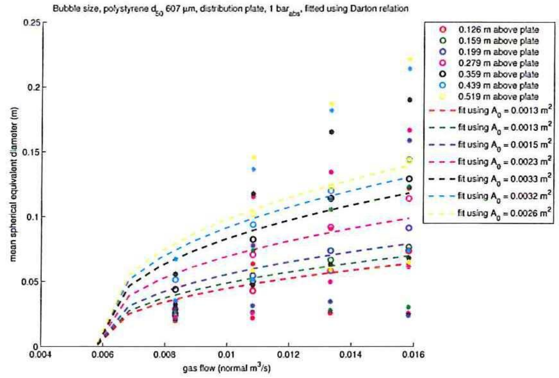
Bubble size, polystyrene d_{50} 607 µm, distribution plate, 1 bar$_{abs}$, fitted using Darton relation

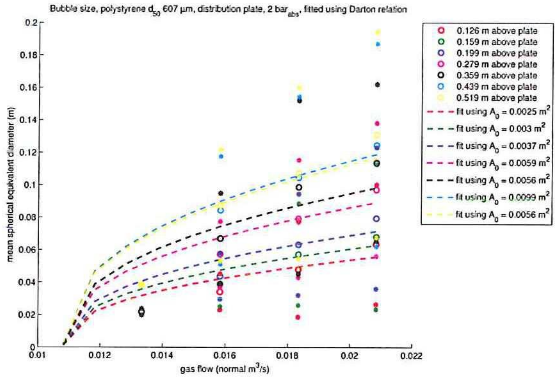
Bubble size, polystyrene d_{50} 607 µm, distribution plate, 2 bar$_{abs}$, fitted using Darton relation

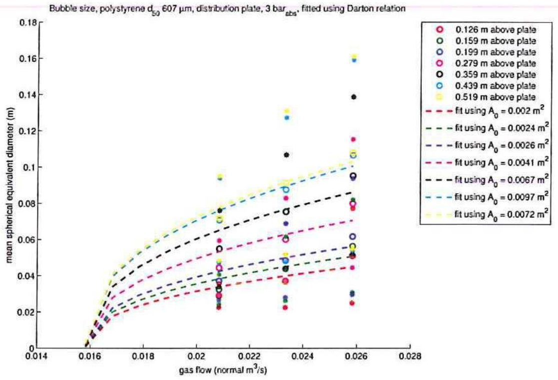
Bubble size, polystyrene d_{50} 607 µm, distribution plate, 3 bar$_{abs}$, fitted using Darton relation

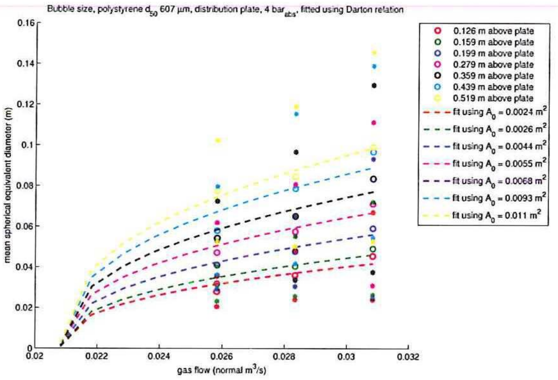
Bubble size, polystyrene d_{50} 607 µm, distribution plate, 4 bar$_{abs}$, fitted using Darton relation

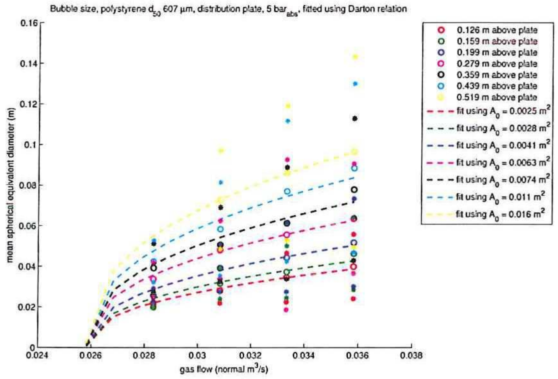
Bubble size, polystyrene d_{50} 607 µm, distribution plate, 5 bar$_{abs}$, fitted using Darton relation

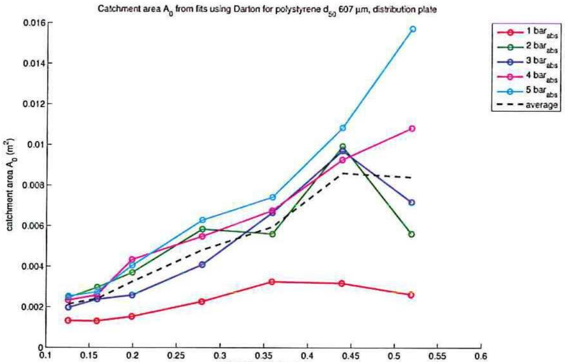
Catchment area A_0 from fits using Darton for polystyrene d_{50} 607 µm, distribution plate

A.3 Distribution plate, at fixed flow

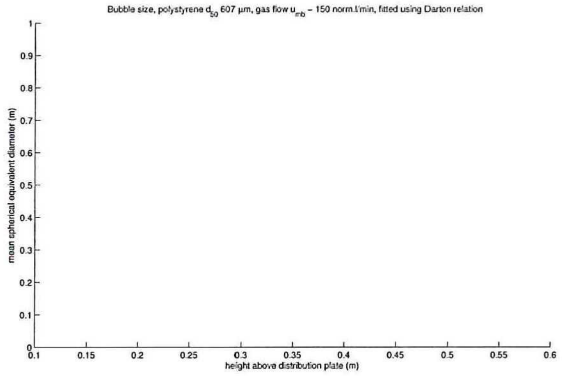

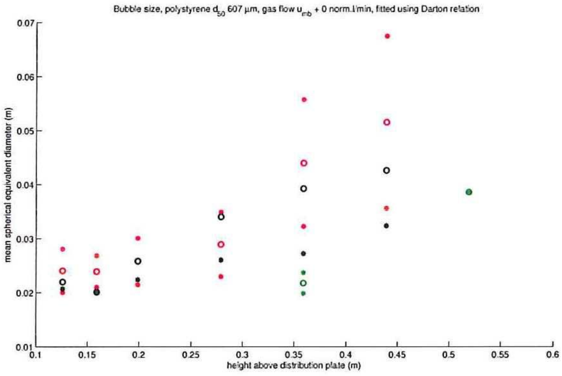

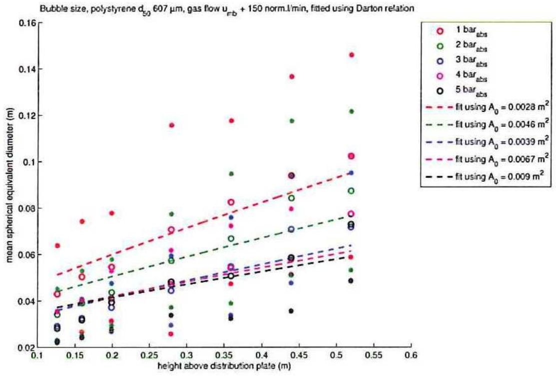

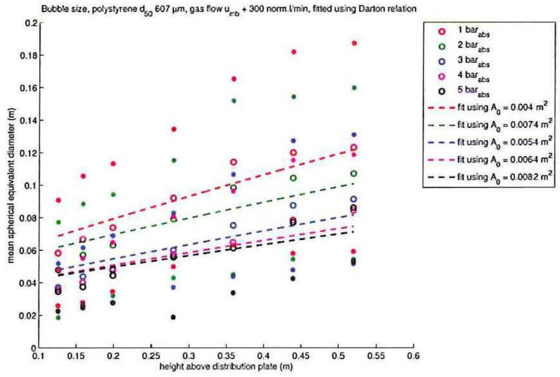

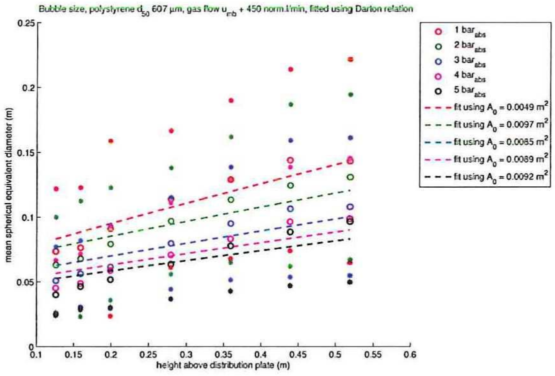

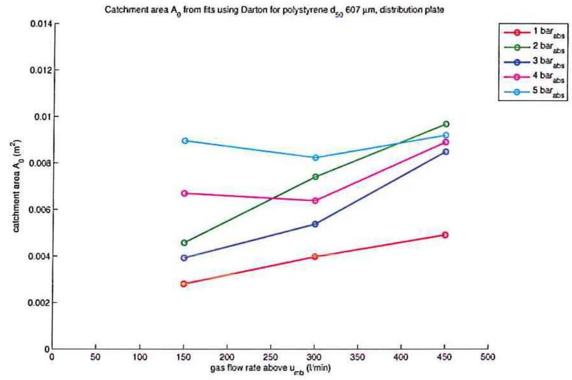
Catchment area A_0 from fits using Darton for polystyrene d_{50} 607 µm, distribution plate
1 bar_{abs}
2 bar_{abs}
3 bar_{abs}
4 bar_{abs}
5 bar_{abs}
catchment area A_0 (m^2)
0.014
0.012
0.01
0.008
0.006
0.004
0.002
0
0
50
100
150
200
250
300
350
400
450
500
gas flow rate above u_{mb} (l/min)

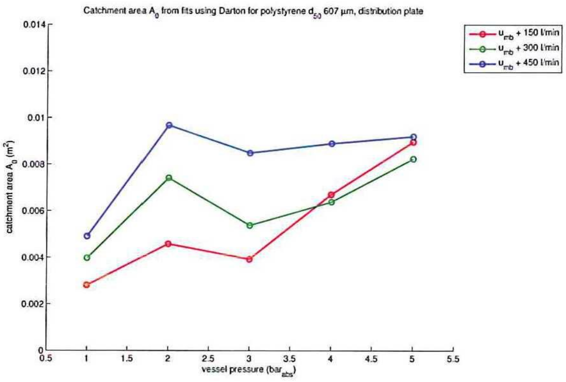
Catchment area A_0 from fits using Darton for polystyrene d_{50} 607 µm, distribution plate
u_{mb} + 150 l/min
u_{mb} + 300 l/min
u_{mb} + 450 l/min
catchment area A_0 (m^2)
0.014
0.012
0.01
0.008
0.006
0.004
0.002
0
0.5
1
1.5
2
2.5
3
3.5
4
4.5
5
5.5
vessel pressure (bar_{abs})

A.4 Single jet, at fixed height

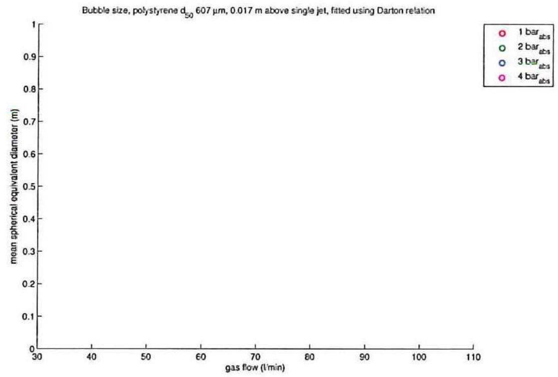

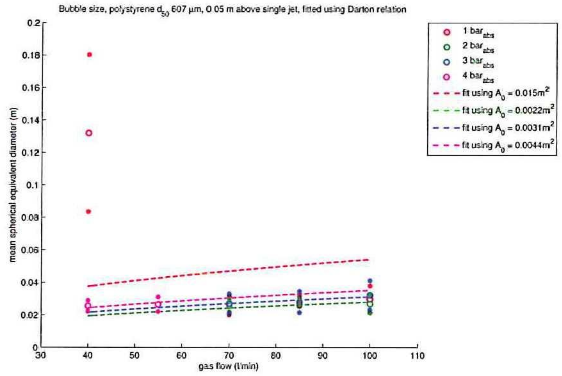

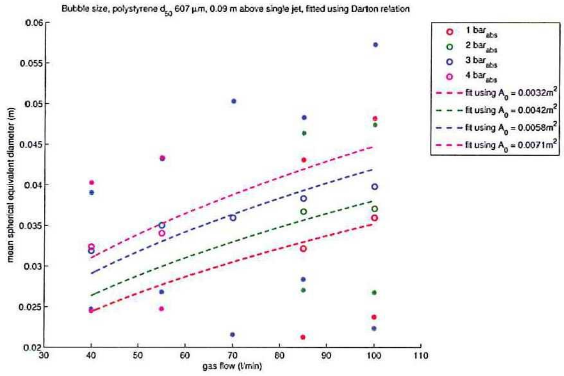

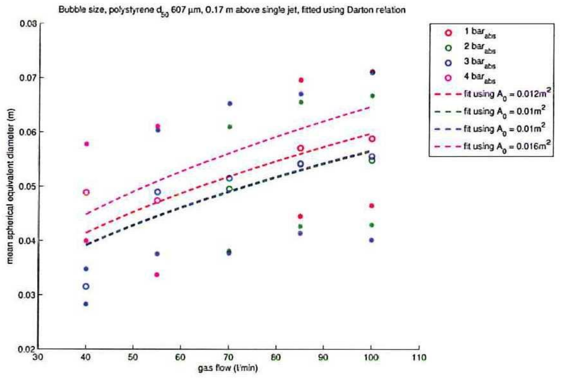

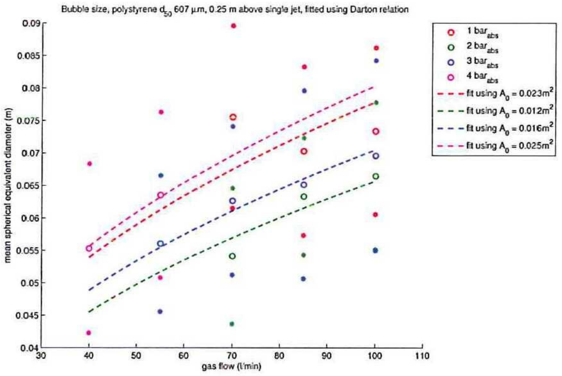

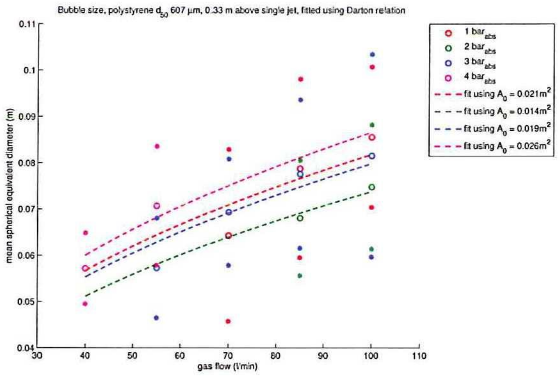

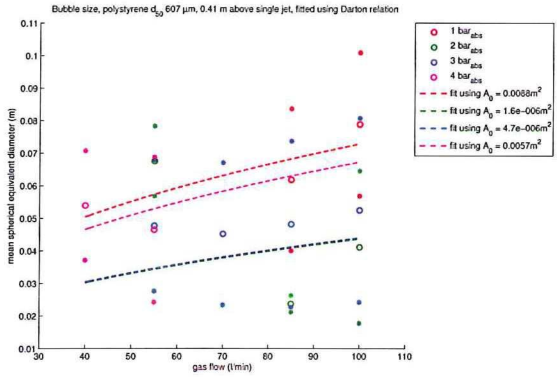
Bubble size, polystyrene d50 607 µm, 0.41 m above single jet, fitted using Darton relation
mean spherical equivalent diameter (m)
gas flow (l/min)
0.11
0.1
0.09
0.08
0.07
0.06
0.05
0.04
0.03
0.02
0.01
30
40
50
60
70
80
90
100
110
1 bar abs
2 bar abs
3 bar abs
4 bar abs
fit using A0 = 0.0088m2
fit using A0 = 1.6e-006m2
fit using A0 = 4.7e-006m2
fit using A0 = 0.0057m2

A.5 Single jet, at fixed pressure

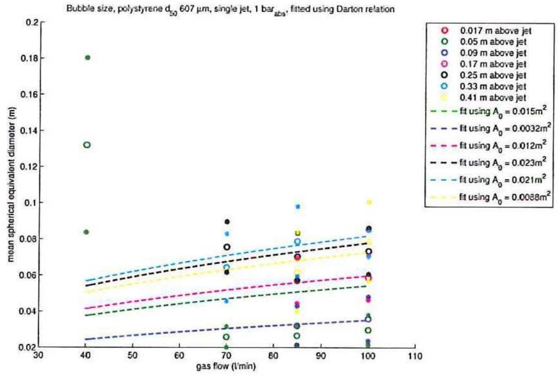

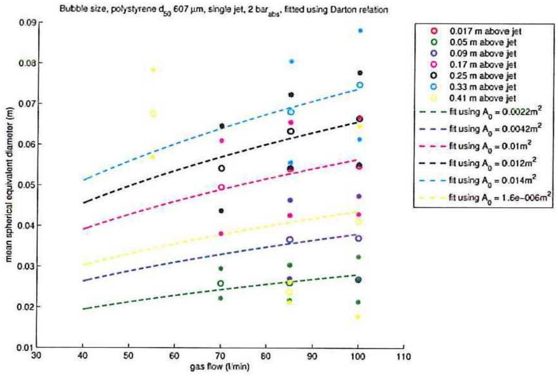

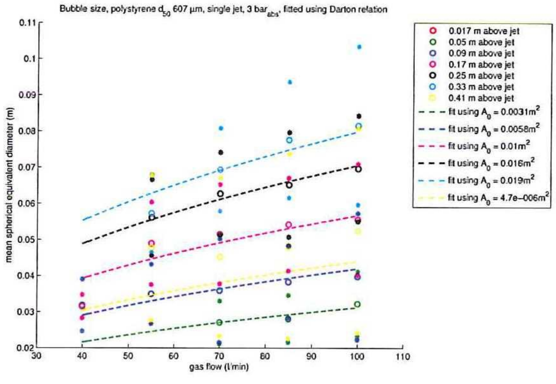

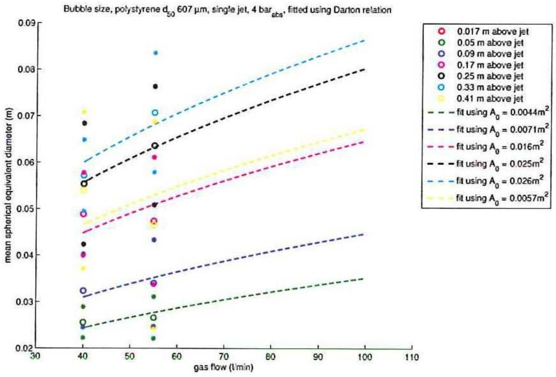

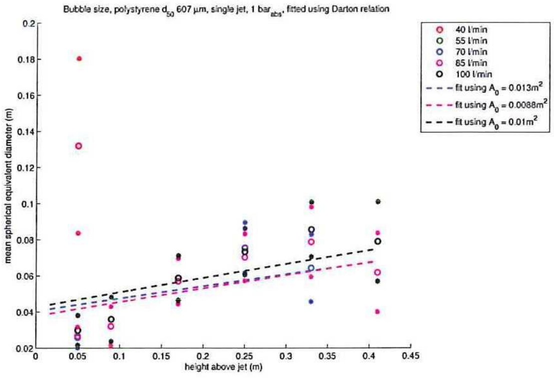
Bubble size, polystyrene d_{50} 607 μm, single jet, 1 bar_{abs}, fitted using Darton relation

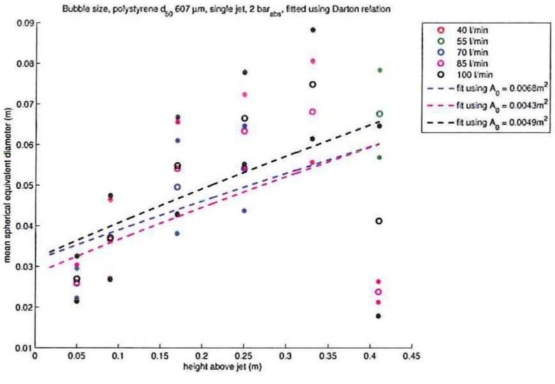
Bubble size, polystyrene d_{50} 607 μm, single jet, 2 bar_{abs}, fitted using Darton relation

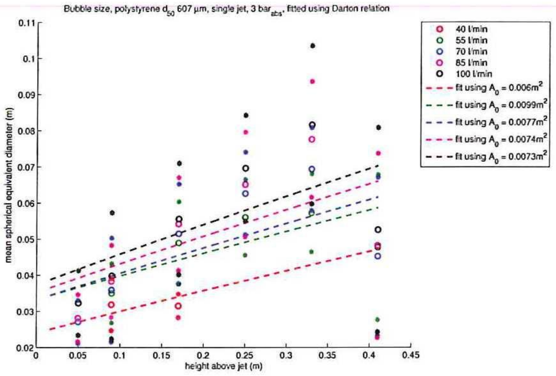
Bubble size, polystyrene d_{50} 607 μm, single jet, 3 bar_{abs}, fitted using Darton relation

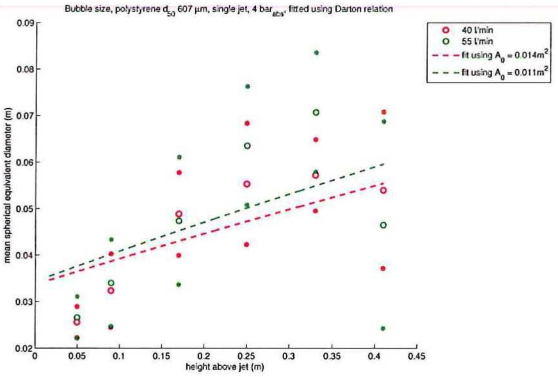
Bubble size, polystyrene d_{50} 607 μm, single jet, 4 bar_{abs}, fitted using Darton relation

A.6 Single jet, at fixed flow

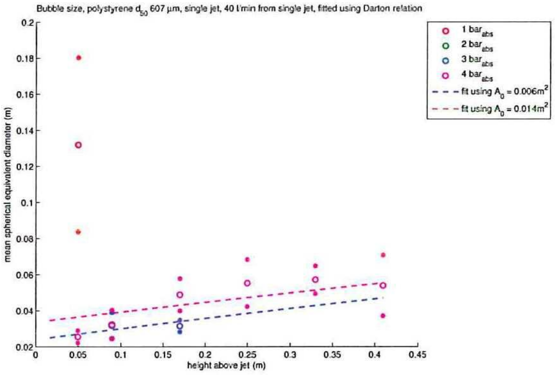

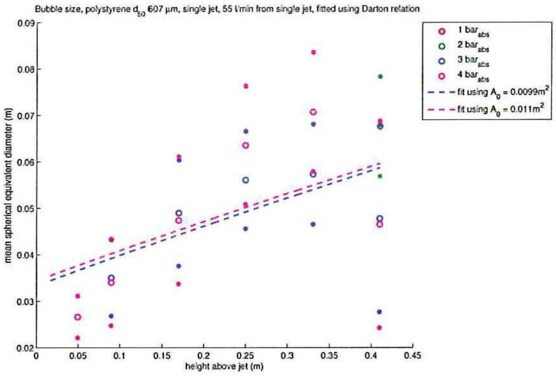

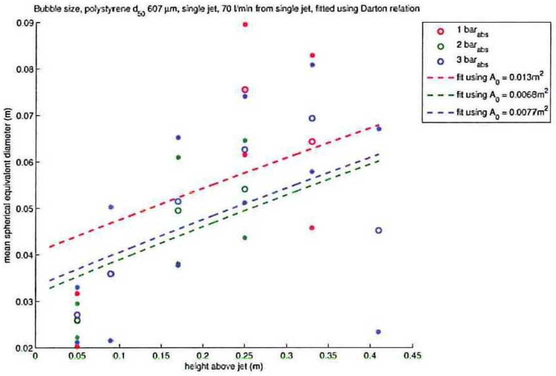

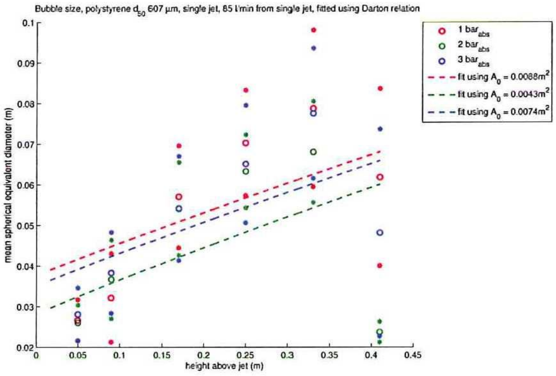

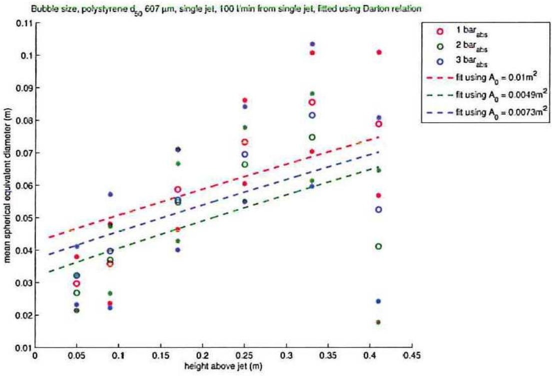

APPENDIX B

Rise velocity plots for pressure

B.1 Distribution plate, at fixed height

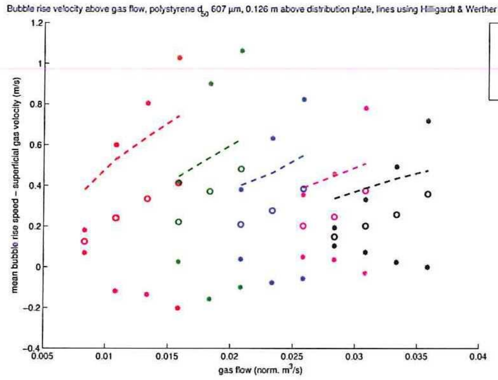

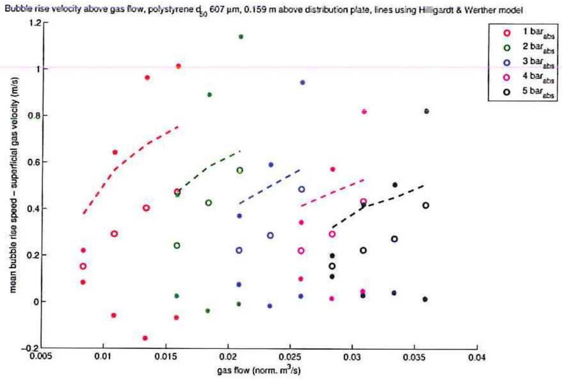

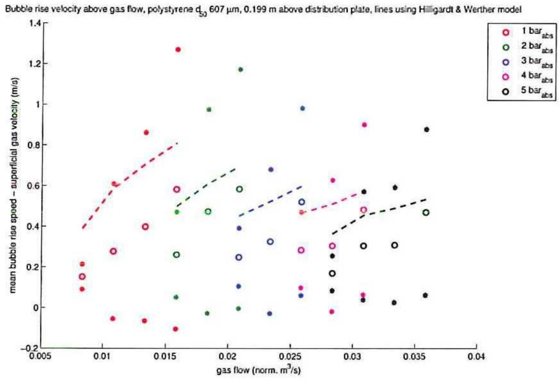

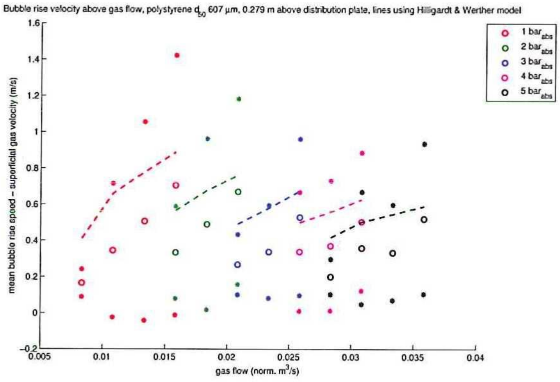

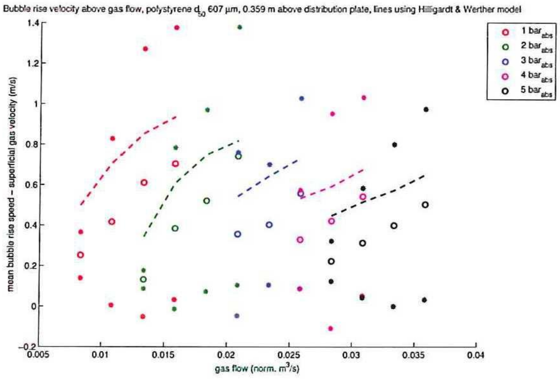

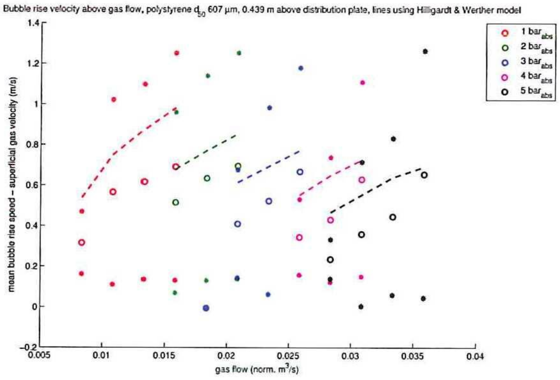

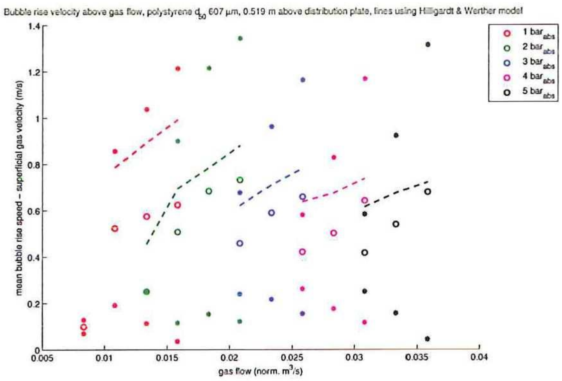
Bubble rise velocity above gas flow, polystyrene d50 607 μm, 0.519 m above distribution plate, lines using Hilligardt & Werther model
mean bubble rise speed − superficial gas velocity (m/s)
gas flow (norm. m³/s)
1 bar abs
2 bar abs
3 bar abs
4 bar abs
5 bar abs

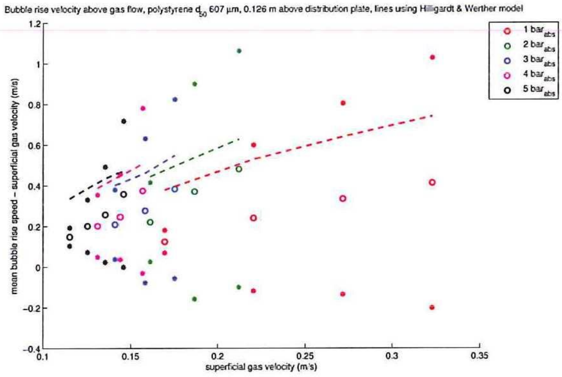
Bubble rise velocity above gas flow, polystyrene d50 607 μm, 0.126 m above distribution plate, lines using Hilligardt & Werther model
mean bubble rise speed − superficial gas velocity (m/s)
superficial gas velocity (m/s)
1 bar abs
2 bar abs
3 bar abs
4 bar abs
5 bar abs

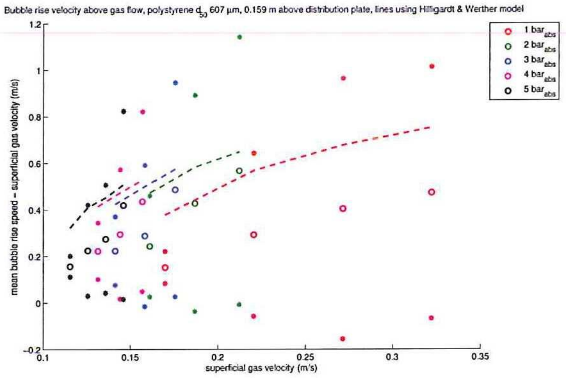
Bubble rise velocity above gas flow, polystyrene d50 607 μm, 0.159 m above distribution plate, lines using Hilligardt & Werther model
mean bubble rise speed − superficial gas velocity (m/s)
superficial gas velocity (m/s)
1 bar abs
2 bar abs
3 bar abs
4 bar abs
5 bar abs

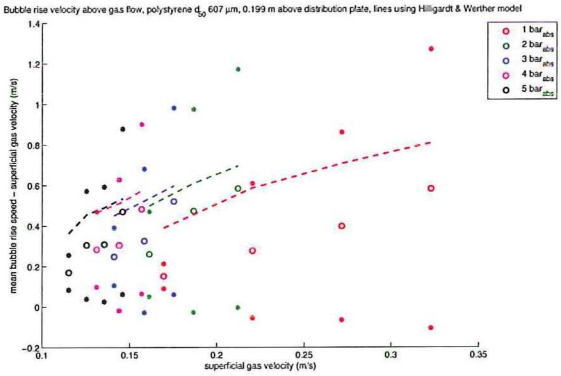
Bubble rise velocity above gas flow, polystyrene d50 607 μm, 0.199 m above distribution plate, lines using Hilligardt & Werther model
mean bubble rise speed − superficial gas velocity (m/s)
superficial gas velocity (m/s)
1 bar abs
2 bar abs
3 bar abs
4 bar abs
5 bar abs

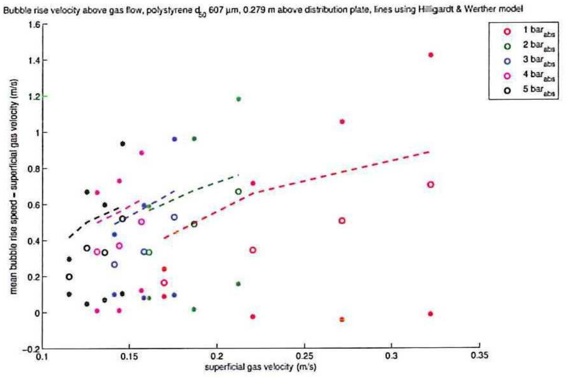
Bubble rise velocity above gas flow, polystyrene d50 607 μm, 0.279 m above distribution plate, lines using Hilligardt & Werther model
mean bubble rise speed − superficial gas velocity (m/s)
superficial gas velocity (m/s)
1 bar abs
2 bar abs
3 bar abs
4 bar abs
5 bar abs

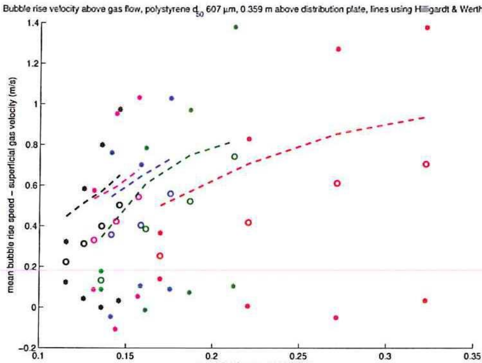
Bubble rise velocity above gas flow, polystyrene d_{50} 607 µm, 0.359 m above distribution plate, lines using Hilligardt & Werther model
mean bubble rise speed – superficial gas velocity (m/s)
superficial gas velocity (m/s)
1.4
1.2
1
0.8
0.6
0.4
0.2
0
−0.2
0.1
0.15
0.2
0.25
0.3
0.35
1 bar_{abs}
2 bar_{abs}
3 bar_{abs}
4 bar_{abs}
5 bar_{abs}

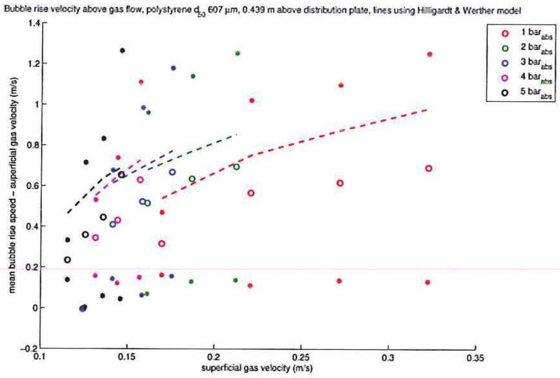
Bubble rise velocity above gas flow, polystyrene d_{50} 607 µm, 0.439 m above distribution plate, lines using Hilligardt & Werther model
mean bubble rise speed – superficial gas velocity (m/s)
superficial gas velocity (m/s)
1.4
1.2
1
0.8
0.6
0.4
0.2
0
−0.2
0.1
0.15
0.2
0.25
0.3
0.35
1 bar_{abs}
2 bar_{abs}
3 bar_{abs}
4 bar_{abs}
5 bar_{abs}

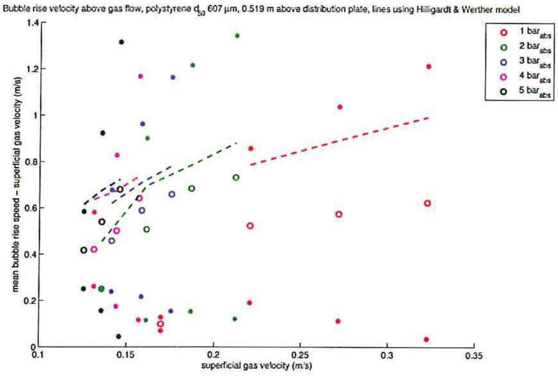
Bubble rise velocity above gas flow, polystyrene d_{50} 607 µm, 0.519 m above distribution plate, lines using Hilligardt & Werther model
mean bubble rise speed – superficial gas velocity (m/s)
superficial gas velocity (m/s)
1.4
1.2
1
0.8
0.6
0.4
0.2
0
0.1
0.15
0.2
0.25
0.3
0.35
1 bar_{abs}
2 bar_{abs}
3 bar_{abs}
4 bar_{abs}
5 bar_{abs}

B.2 Distribution plate, at fixed pressure

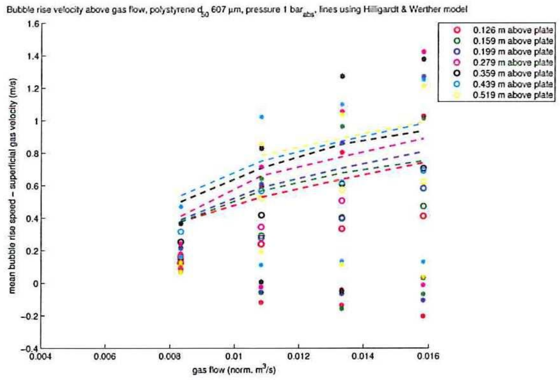

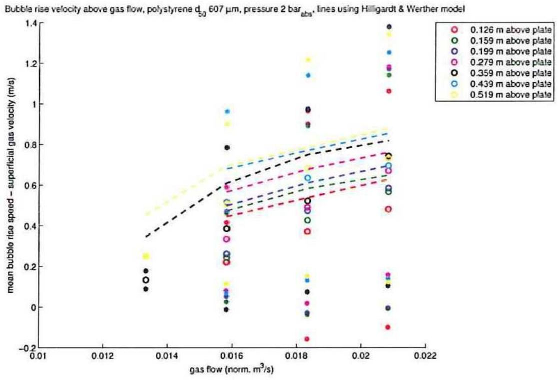

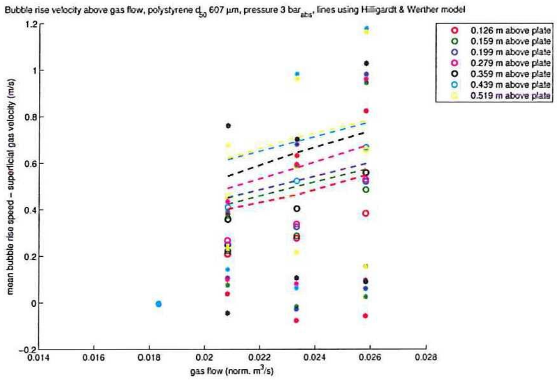

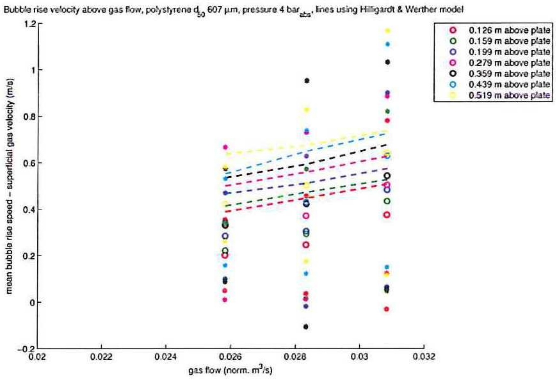

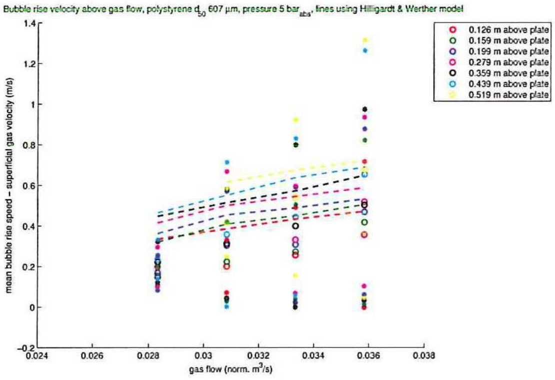

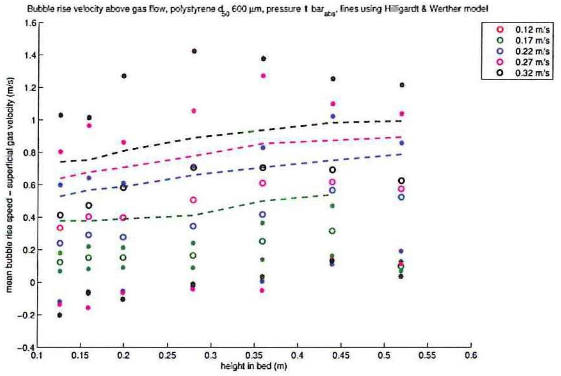
Bubble rise velocity above gas flow, polystyrene d_{50} 600 µm, pressure 1 bar_{abs}, lines using Hilligardt & Werther model
mean bubble rise speed – superficial gas velocity (m/s)
height in bed (m)
0.12 m/s
0.17 m/s
0.22 m/s
0.27 m/s
0.32 m/s
-0.4
-0.2
0
0.2
0.4
0.6
0.8
1
1.2
1.4
1.6
0.1
0.15
0.2
0.25
0.3
0.35
0.4
0.45
0.5
0.55
0.6

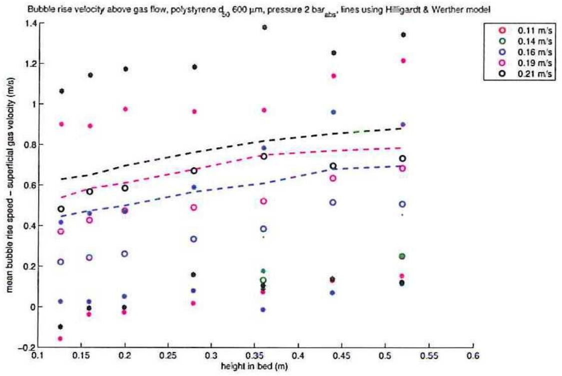
Bubble rise velocity above gas flow, polystyrene d_{50} 600 µm, pressure 2 bar_{abs}, lines using Hilligardt & Werther model
mean bubble rise speed – superficial gas velocity (m/s)
height in bed (m)
0.11 m/s
0.14 m/s
0.16 m/s
0.19 m/s
0.21 m/s
-0.2
0
0.2
0.4
0.6
0.8
1
1.2
1.4
0.1
0.15
0.2
0.25
0.3
0.35
0.4
0.45
0.5
0.55
0.6

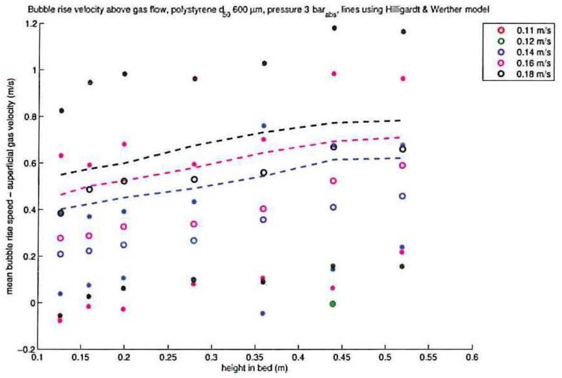
Bubble rise velocity above gas flow, polystyrene d_{50} 600 µm, pressure 3 bar_{abs}, lines using Hilligardt & Werther model
mean bubble rise speed – superficial gas velocity (m/s)
height in bed (m)
0.11 m/s
0.12 m/s
0.14 m/s
0.16 m/s
0.18 m/s
-0.2
0
0.2
0.4
0.6
0.8
1
1.2
0.1
0.15
0.2
0.25
0.3
0.35
0.4
0.45
0.5
0.55
0.6

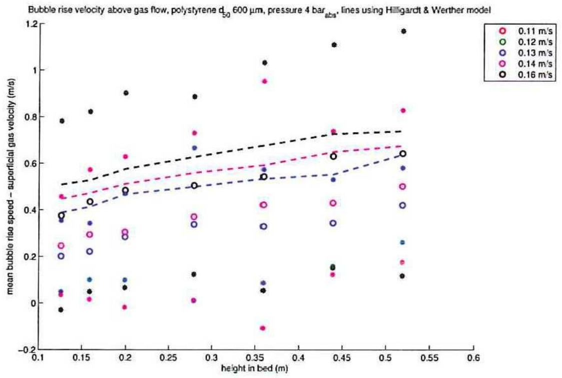
Bubble rise velocity above gas flow, polystyrene d_{50} 600 µm, pressure 4 bar_{abs}, lines using Hilligardt & Werther model
mean bubble rise speed – superficial gas velocity (m/s)
height in bed (m)
0.11 m/s
0.12 m/s
0.13 m/s
0.14 m/s
0.16 m/s
-0.2
0
0.2
0.4
0.6
0.8
1
1.2
0.1
0.15
0.2
0.25
0.3
0.35
0.4
0.45
0.5
0.55
0.6

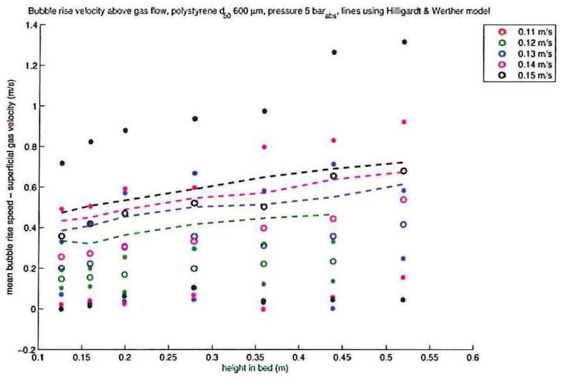
Bubble rise velocity above gas flow, polystyrene d_{50} 600 µm, pressure 5 bar_{abs}, lines using Hilligardt & Werther model
mean bubble rise speed – superficial gas velocity (m/s)
height in bed (m)
0.11 m/s
0.12 m/s
0.13 m/s
0.14 m/s
0.15 m/s
-0.2
0
0.2
0.4
0.6
0.8
1
1.2
1.4
0.1
0.15
0.2
0.25
0.3
0.35
0.4
0.45
0.5
0.55
0.6

B.3 Distribution plate, at fixed flow

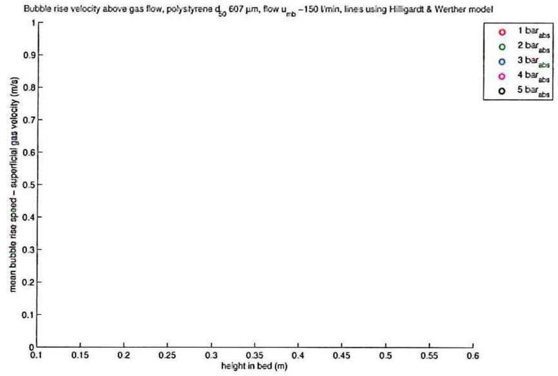

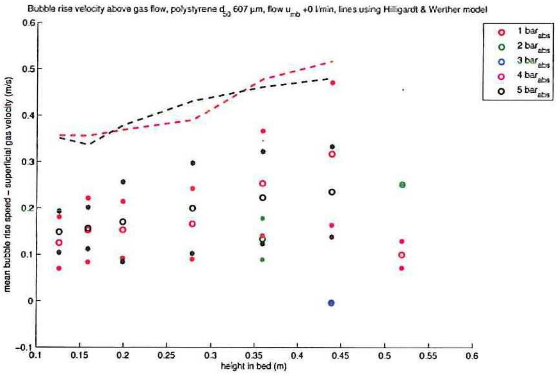

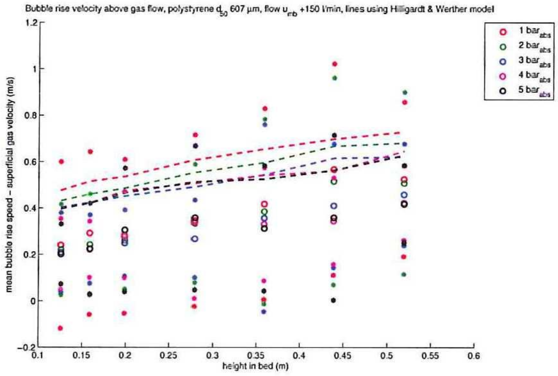

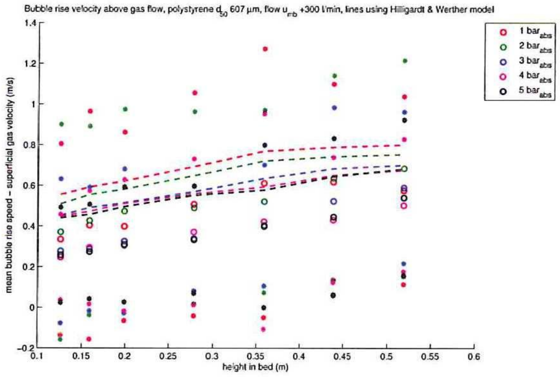

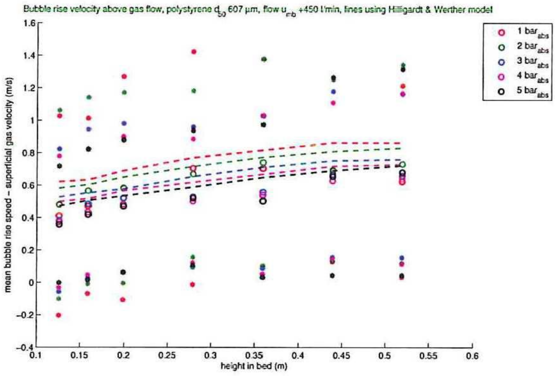

B.4 Single jet, at fixed height

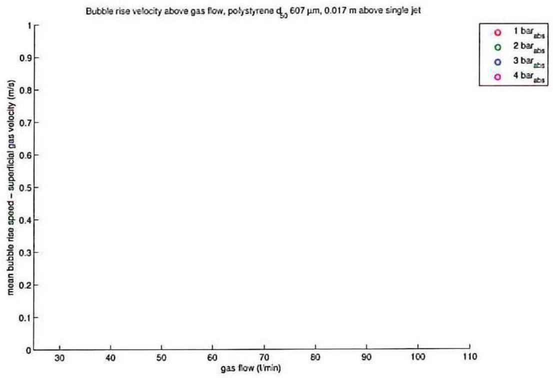

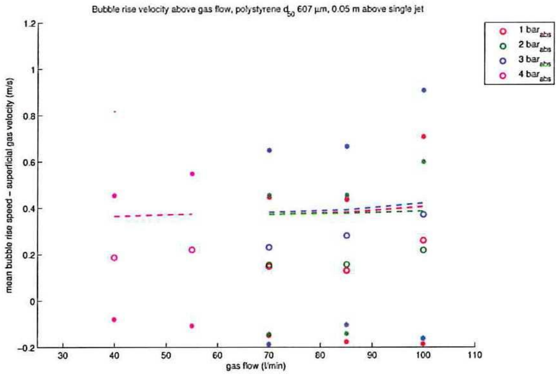

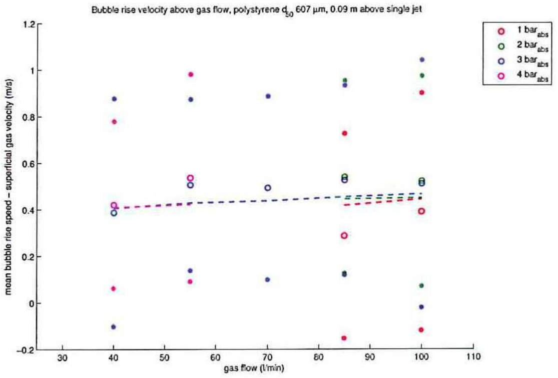

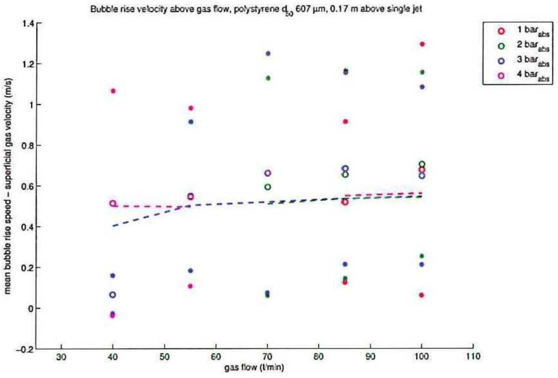

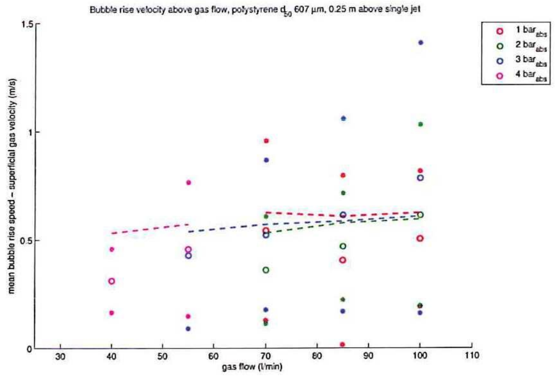

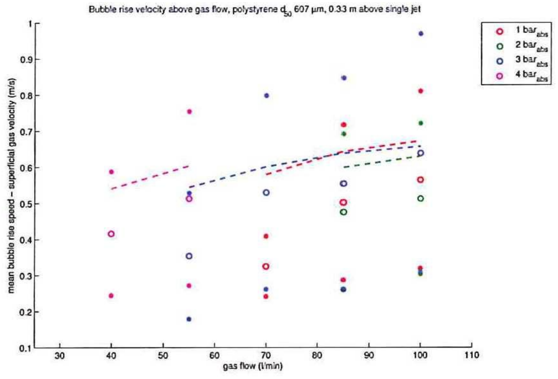

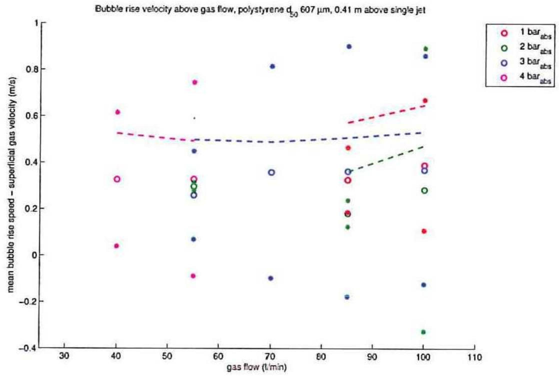
Bubble rise velocity above gas flow, polystyrene d50 607 µm, 0.41 m above single jet
mean bubble rise speed − superficial gas velocity (m/s)
1
0.8
0.6
0.4
0.2
0
−0.2
−0.4
30
40
50
60
70
80
90
100
110
gas flow (l/min)
1 bar abs
2 bar abs
3 bar abs
4 bar abs

B.5 Single jet, at fixed pressure

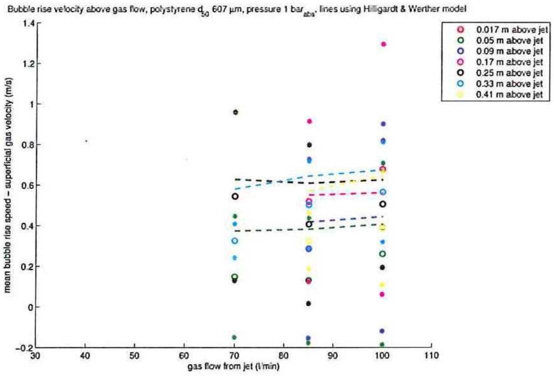
Bubble rise velocity above gas flow, polystyrene d_{50} 607 µm, pressure 1 bar_{abs}, lines using Hilligardt & Werther model

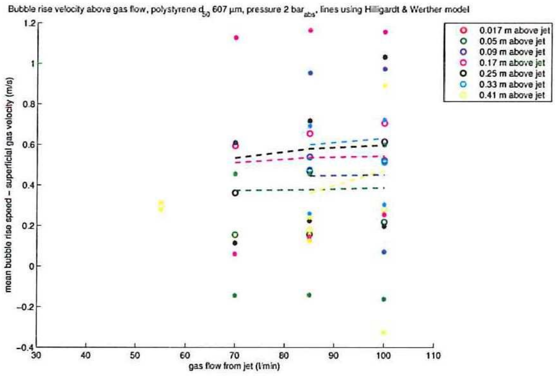
Bubble rise velocity above gas flow, polystyrene d_{50} 607 µm, pressure 2 bar_{abs}, lines using Hilligardt & Werther model

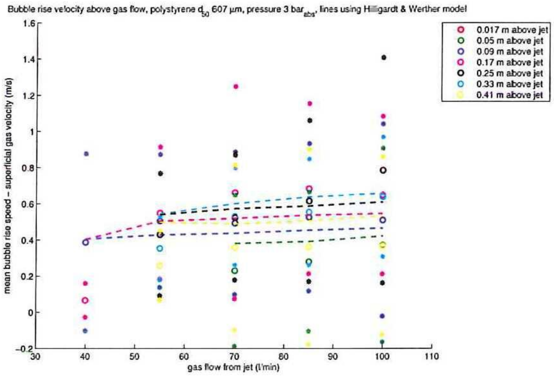
Bubble rise velocity above gas flow, polystyrene d_{50} 607 µm, pressure 3 bar_{abs}, lines using Hilligardt & Werther model

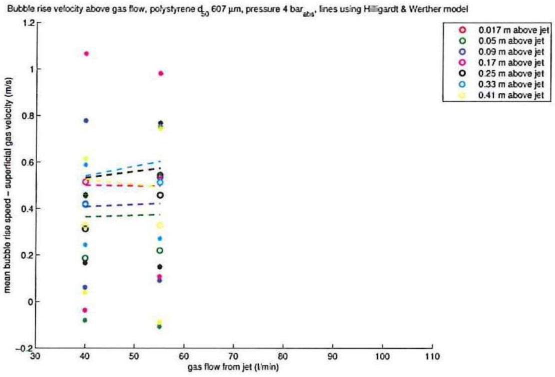
Bubble rise velocity above gas flow, polystyrene d_{50} 607 µm, pressure 4 bar_{abs}, lines using Hilligardt & Werther model

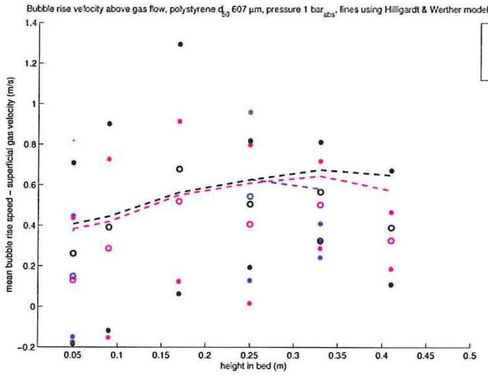
Bubble rise velocity above gas flow, polystyrene d50 607 µm, pressure 1 barabs, lines using Hilligardt & Werther model
mean bubble rise speed – superficial gas velocity (m/s)
height in bed (m)
-0.2
0
0.2
0.4
0.6
0.8
1
1.2
1.4
0.05
0.1
0.15
0.2
0.25
0.3
0.35
0.4
0.45
0.5
40 l/min
55 l/min
70 l/min
85 l/min
100 l/min

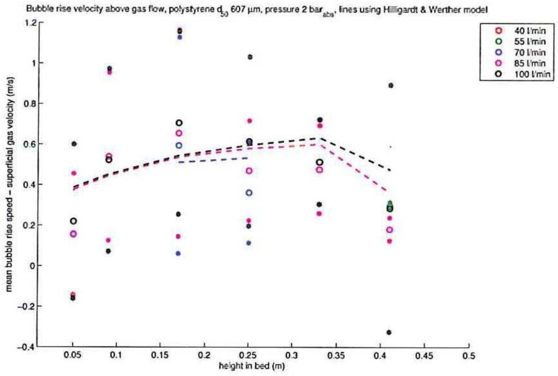
Bubble rise velocity above gas flow, polystyrene d50 607 µm, pressure 2 barabs, lines using Hilligardt & Werther model
mean bubble rise speed – superficial gas velocity (m/s)
height in bed (m)
-0.4
-0.2
0
0.2
0.4
0.6
0.8
1
1.2
0.05
0.1
0.15
0.2
0.25
0.3
0.35
0.4
0.45
0.5
40 l/min
55 l/min
70 l/min
85 l/min
100 l/min

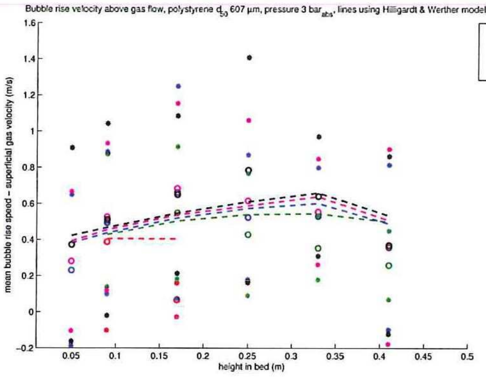
Bubble rise velocity above gas flow, polystyrene d50 607 µm, pressure 3 barabs, lines using Hilligardt & Werther model
mean bubble rise speed – superficial gas velocity (m/s)
height in bed (m)
-0.2
0
0.2
0.4
0.6
0.8
1
1.2
1.4
1.6
0.05
0.1
0.15
0.2
0.25
0.3
0.35
0.4
0.45
0.5
40 l/min
55 l/min
70 l/min
85 l/min
100 l/min

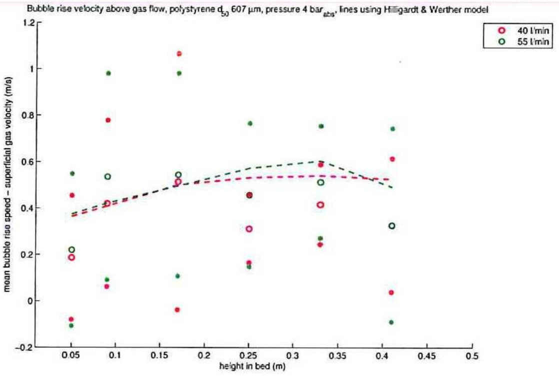
Bubble rise velocity above gas flow, polystyrene d50 607 µm, pressure 4 barabs, lines using Hilligardt & Werther model
mean bubble rise speed – superficial gas velocity (m/s)
height in bed (m)
-0.2
0
0.2
0.4
0.6
0.8
1
1.2
0.05
0.1
0.15
0.2
0.25
0.3
0.35
0.4
0.45
0.5
40 l/min
55 l/min

B.6 Single jet, at fixed flow

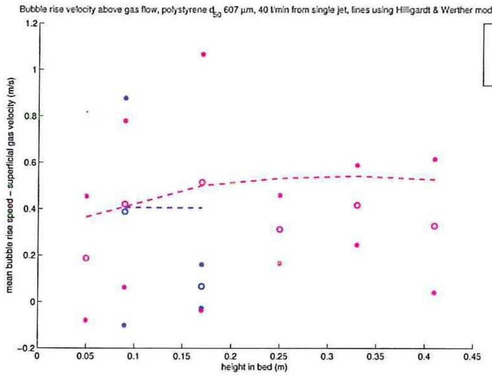

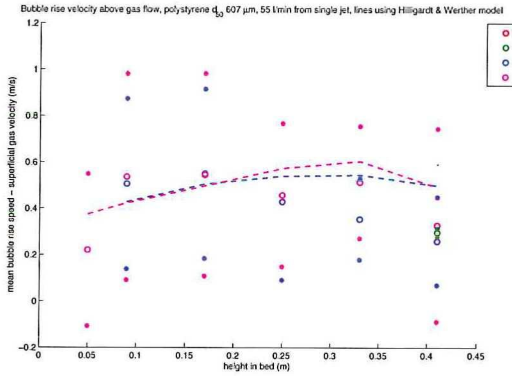

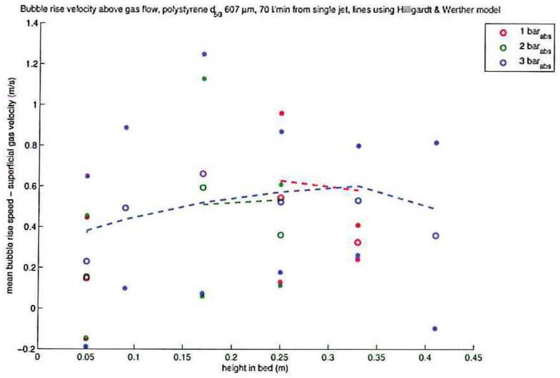

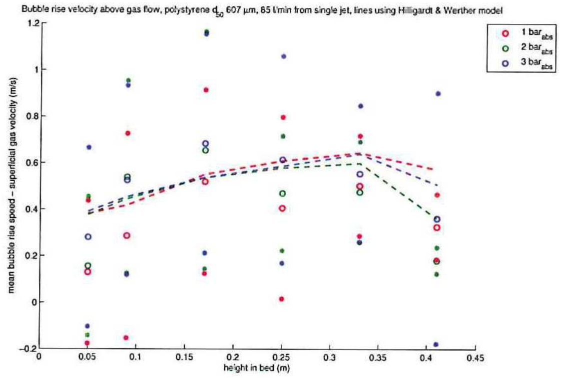

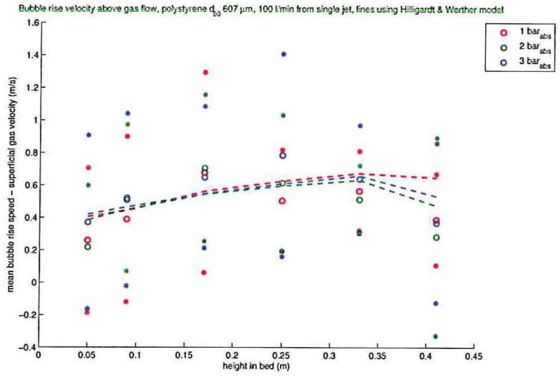

APPENDIX C

Spherical equivalent diameter plots for fines

Detected bubble size and size normalized at 0% fines

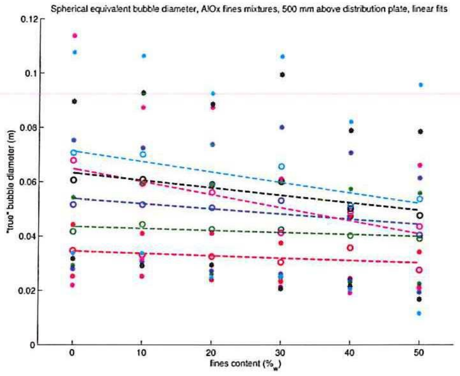
Spherical equivalent bubble diameter, AlOx fines mixtures, 500 mm above distribution plate, linear fits

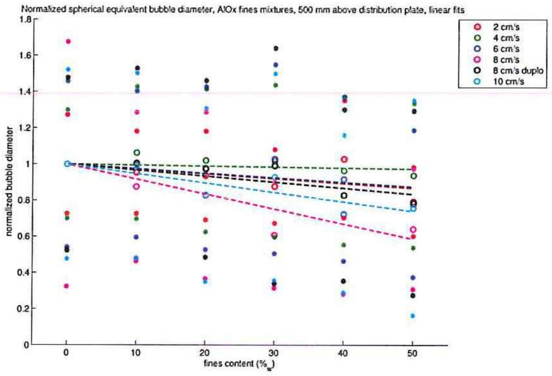
Normalized spherical equivalent bubble diameter, AlOx fines mixtures, 500 mm above distribution plate, linear fits

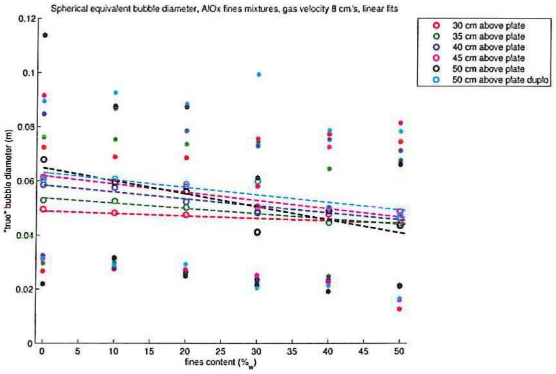
Spherical equivalent bubble diameter, AlOx fines mixtures, gas velocity 8 cm/s, linear fits

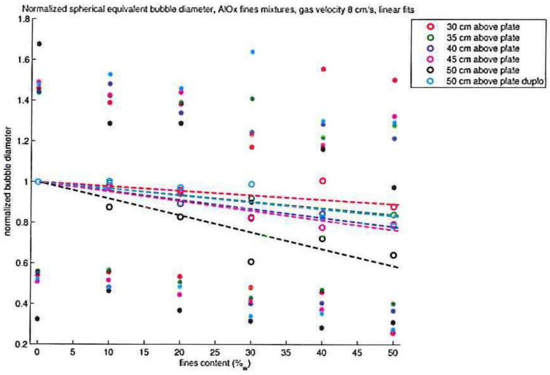
Normalized spherical equivalent bubble diameter, AlOx fines mixtures, gas velocity 8 cm/s, linear fits

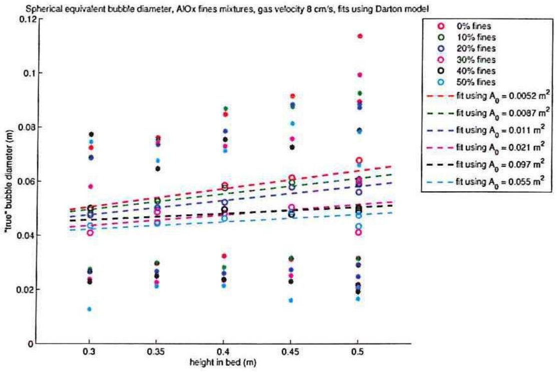
Spherical equivalent bubble diameter, AlOx fines mixtures, gas velocity 8 cm/s, fits using Darton model

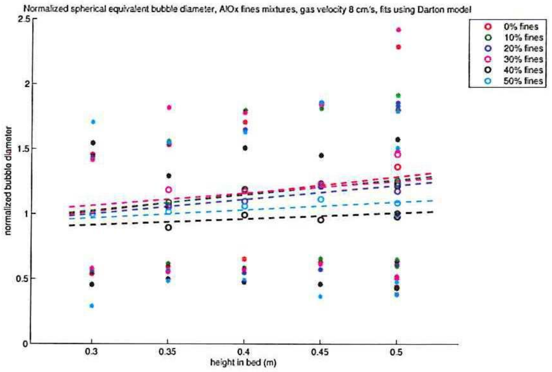
Normalized spherical equivalent bubble diameter, AlOx fines mixtures, gas velocity 8 cm/s, fits using Darton model

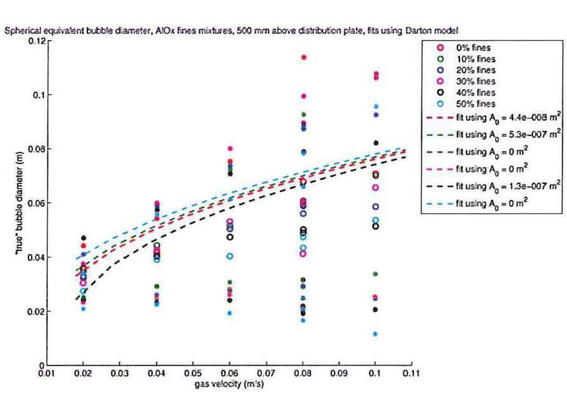
Spherical equivalent bubble diameter, AlOx fines mixtures, 500 mm above distribution plate, fits using Darton model
"true" bubble diameter (m)
0
0.02
0.04
0.06
0.08
0.1
0.12
gas velocity (m/s)
0.01
0.02
0.03
0.04
0.05
0.06
0.07
0.08
0.09
0.1
0.11
0% fines
10% fines
20% fines
30% fines
40% fines
50% fines
fit using A_0 = 4.4e−008 m^2
fit using A_0 = 5.3e−007 m^2
fit using A_0 = 0 m^2
fit using A_0 = 0 m^2
fit using A_0 = 1.3e−007 m^2
fit using A_0 = 0 m^2

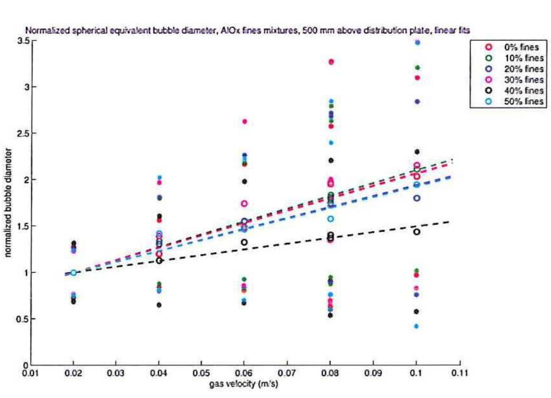
Normalized spherical equivalent bubble diameter, AlOx fines mixtures, 500 mm above distribution plate, linear fits
normalized bubble diameter
0
0.5
1
1.5
2
2.5
3
3.5
gas velocity (m/s)
0.01
0.02
0.03
0.04
0.05
0.06
0.07
0.08
0.09
0.1
0.11
0% fines
10% fines
20% fines
30% fines
40% fines
50% fines

APPENDIX D

Rise velocity plots for fines

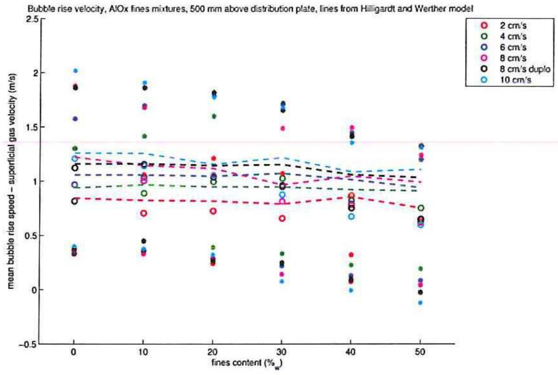

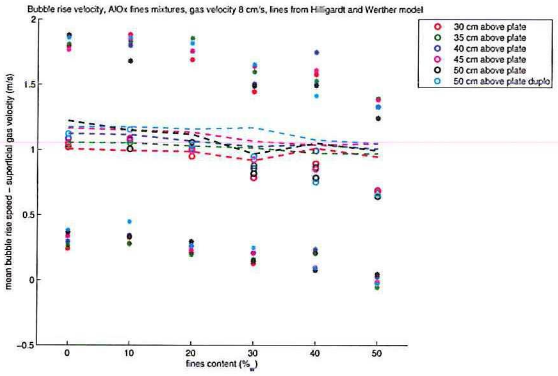

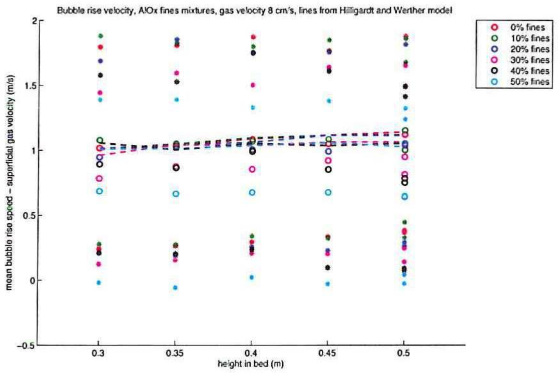

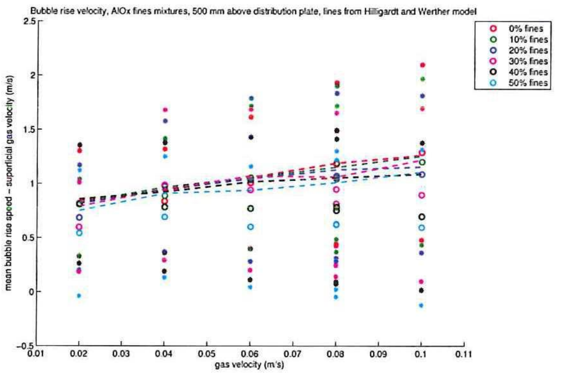

APPENDIX E

Particle size distribution measurements

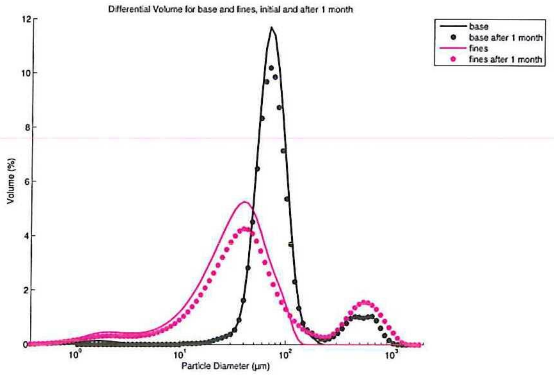

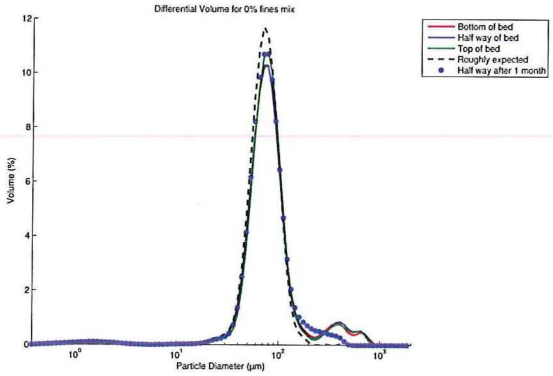

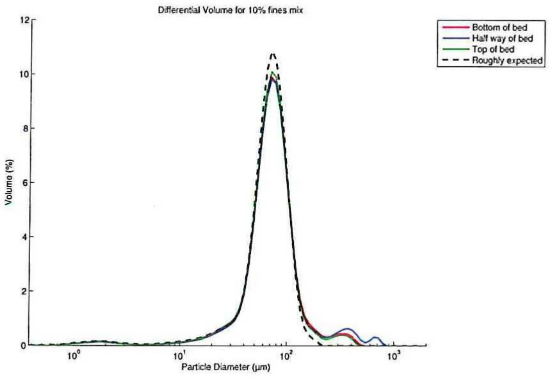

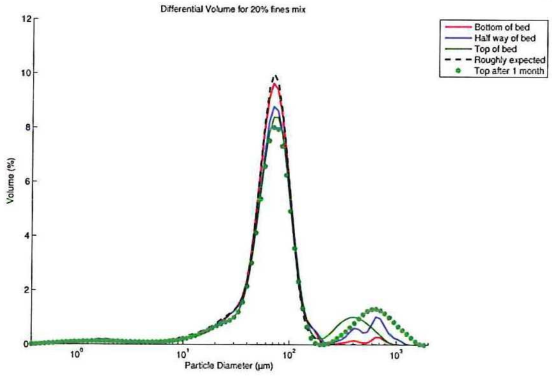

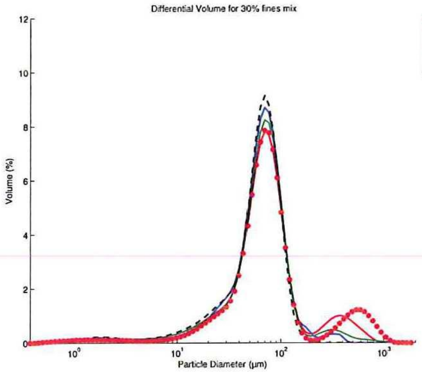
Differential Volume for 30% fines mix
Bottom of bed
Half way of bed
Top of bed
Roughly expected
Bottom after 1 month
Volume (%)
12
10
8
6
4
2
0
10^0
10^1
10^2
10^3
Particle Diameter (μm)

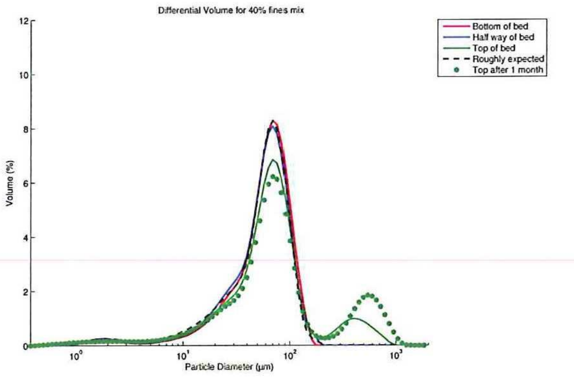
Differential Volume for 40% fines mix
Bottom of bed
Half way of bed
Top of bed
Roughly expected
Top after 1 month
Volume (%)
12
10
8
6
4
2
0
10^0
10^1
10^2
10^3
Particle Diameter (μm)

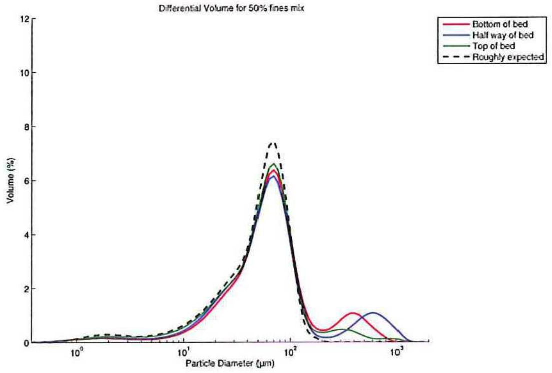
Differential Volume for 50% fines mix
Bottom of bed
Half way of bed
Top of bed
Roughly expected
Volume (%)
12
10
8
6
4
2
0
10^0
10^1
10^2
10^3
Particle Diameter (μm)

EFFECTS OF PRESSURE ON BUBBLE DIAMETER IN A FLUIDIZED BED STUDIED USING FAST X-RAY TOMOGRAPHY

G.C. Brouwer[1], E.C. Wagner[1], J.R. van Ommen[2] and R.F. Mudde[1]
[1] Kramers Laboratorium voor Fysische Technologie
[2] Department of Chemical Engineering
Delft University of Technology, The Netherlands

Summary

Using a fast X-ray tomography setup it is possible to reconstruct 250 images per second of a 25 cm diameter pressurized fluidized bed. The bed consists of polystyrene particles ($d_{50} = 600$ μm, $\rho = 1102$ kg/m^3, Geldart B) which are fluidized using a distribution plate at the bottom of the vessel. We have investigated the spherical equivalent diameter of the bubbles in the bed for different bed pressures. We varied the pressure from 1 to 5 bar$_{abs}$ for different gas flow rates. Our results clearly show that higher pressures lead to smaller bubbles.

Keywords

fluidization, pressure, X-ray, tomography, bubble-size

1 Introduction

Fluidization is used in many chemical engineering applications. Fluidized beds provide a large contact surface area in a relatively small volume. If the gas flow is increased, the bed will generally begin to bubble. Although this ensures the bed is well mixed, the gas in the center of a bubble has limited contact with the particles. Since fluidized beds are often used in gas conversion processes, these bubbles will reduce the performance of the bed. One option to reduce the bubble size, is to raise the pressure inside the bed.

The objective of this paper is to determine the effect of pressure on the size and dynamics of bubbles in a fluidized bed as a function of the gas velocity.

2 Measurement method

Using X-ray tomography it is possible to study bubbles inside a bed. To do this, a setup has been developed at TU Delft [1]. In the middle of the setup a steel column (25 cm diameter) filled with, in this case, polystyrene particles ($d_{50} = 600$ μm, $\rho = 1102$ kg/m^3, Geldart B) is placed. This column is placed on a height adjustable table, so the bed can be studied at different heights. The setup measures in two planes. The cross-sections of both planes are reconstructed using the Algebraic Reconstruction technique. In this way bubbles can be detected in the lower and upper plane. These bubbles can be matched, and in that way the speeds and true sizes of the bubbles can be determined. It is possible to reconstruct 250 images per second and detect bubbles with a diameter as small as 2 cm.

For the measurement series the bed is fluidized using compressed air fed through a flow controller and then through the distribution plate at the bottom of the column. Using a valve at the top of the bed it is possible to control the pressure inside the vessel. Measurements were done at various heights (126 - 519 mm above plate), various gas flow settings (10 - 32 cm/s) and various pressures (1 - 5 bar$_{abs}$). Each measurement consists of 60 seconds of data. This data is reconstructed and a bubble detection script is run. A 60 second measurement typically contains about 150 bubbles. Such a number of bubbles will give a good indication of the distribution in size, speed and location of the bubbles. The accuracy can be improved by further extending the measurement time.

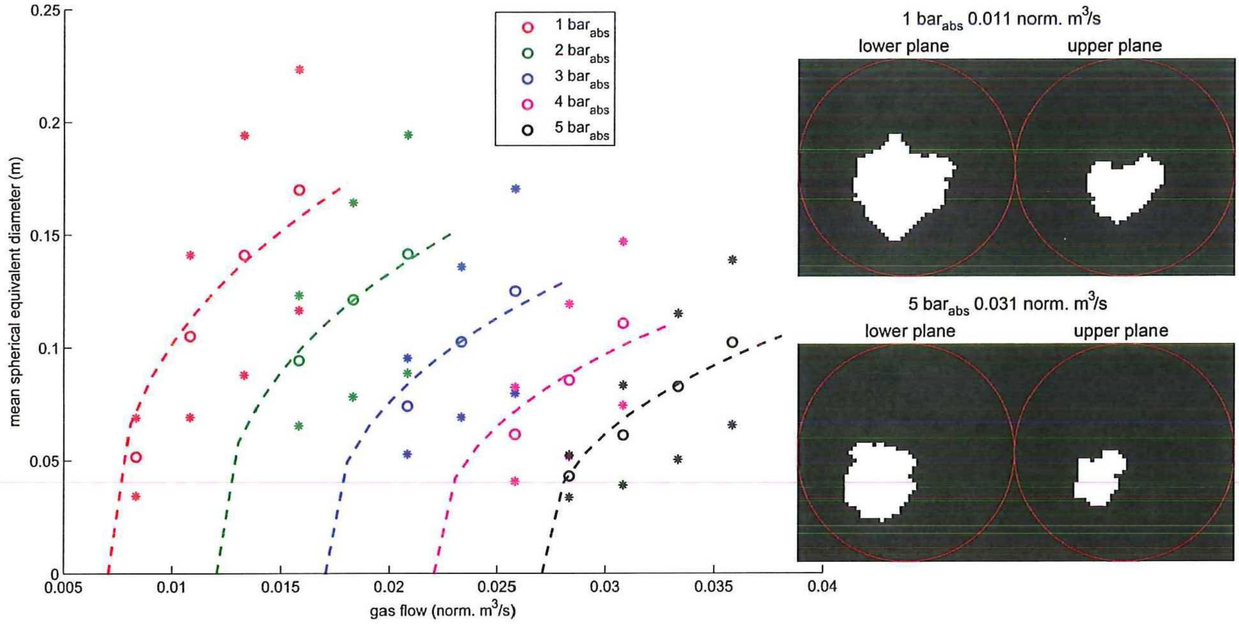

Figure 1: Mean spherical equivalent bubble diameter, polystyrene particles d_{50} 600 μm, 0.439 m above distribution plate. The mean bubble size (circles) and standard deviation around this value (asterisks) are shown, curves fitted using Darton's relation (dash curves). On the right two sets of thresholded tomograms are shown. In both cases a bubble is clearly visible in the lower plane, while it is just starting to appear in the upper plane.

3 Results

The bubble size has been determined at various heights in the bed. Figure 1 shows the mean spherical equivalent diameter of the bubbles based on their detected true volume for one of the studied measurement heights. For higher pressures fluidization starts at a lower superficial gas velocity. It can clearly be seen that a higher pressure will drastically reduce the bubble size at the same volumetric gas flow. The lines through the values are fits based on the bubble growth model by Darton [2]:

$$d_e = 0.54(u - u_{mf})^{0.4}(h + 4\sqrt{A_0})^{0.8} g^{-0.2} \quad (1)$$

The catchment area A_0 is used as a fitting parameter.

This clearly shows that the fast X-ray setup can be used to examine the effects of increased pressure on the bubble size in a fluidized bed. Moreover, it enables the investigation of the velocity and shape of the bubbles. A strong point of the current measurement system is that all information obtained is dynamic, i.e. even bubble interaction can be revealed.

References

[1] R. F. Mudde, Bubbles in a fluidized bed: A fast X-ray scanner, AIChE Journal 57-10 (2011) 2684–2690.

[2] R.C. Darton, R.D. LaNauze, J.F. Davidson D. Harrison, Bubble growth due to coalescence in fluidised beds, Chemical Engineering Research and Design 55a (1977) 274–280.

Acknowledgements

The time I've spent at the Kramers Lab and later at the Leeghwaterstraat has been a great time for me. I've been able to do very interesting work with the support of many great people.

First of all I would like to thank my supervisors Rob Mudde and Ruud van Ommen. Our progress meetings were always productive, interesting and fun actually. Talking about how challenges can be overcome and how to interpret results, always gave me a boost to continue my work. I was given enough freedom to make this project my own, but if I needed guidance I could always count on you.

Because of the experimental nature of my research I have been working closely with the technicians and research assistants. I especially would like to thank Evert Wagner, because he was my most important problem solver concerning the X-ray setup. But without the help of the other people at the Kramers Lab I would not have been able to finish my project.

The student room has always been a great place to work. The coffee breaks together with the PhD students were always fun and a good distraction from our work. The movie and 'how is the man'-nights were also a lot of fun. I've enjoyed being in your company.

I would also like to thank my girlfriend, Floor, for putting up with me during this project. Sometimes I would be working all night even though she came to visit. She also helped me with my report and presentation.

And last, but not least, I would like to thank my parents. During the many years of (not) studying in Delft, they have always been supportive and were always able to help me with difficult choices.

Gerrit Brouwer
Delft, December 2011